STARS

University of Central Florida
STARS

Electronic Theses and Dissertations, 2004-2019

2014

Experiments in Graphene and Plasmonics

Christian Smith
University of Central Florida

Part of the Physics Commons
Find similar works at: https://stars.library.ucf.edu/etd
University of Central Florida Libraries http://library.ucf.edu

This Doctoral Dissertation (Open Access) is brought to you for free and open access by STARS. It has been accepted for inclusion in Electronic Theses and Dissertations, 2004-2019 by an authorized administrator of STARS. For more information, please contact STARS@ucf.edu.

STARS Citation

Smith, Christian, "Experiments in Graphene and Plasmonics" (2014). *Electronic Theses and Dissertations, 2004-2019*. 1249.
https://stars.library.ucf.edu/etd/1249

University of Central Florida
STARS
Showcase of Text, Archives, Research & Scholarship

EXPERIMENTS IN GRAPHENE AND PLASMONICS

by

CHRISTIAN W. SMITH
B.S. University of Central Florida, 2010

A dissertation submitted in partial fulfillment of the requirements
for the degree of Doctor of Philosophy
in the Department of Physics
in the College of Sciences
at the University of Central Florida
Orlando, Florida

Fall Term
2014

Major Professor: Masahiro Ishigami

© 2014 Christian W. Smith

ABSTRACT

Graphene nanoribbons, graphene based optical sensors, and grating based plasmonics are explored experimentally. Graphene nanoribbons exhibit highly insulating states that may allow for graphene based digital applications. We investigate the sensitivity of these states to local charged impurities in ultra high vacuum. We look into the possibility of isolating two-dimensional films of H-BN and BSCCO, and test for any interesting phenomena. We also assess graphene's applicability for optical sensing by implementing a new style of spectral detector. Utilizing surface plasmon excitations nearby a graphene field-effect transistor we are able to produce a detector with wavelength sensitivity and selectivity in the visible range. Finally, we study another plasmonic phenomenon, and observe the resonant enhancement of diffraction into a symmetry-prohibited order in silver gratings.

This thesis is dedicated to my loving parents, wife, and kitty.

ACKNOWLEDGMENTS

First and foremost I would like to thank my parents for their unwavering support during my endeavors in higher education. I would like to thank my research advisor Dr. Masahiro Ishigami. Under his tutelage I have become a confident independent experimentalist. I would also like to thank Dr. Peale, Dr. Mucciolo, Dr. Cleary, Dr. Avrutsky, and Dr. Mou for teaching me some of the world's many mysteries. I would like to thank my fellow researchers Jyoti, Ryuichi, Mike, Ben, Brandon, Farnood, and many others along the way. I would also like to thank the funding and opportunities offered by the National Science Foundation and the Air Force Office of Scientific Research. Finally I would like to thank my wife Kelsey for everything.

TABLE OF CONTENTS

LIST OF FIGURES x

LIST OF ACRONYMS xxi

CHAPTER 1 : GRAPHENE 1

1.1 Background 1

1.2 Graphene Device Fabrication 4

1.2.1 Exfoliation Methods 4

1.2.2 CVD Growth 9

1.2.3 Transfer 11

1.2.4 Raman Characterization 17

1.2.5 Device Fabrication 19

1.2.6 Wirebonding 24

1.2.7 Electronic Transport 26

1.2.8 Graphene Device Post-Processing 28

1.3 Electrode Transfer 34

1.3.1 Background 34

1.3.2 Methodology 35

1.3.3 Results 36

CHAPTER 2 : GRAPHENE NANORIBBONS 39

2.1 Background 39

2.2 Methodology 40

2.3 Results 44

2.4 Discussion 48

2.4.1 Increasing Insulating Behavior 52

CHAPTER 3 : OTHER 2D MATERIALS 55

3.1 Hexogonal Boron Nitride 55

3.1.1 Background 55

3.1.2 Methodology 56

3.1.3 Results 59

3.2 BSCCO 60

3.2.1 Background 60

3.2.2 Methodology 61

3.2.3 Results 63

CHAPTER 4：PLASMON COUPLED DEVICES 66
4.1 Background 66
4.1.1 Kretschmann configuration 70
4.2 Methodology 72
4.3 Experimental Setup 76
4.4 Results 81
4.5 Discussion 87
4.5.1 Second Generation Coupled Devices 90
4.6 Grating Devices 92
4.6.1 Methodology 94
4.6.2 Results 95

CHAPTER 5：SPP FACILITATED DIFFRACTION INTO PROHIBITED ORDERS 97
5.1 Backround 97
5.2 Methodology 99
5.3 Results 101
5.4 Discussion 104

CHAPTER 6：CONCLUSIONS 106

APPENDIX A：Scanning Electron Microscope Standard Operating Procedure 107

A.1 Setup 108

A.2 Imaging 109

APPENDIX B：Wirebonder Standard Operating Procedure 113

B.1 Setup 114

B.2 Bonding 116

APPENDIX C：Goniometer Standard Operating Procedure 118

C.1 General Goniometer Control 119

C.2 Measurement 119

LIST OF REFERENCES 121

LIST OF FIGURES

LIST OF ACRONYMS

2DEG	Two-Dimensional Electron Gas
AC	Alternating Current
AFM	Atomic Force Microscopy
Ag	Silver
Al	Aluminum
APS	Ammonium Persulfate
Ar	Argon
ATR	Attenuated Total Reflectance
Au	Gold
BOE	Buffered Oxide Etch
BSCCO	$Bi_2Sr_2CaCu_2O_{8+\delta}$
CAD	Computer Aided Drafting
CPU	Central Processing Unit
CVD	Chemical Vapor Deposition
DAC	Digital to Analog Converter
DC	Direct Current
DUV	Deep Ultra-Violet

ESD	Electrostatic Discharge
FET	Field Effect Transistor
FWHM	Full-Wide Half-Maximum
H_2	Hydrogen
hBN	Hexagonal Boron-Nitride
HMDS	Hexamethyldisilazane
IR	Infrared
IPA	Isopropyl Alcohol
MCP	Minimum Conductivity Point
MCT	Mercury Cadmium Telluride
MIBK	Methyl Isobutyl Ketone
MMA	Methyl Methacrylate
NPGS	Nanometer Pattern Generation System
O_2	Oxygen
PAC	Photoactive Compound
PDMS	Polydimethylsiloxane
PET	Polyethylene Terephthalate
PMMA	Poly(Methyl Methacrylate)
QCL	Quantum Cascade Laser
SEM	Scanning Electron Microscope
SiO_2	Silicon Dioxide

SOP	Standard Operating Procedure
SPP	Surface Plasmon Polariton
SPR	Surface Plasmon Resonance
STM	Scanning Tunneling Microscope
RF	Radio Frequency
RPM	Revolutions per Minute
T_C	Critical Temperature
TIR	Total Internal Reflectance
TE	Transverse Electric
TM	Transverse Magnetic
UHV	Ultra-High Vacuum
UV	Ultra Violet

CHAPTER 1
GRAPHENE

1.1 Background

Graphene is a two-dimensional array of carbon atoms arranged in a honeycomb lattice. The trigonally bonded carbon atoms form an atomically thin sheet of strong in-plane σ-bonds, with the exceptional electronic properties of graphene originating from the out-of-plane π-orbitals located near the chemical potential. Figure 1.1(a) shows the unit cell in graphene, which consists of two carbon atoms. Unit lattice vectors $\vec{a_{1,2}}$ comprise the two triangular interleaving sublattices A and B.

The π-bands are well described by a nearest-neighbor tight binding model, and this was first applied to a single sheet of graphite in 1947 [6]. Choosing a basis in the sub-lattice positions of A and B the Hamiltonian in momentum space can be expressed as

$$\mathscr{H}_{\vec{k}} = \begin{pmatrix} \varepsilon_A & \xi \\ \xi^* & \varepsilon_B \end{pmatrix} \tag{1.1}$$

where $\varepsilon_{A(B)} = 0$ corresponds to the on-site energy of the carbon atom at site $A(B)$. Because each site lacks inversion symmetry ξ is complex, and has the form

$$\xi = t(e^{i\vec{k}\cdot\vec{a}_1} + e^{i\vec{k}\cdot\vec{a}_2} + e^{i\vec{k}\cdot\vec{a}_3}) \ , \tag{1.2}$$

where the next nearest hopping element $t \approx 2.6$eV, and the vectors $\vec{a}_1 = a(1,0)$ $\vec{a}_2 = \frac{a}{2}(-1,\sqrt{3})$ $\vec{a}_3 = \frac{a}{2}(-1,-\sqrt{3})$, which denote the three nearest-neighbor positions with a = 1.42Å [7]. The eigenvalues for this tight-binding Hamiltonian are shown in the energy momentum diagram of Figure 1.1(b).

Of particular interest is the behavior at the Dirac points K (K'), for small wave-vectors $k \ll K$. We can express the dispersion relation as

$$E_{\pm} \approx \pm\hbar v_F k, \tag{1.3}$$

where $v_F \approx 1 \times 10^6$m/s is the Fermi velocity in graphene. This linear dispersion near the Dirac point in graphene gives rise to the Dirac cones, and the zero gap semiconducting nature of the material. Expanding Eq. 1.1 close to the K point, the Hamiltonian becomes

$$\mathscr{H}_K = \hbar v_F \begin{pmatrix} 0 & k_x - ik_y \\ k_x + ik_y & 0 \end{pmatrix} \ , \tag{1.4}$$

which is the Dirac Hamiltonian for massless relativistic fermions renormalized to the Fermi velocity. Thus, within these cones, the charge carriers in graphene behave as massless relativistic particles with Fermi velocity $\approx$ 1/300 the speed of light. The linear dispersion is only valid within about 1eV above or below the Dirac points [8], where at higher energies the dispersion is no longer linear due to lattice effects such as trigonal warping [9].

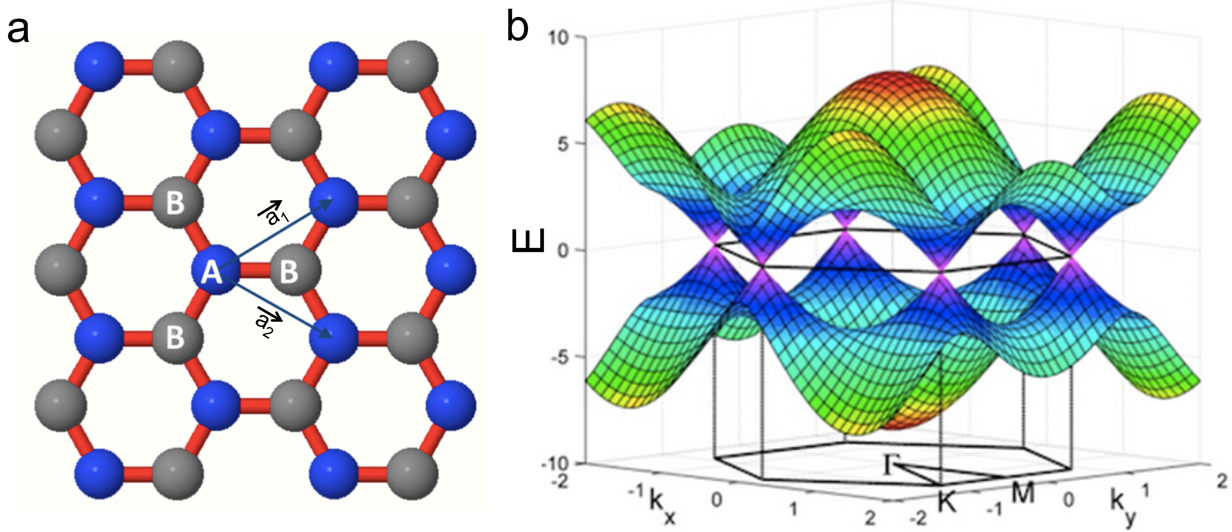

Figure 1.1: **Graphene Lattice and Band Structure of First Brillouin Zone.** (a) Crystal structure of graphene with vectors $\vec{a_{1,2}}$ defining the unit cell and sublattices A and B. [1] (b) The energy–momentum dispersion relation of graphene for the first Brillouin zone. Dirac cones meeting at the K and K' (Dirac) points exhibit linear dispersion near the chemical potential.

Shortly after the experimental isolation of graphene [10], research into the material [11] was spurred due to the discovery of several exciting electronic properties. The charge carriers in graphene were confirmed to be massless Dirac fermions [3]. Owing to its band structure, graphene was found to have extremely high room-temperature mobility. Ambient carrier concentrations as high as $1\times10^{13}\text{cm}^{-2}$ and mobility exceeding $15\times10^{3}\text{cm}^2/\text{Vs}$ were reported [11][3], with mobility as high as $1\times10^{5}\text{cm}^2/\text{Vs}$ for graphene suspended above the substrate [12]. Graphene was also found to have unique transport effects such as residual minimum conductivity and an ambipolar field-effect [13][14]. Although graphene possesses an unusually high room-temperature carrier mobility, the lack of an electronic band gap limits its applications in logic roles, where high on-

off ratios and high mobility are required. We have joined in the attempts of others to engineer a bandgap in graphene. This will be explored in the study of graphene nanoconstrictions in the next chapter.

In addition to digital applications, graphene is an exciting system for optical studies, due to its ideal two-dimensional electron gas (2DEG) supported by the π-orbitals, and robust ballistic transport regime with carrier mean free path over 1μm [15]. We will also explore optical applications for graphene-based devices in later chapters.

1.2 Graphene Device Fabrication

1.2.1 Exfoliation Methods

Single-layer graphene films can be exfoliated from bulk graphite flake in a number of ways. The most common method, originally used to produce the first isolated graphene flakes [10], is the so-called "Scotch-tape" method. In this method a portion of the bulk graphite flake is removed using the adhesive side of the sticky tape. Then the portion of the graphite flake attached to the tape is thinned further by subsequent pealing with fresh adhesive. As the flake is exfoliated the tape becomes more and more translucent, and the color changes from dark to light grey. Once the graphite flake has been deemed sufficiently thinned, the tape adhesive is put in contact with the desired substrate. The backside of the tape is then rubbed with plastic forceps or cloth to produce an electrostatic repulsion that forces the graphite flakes against the substrate. The tape is then

removed from the substrate, leaving behind the graphite flakes that were secured to the surface with van der Waals forces. This brute-force approach results in graphene flakes that have lateral size on the order of tens of microns, scattered within thicker graphite flakes. These samples must then be optically documented, taking inventory of any thin graphite flakes. The substrate of choice for optimal optical contrast is silicon wafer with 300nm of thermal oxide [16]. This thickness of oxide is crucial to making graphene visible. Prior to all processes the Si/SiO_2 wafers were cleaned in piranha solution (H_2SO_4:H_2O_2 1:3). Although the sample preparation portion of this method is a quick and easy process, cataloging all of the thin flakes can be tedious due to their scarcity relative to thicker flakes on the surface. These thick graphite flakes present a challenge for designing FETs because they can unintentionally short electrodes or lead to electrode discontinuity across the flake steps. Figure 1.2 shows a low- and high-magnification optical image of exfoliated graphite flake deposited on top of a Si/SiO_2 wafer. Alignment markers are visible as a gold array of regular shapes and the number 34. In Figure 1.2 (b) a graphene candidate is circled in red. This was the method we initially used to isolate graphene flakes from bulk kish graphite. Comparison of different tape adhesives and degree of thinning allowed for the production of samples with less adhesive residue and un-exfoliated flakes. Unfortunately the adhesive residue on the substrate proved difficult to remove, and tended to degrade the electronic performance of these devices.

Before moving to more advanced techniques, we did some testing to optimize the tape method. We wanted to compare the exfoliation efficiency of various types of adhesive tape. We purchased several over-the-counter varieties, and tested the performance of each type of tape. We evaluated the tapes based on the exfoliation observed on the transferred material, as well as the amount of

residual adhesive on the wafers. We then determined that tapes with a greater adhesive strength would leave behind more residue, but would be able to exfoliate the flakes more efficiently. The same level of exfoliation could be achieved on the lower adhesive strength tape, but more peeling steps needed to be performed.

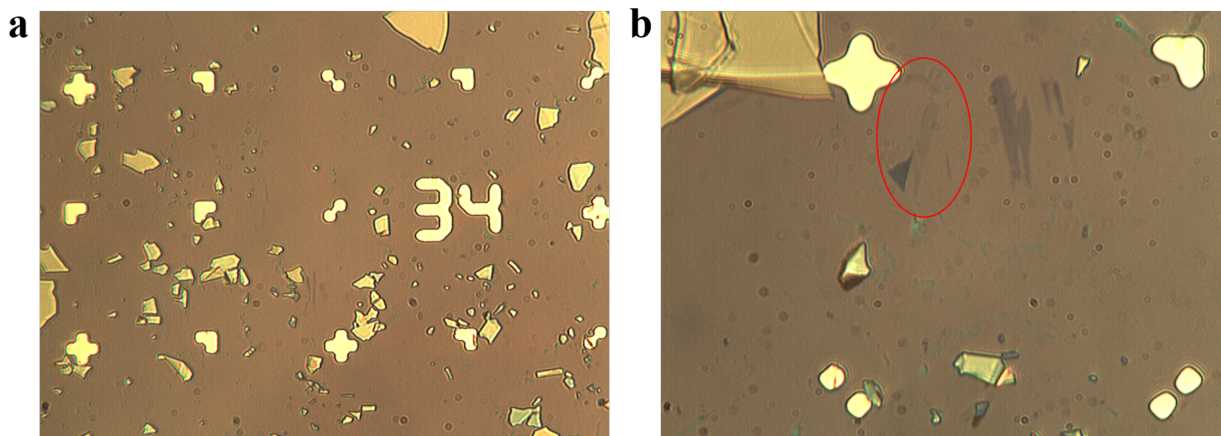

Figure 1.2: **Optical Images of Tape Method Exfoliated Graphite on SiO_2.** (a) Optical micrograph of exfoliated graphite on top of 280nm of SiO_2 on top of silicon wafer prepared using the tape method. Periodic regular shapes in gold are alignment markers for cataloging and device fabrication. (b) Optical image of a graphene flake prepared by tape method. The faint contrast difference due to the graphene film (purple) is surrounded by a red circle for clarity. Neighboring thick graphite flakes (yellow) and adhesive resiude (green) are visible.

The downside of more peeling steps is that the flakes would end up breaking into smaller pieces, and there would be more bulk graphite flakes crowding the candidates. Tapes with low adhesive strength benefited from very little residue deposited on the sample surface. The size of the flakes and the bulk material could be designed around, but the residue would affect the graphene transport

properties. In search of low adhesive tapes to reduce adhesive residues a special kind of tape (Ultron Systems Part No. 1007 R-0.8), originally designed for wafer dicing, was the tape capable of producing the cleanest samples.

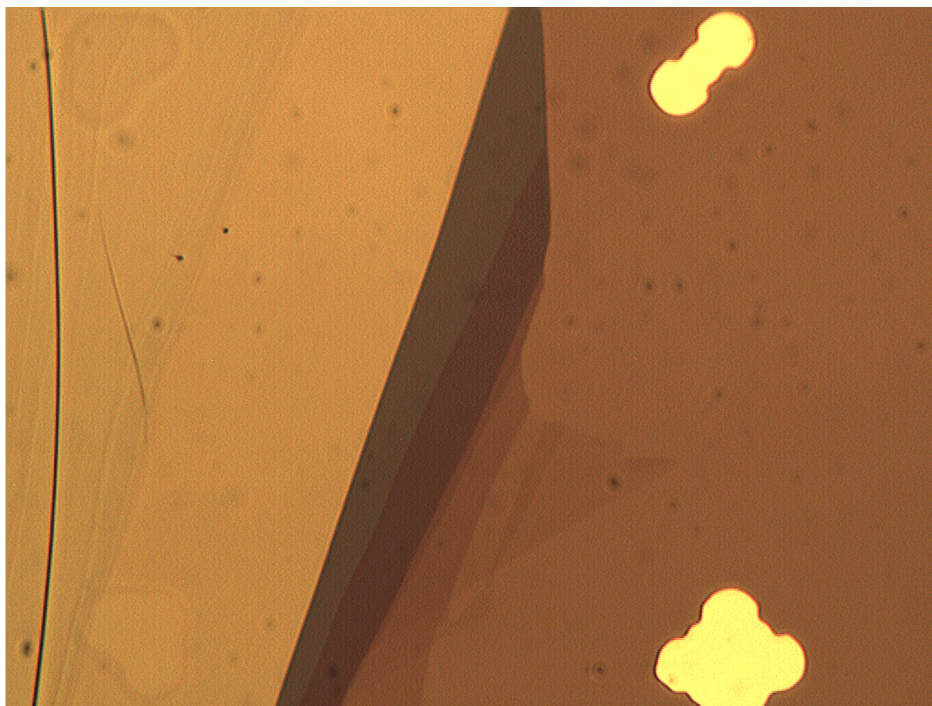

Figure 1.3: **Optical Image of Rubbing Method Exfoliated Graphite on SiO_2.** Optical micrograph of exfoliated graphite on top of 280nm of SiO_2 on top of silicon wafer prepared using the rubbing method. The graphite flake undergoes a thickness gradient from left to right, with the bulk graphite (yellow) thinning (blue) to multi-layer graphene (dark purple), then bilayer graphene (purple), and finally triangular graphene (faint purple).

During our optimization it was noted that there was a seasonality to the exfoliation performance. Our group noticed that in the winter and spring seasons there was a pronounced increase in the exfoliated flakes present on the wafer after exfoliation. In fact the number of bulk flakes was

also increased. In the summer and fall we saw the number of flakes on each wafer decrease. We eventually realized that it was the native Floridian humidity that was responsible for these productivity swings. The moisture in the air would impede the electrostatic repulsion step used to deposit the graphite flakes on the sample. Because of this effect we implemented a dehumidified dry room to increase the productivity year round.

A more sophisticated approach known as the "rubbing" method allowed for an adhesive-residue-free exfoliation of graphene, although the process was more skill intensive than the "tape" method. In this next method the bulk graphite flake is secured to a piece of tape, and a second piece of tape is used to perform an initial exfoliation of the bulk flake. Then, by using very fine tipped tweezers, pieces of graphite are lifted from the bulk flake. If the piece of graphite removed from the bulk is sufficiently flat and thin, van der Waals forces would allow the flake to adhere to the substrate surface. The target surface must be exceedingly clean, and the method of choice for substrate preparation was either a piranha etch or O_2 plasma etch. Once the sample had several flakes secured to the surface, it could be grazed with either a sharp razor edge or a secondary, fresh wafer. This cleaving process can be repeated as many times as necessary, and the results checked under the optical microscope each time in order to produce graphene consistently. With the rubbing method the samples are more difficult and time consuming to produce, but the time spent visually inspecting the samples for graphene candidates is greatly reduced. In addition, the challenges of designing electrodes to weave around bulk graphite flakes were also alleviated. Figure 1.3 shows an optical micrograph of a graphene candidate produced using the rubbing method. The candidate is connected to a bulk graphite crystal, but the neighborhood of this flake is much less crowded.

Once we became skilled in this method, the majority of our samples were produced by rubbing. This contributed to a higher initial cleanliness of the graphene, and better electrical performance of finished devices.

1.2.2 CVD Growth

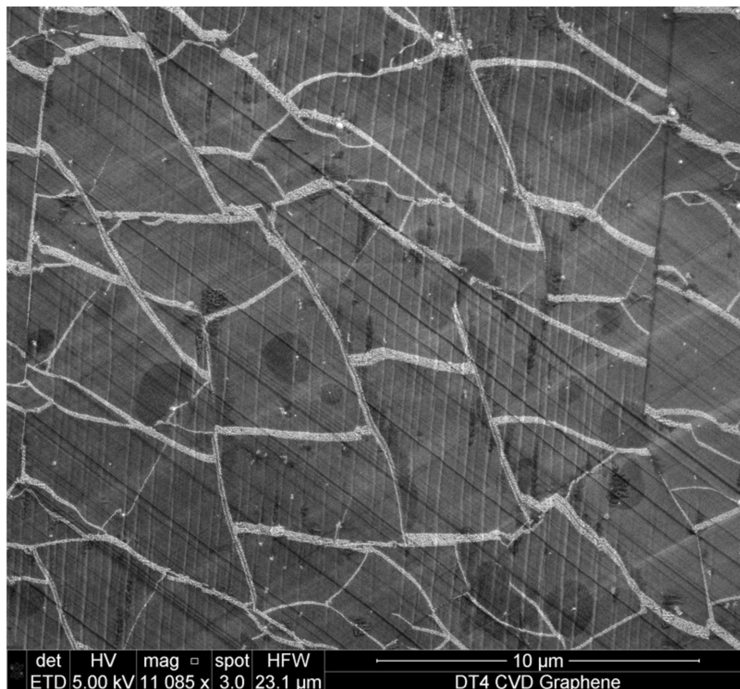

Figure 1.4: **SEM Micrograph of CVD graphene on Cu foil.** SEM image of CVD graphene grown on Cu foil. The Cu terraces that create wrinkles in the graphene film can be seen as the angled periodic dark lines. Vertically oriented white lines are likely stress fractures in the graphene film.

The mechanical exfoliation process leaves much to be desired. It suffers from low throughput, high labor intensity, and small nonuniform graphene films. A process was developed to grow large-area single-layer films by using a catalytic growth substrate. The CVD process we used mimicked the process adopted by others to obtain continuous, large domain, single-layer graphene films [17][18][19]. Using a high throughput roughing pump we kept the pressure below 70mTorr throughout the growth. Alfa Aesar (Part No. 46986) 99.8% purity Cu foil was used as the growth substrate, which was pretreated in acetic acid to remove any unwanted oxidation. Next the foil was rinsed of residues in deionized water, prior to being loaded in the tube for the growth process. The tube was evacuated and then purged with 2sccm hydrogen, before raising the temperature of the furnace to 900°C in order to further clean the surface of the Cu foil. After annealing at this temperature for 2 hours with only the hydrogen flowing, the furnace is taken to 1000°C, just below the melting point of Cu. Methane acts as the precursor for the graphene growth, and 20.48sccm of methane are introduced once the Cu reaches the reaction temperature. During the next 30 minutes, some carbon from the methane is dissolved in the surface of the Cu foil. After the Cu is given enough time at this temperature to absorb a sufficient amount of carbon, the furnace temperature is lowered quickly. The carbon dissociates to the surface and forms a film of hexagonally arranged atoms within each Cu grain boundary. It is thought that the speed at which the Cu is cooled plays an important role in the size of the resulting grain boundaries of the graphene. To this end we added a linear bearing system to our furnace, allowing the heating elements to quickly slide to the opposite side of the tube for fast cooling [20]. Once the Cu has cooled, the gas flows are halted, and the Cu removed from the tube. Figure 1.4 shows an SEM micrograph of Cu foil, after CVD

graphene synthesis. The Cu terraces are situated at a $\sim 45^{\circ}$ angle, and are periodic dark lines. The vertically oriented white lines are likely fractures in the graphene film caused by strain during mishandling.

The graphene formation is thought to begin at seed regions of the Cu surface, likely with compositional impurities, hence the reason for using a Cu film with a slightly lower purity than the highest available. With insufficient growth time, the growth fronts never expand large enough to make a continuous film, while excess growth time allows for a second growth to form on top of the first layer, resulting in patches of bi-layer graphene. As the seed region expands laterally, for a continuous film each region inevitably encounters a neighboring growth front. As these growth fronts come into contact a tilted grain boundary forms between the two, creating one of the primary drawbacks of CVD grown graphene. Transport across the grain boundaries in this polycrystalline film is not perfect, with scattering at these boundaries resulting in a larger sheet resistance, and lowered field-effect mobility in the transport as compared to single-crystal graphene produced by exfoliation. The benefit of the CVD process is the size of the films able to be produced. The graphene film coats both surfaces of the Cu foil, but traditionally the top surface has more care taken to preserve cleanliness, and it is only this upper film that is used.

1.2.3 Transfer

To transfer the CVD graphene from the surface of the Cu foil to an arbitrary target substrate, we experimented with several methods. In essence the various methods all relied on the same

principles. The graphene is first supported by some sort of polymer or film, typically hundreds of nanometers thick. The unwanted graphene is removed from the uncoated side of the foil via plasma etching. Next the Cu substrate and graphene are separated, allowing the supported graphene to either float on the surface of a solution, or in some cases become affixed to a thicker support medium. Then the graphene is transferred to the desired substrate, and the support polymer is stripped with solvent. Our initial transfer process was based on a published procedure [21][22] that used a thin PMMA layer as the support film, and an etching solution of ferric chloride to remove the Cu.

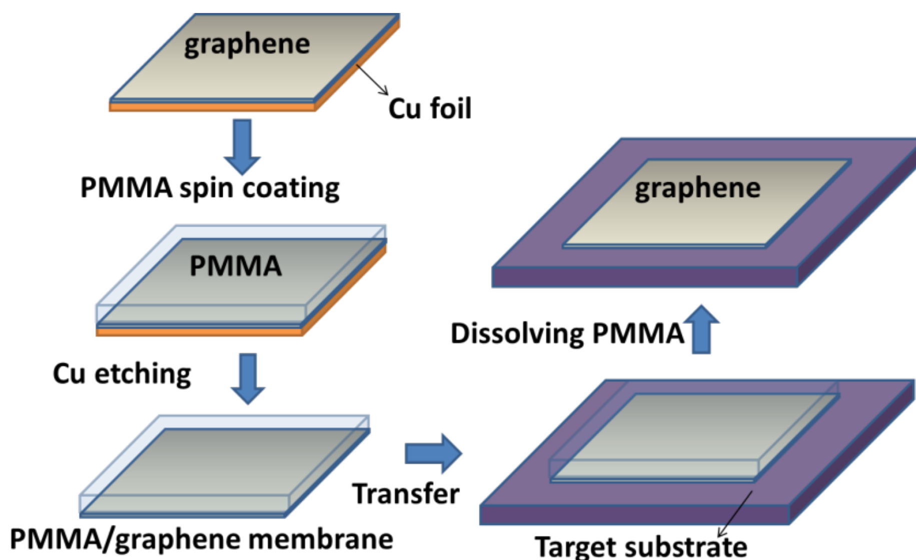

Figure 1.5: **Transfer Process.** A schematic showing the different stages of the transfer process [2]. The graphene/Cu stack is coated in a sacrificial PMMA layer, as the Cu is etched in solution. The graphene/PMMA stack is transferred to a target substrate, and the PMMA is dissolved in solvent.

A schematic of the transfer process is shown in Figure 1.5. Using an iron-based etching solution has the downside of depositing heavy ionic contaminants on the surface of the graphene after the

Cu is removed. A method to clean the graphene surface was adapted from an existing procedure for cleaning wafers of organic and ionic contaminants[23]. A final bath of deionized water was used to rinse the graphene of the chemicals used for the RCA clean. The solutions used for the RCA clean were diluted sufficiently to prevent harm to the graphene. Through subsequent baths in these solutions it was shown that the resulting graphene possessed higher carrier mobility, and lower initial doping than transferred graphene that had not been treated similarly. Using an etching solution free of metallic contaminants allowed for less solution processing, which meant less handling, and less chances to tear the film. We began using ammonium per sulfate (APS) solution in order to etch the Cu foil. The undiluted 15% APS solution caused vigorous bubbling, producing cracks and tears in the transferred graphene film. By diluting the APS solution to 1%, the Cu foil was etched without the vigor of the undiluted APS, and the resulting films were predominantly free of tears and cracks. In addition the films possessed higher carrier mobility, and lower carrier concentration owing to the metal-free solution. Again deionized water was used as the final bath before transfer. The actual transfer was performed by submerging the desired substrate in the deionized water and raising the substrate under the graphene film, drawing the film onto the surface. Ideally the surface of the wafer is prepared beforehand, through a typical oxygen plasma de-scum etch (50W RF power, 5sccm O_2) so that the surface is clean and hydrophilic. The hydrophilic nature of the substrate enables the graphene film to slide on a buffer layer of water, allowing for fine placement. In order to remove this water layer and reduce conformal wrinkles retained by the graphene as it is removed from the terraced Cu surface, the graphene PMMA stack is heated past the glass transition of the PMMA. This causes the PMMA to re-flow and the graphene to conform to the

surface of the target substrate [24]. Once the sample has cooled the support polymer is stripped in the appropriate solvent.

1.2.3.1 Alternate Transfer Techniques

Various new transfer processes were devised, and we attempted many of these in order to compare the quality of the resulting graphene film. Various methods utilizing a particular type of thermal release tape [25], designed to lose adhesion when heated, were tested. The tape was applied to either the polymer support layer or directly to the graphene surface, and then either chemical etchants or a physical separation of the tape and copper were used to remove the graphene from the substrate. Optical and SEM images compare the PMMA and thermal release tape assisted transfer techniques in Figure 1.6. Inevitably the resulting graphene film transferred by thermal release tape had large fissures throughout the once continuous film, likely due to the differences in thermal expansion between the adhesive and graphene upon performing the heat activated detachment. Not only was the graphene film discontinuous, but the additional adhesive created more residue, and the resulting film had lower mobility, and larger doping than methods not involving the thermal release tape.

Another method was introduced in which the etching solution was replaced by $\sim$0.25M NaOH dissolved in water. The electrolytic solution and an external voltage supply were used to produce bubbles on the surface of the copper foil acting as the cathode. Hydrogen gas from the electrol-

ysis forms at the boundary between the graphene and Cu, as long as the electrolytic solution has permeated the interface [26].

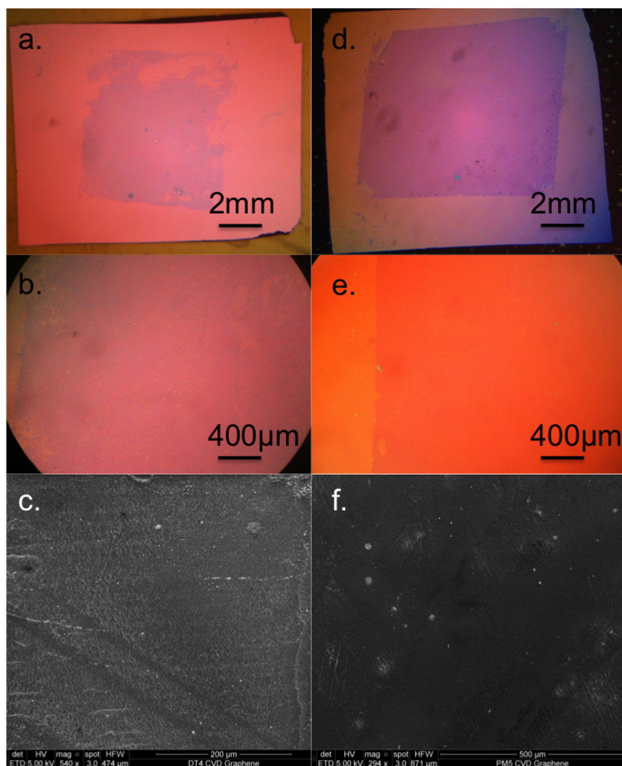

Figure 1.6: **Comparison of Transfer Techniques.** (a) Low magnification optical image of graphene transferred using the thermal release tape method. (b) Optical image of graphene film after thermal release tape transfer showing a variety of voids in the film. (c) SEM micrograph of the same graphene film transferred using thermal release tape. (d) Low magnification optical image of graphene transferred using the PMMA assisted etching method. (e) Optical image of the same graphene film transferred using PMMA, yielding very few voids or tears in the film. (f) SEM micrograph of the graphene transferred using PMMA.

In practice this often results in part of the polymer graphene stack still attaching to the foil as the free section of the film dances in the bubbles of the solution. By tuning the voltage of the power supply, thus adjusting the resulting current, the speed of the gas formation is adjusted, which in turn determines the separation speed. Too much current and the vigorous bubbling would damage the graphene film, while too little current caused the half-secured mess that often resulted in folded films in solution. The separated films were fished out and floated atop a bath of deionized water, efficiently removing any salt from the previous bath. This process produced samples ranging from fair to poor in terms of continuity and size. The electronic properties of the best samples did show some improvement, but the yield was much lower than chemical etching.

Other processes were designed to achieve a transfer free of aqueous processing altogether, preventing any contaminants in the solution from being deposited on the underside of the graphene. We tested a method that relied on the strength of the adhesion of graphene to PDMS film being higher than that between Cu and graphene. The PDMS film is simply brought into conformal contact with the graphene coated Cu and the PDMS film is peeled from the copper, then the graphene is transferred to the polymer substrate [20]. Finally the dry transfer is performed by again placing the polymer film in conformal contact with the target substrate and peeling.We had a great deal of trouble in transferring the entirety of the graphene film with this method, often achieving only very small regions of transfer, which was usually plagued with cracks from handling the flexible intermediate substrate. Although the graphene flakes produced through this method were small and sparse, analysis of the Raman spectra for these films suggested an exceedingly low initial carrier concentration, and the largest mobility of the methods tested.

1.2.4 Raman Characterization

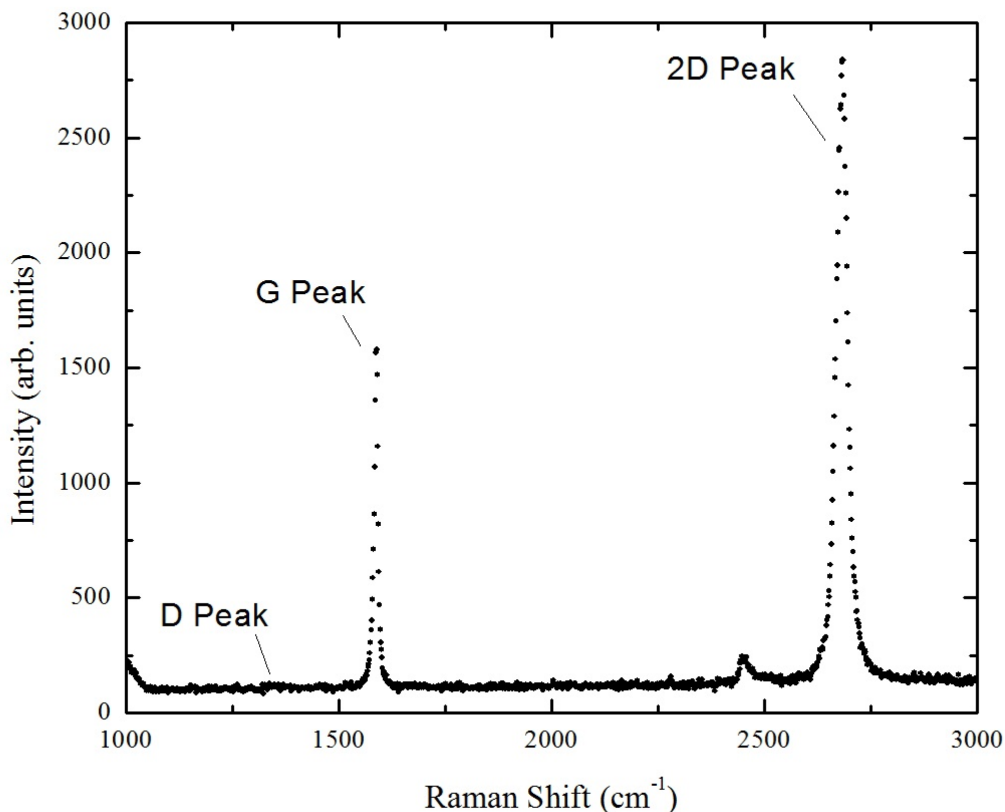

Figure 1.7: **Raman Spectrum of Graphene Film.** Labeled Raman spectrum for a graphene film produced by the rubbing method. The absence of a D peak confirms the high quality of the film. A Lorentzian fit of the 2D peak yields a value of 29.5cm^{-1}, confirming the single-layer nature of this film.

In order to determine the actual number of layers for each of the graphene candidate flakes, the most widely adopted method is the analysis of their Raman spectra. In Raman spectroscopy

the sample is subjected to stimulated electromagnetic radiation, and the reflected light experiences a change in energy due to inelastic scattering and virtual excitation of electrons and phonons in the sample. The predominate peak for bulk graphite, known as the G peak, is due to out-of-plane phonons, and is located at 1580cm^{-1}. If any defects exist in the material, they will contribute to a peak, known as the D peak, which can be found around 1350cm^{-1}. Additionally, as the number of layers decreases there is a third peak, known as the 2D peak, at 2800cm^{-1}. When the graphite flake is multiple layers thick, the lack of a 2D peak causes the 2D:G intensity ratio to be small. For bilayer graphene the 2D:G peak intensity ratio has been found to be close to unity [27]. Graphene's signature Raman spectrum produces a 2D:G ratio larger than 1. Furthermore, a Lorentzian fit to the 2D peak is a more rigorous method to differentiate between single and bilayer; the 2D peak for bilayer is more broad, exhibiting a full-width half-maximum (FWHM) usually greater than 50cm^{-1}, whereas the sharper 2D peak of graphene should have a FWHM less than 30cm^{-1}. To characterize the graphene candidates we used a Renishaw RM 1000B Micro-Raman Spectrometer with an Ar-514nm excitation unit, operating between 5-10mW.

Figure 1.7 presents a characteristic Raman spectrum from one of the graphene flakes produced by the rubbing method. The 2D:G ratio for this particular sample is 1.79, and the FWHM of the 2D peak is 29.5cm^{-1}. There is virtually no D peak, indicating a high quality sample.

In addition to determining the thickness and quality of the graphene, the Raman spectrum holds information about the carrier concentration and defect density. The carrier concentration can be inferred from the G peak position and the intensity ratio between the 2D and G peaks [28]. The defect density of the graphene film can be approximated by using the intensity ratio of the D and

G peaks [29]. The carrier density can be affected by local impurities that are deposited on the substrate or graphene during the fabrication process. These contaminants provide unintentional doping, and can cause the graphene charge neutral point to be far from zero gate bias.

1.2.5 Device Fabrication

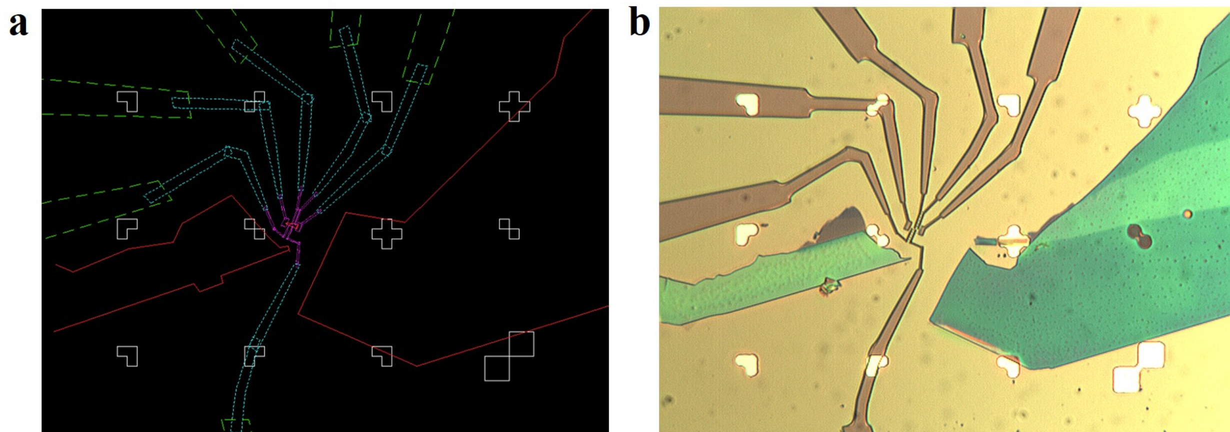

Figure 1.8: **DesignCAD.** (a) A screen capture from the DesignCAD sowftware that shows the pattern to be written. Pre-existing alignment markers (white) are used to size optical images to trace out bulk graphite (red), so that electrodes can be written into the resist using different magnifications for large, medium, and small features (green, blue, and purple, respectively). (b) An optical image of the pattern from (a) after electron beam exposure of the resist followed by development.

Due to the size of the average exfoliated graphene flake, and the necessary customization of each device, the technique used in the fabrication of graphene devices is electron beam lithography. Electron beam lithography allows for many contacts to be placed on flakes below 10μm in size.

The diffraction limit of the UV radiation used in photolithography limits the smallest features to about 2μm or larger. In electron beam lithography the lower limit of features is dependent on the style of SEM but can easily be below 100nm. Our group's SEM, a tungsten filament SEM, was able to produce lines in e-beam resist as thin as 30nm. A field emission SEM is capable of even smaller features, owing to a smaller beam spot. The precision provided by this process was used to create devices with hall bar geometry on even the smallest graphene flakes.

To perform this process we used an SEM outfitted with the Nanometer Pattern Generation System (NPGS). This is a system developed by Joe Nabity, which uses a Computer Aided Drafting (CAD) software, along with direct control of the x and y positions of the SEM's electron beam to position the beam spot in the correct manner to expose the desired pattern into the e-beam resist. Figure 1.8 (a) shows an electrode pattern created in DesignCAD, and the same pattern exposed and developed in PMMA (b). We installed and calibrated this system on our SEM, and developed the procedure for writing devices (see Appendix). A wafer coated with 600nm of more sensitive MMA followed by 400nm of less sensitive PMMA was used as the test case. We designed an array of the same pattern that would be exposed at different dosages, called a dosimitery matrix, to determine the appropriate exposure conditions that our lab was to use. The sample was developed in a 1:3 MIBK:IPA mixture for 60s. A developed dose matrix is shown in Figure 1.9. Patterns without enough exposure time would have unexposed polymer remain, while too long an exposure time would result in the fine features of the pattern bleeding together. The 350μC/cm^2 dosage was the lowest exposure that had cleanly developed in both the large and small segments of the pattern.

This optimal dosage was used to expose the majority of patterns requiring a resolution as low as 100nm.

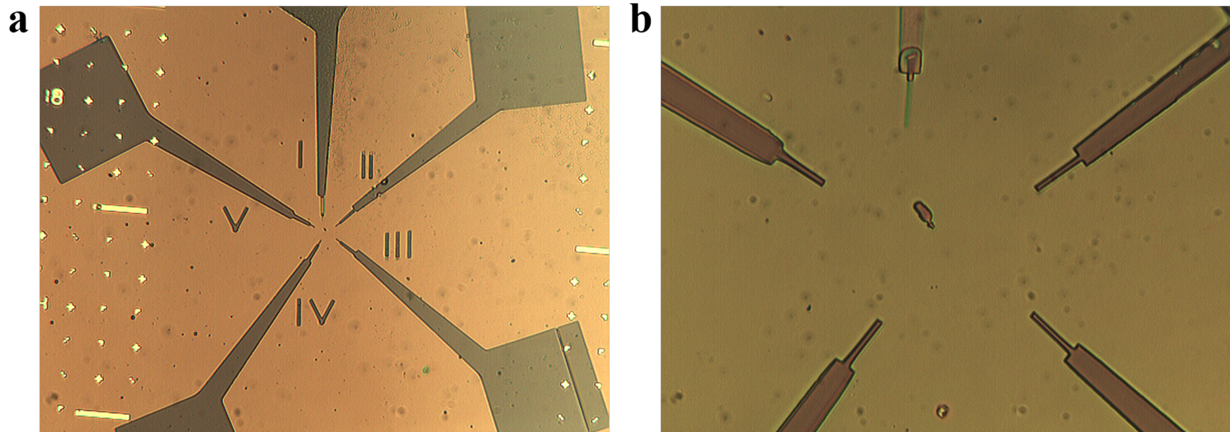

Figure 1.9: **Dosimetry Matrix.** (a) An optical image of a dose matrix, with dosages of 200μC/cm^2 to 400μC/cm^2 in steps of 50μC/cm^2 from I to IV. (b) An optical image closeup of the smallest features of the same dose matrix, showing signs of undeveloped resist in I due to underexposure, and bleeding at the edges of IV due to overexposure.

With the proper dosage setting determined, a pattern could be successfully written into the electron beam resist. A custom pattern would need to be designed in the CAD software so that when metalized the target would have electrodes placed at the correct positions, with leads weaving through obstacles to the contact pads, which would eventually be contacted via a wedge bonder. To do this, optical images are taken of the target after spincoating, as the flakes can move slightly during the coating process. Both the target flake and the closest set of alignment markers must be visible in the optical image, and away from edges that may be affected by lensing by the camera optics. This image is then imported into the CAD software, and scaled so that the alignment

markers in the CAD software lay on top of those in the optical image. Then it is possible to trace the outline of the target in the CAD environment, and proceed to design the pattern accordingly. For samples with thick flakes nearby the design space, it is helpful to import pictures of these in a similar manner and denote where to avoid.

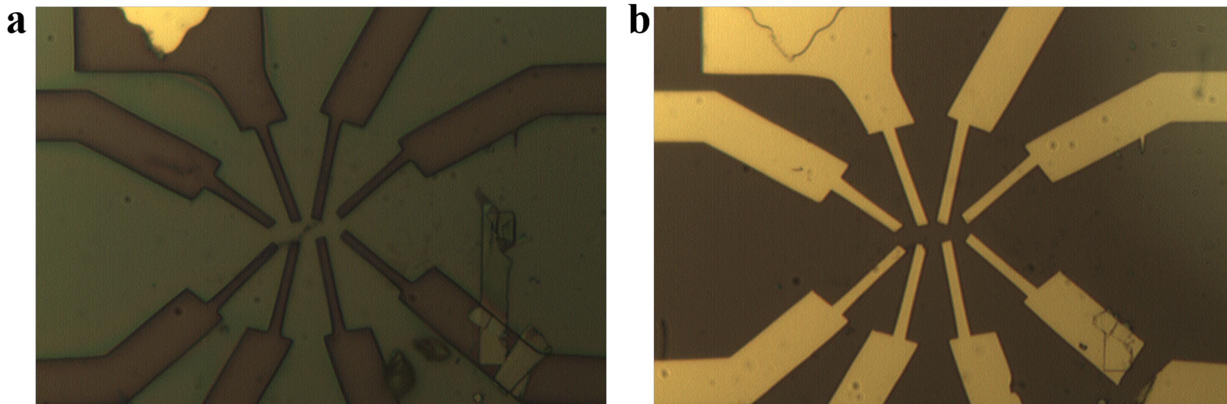

Figure 1.10: **Metalization.** (a) Optical micrograph of a pattern in PMMA/MMA. The E-Beam resist has been exposed and developed, yielding a negative image of the desired pattern. (b) Optical image of the same pattern after metalization and liftoff. The remaining metal has become a positive image of the desired patern.

Two common methods exist for the selective deposition of metal on the surface of a sample. The first is a removal process, by which the surface is first coated in the desired metal, and then a negative image of the pattern is exposed in the polymer. After development the polymer is coating only the desired metal pattern, and by submerging the wafer in an etchant that selectively removes the metal film, the positive image of the pattern is left behind. This process can be performed with either positive or negative resist, but as the chemical etch bath used to remove the metal is an isotropic process, a positive sloping sidewall is more desirable. Since the polymer at the bottom

of the film is thicker, the etching solution makes contact with the exposed metal at the full extent of the pattern, and minimal sidewall etching leaves the patterns true to the design dimensions. The wafer is submerged in the chemical bath only long enough to remove the thickness of the undesired metal, normally on the order of 100nm, so that the thinning of features larger than 1μm are affected by at most 20%. This process is favorable for larger features, as it is reliable and consistent. The alternative is a method known as metal lift-off. In this process a bare wafer is coated with polymer resist, and a positive image is exposed on the surface. By developing the pattern, a coating of polymer covers the entire wafer, except for where the pattern will eventually exist. The desired metal is then deposited on the entire surface of the wafer, and because this is done in high vacuum (1×10^{-6} Torr) the metal is coated via line of sight to the evaporation source. Negative sloping sidewalls or an overhang are desired for this process, as the line of sight is shadowed by the surface of the polymer, and the metal is deposited away from the lower sidewalls. If the thickness of the metal is much lower than the thickness of the polymer then the metal that sits on the wafer surface never makes contact with the polymer. The unwanted metal is deposited on the top surface of the polymer and never makes contact with the wafer surface. When the polymer is stripped in the appropriate solvent it is released from the surface, leaving the desired metal, and carrying with it the unwanted metal. Metal electrodes fabricated using metal liftoff are shown in Figure 1.10. The developed electrode pattern is shown in Figure 1.10 (a), then after metal deposition and liftoff the metal pattern in (b) is created.

1.2.6 Wirebonding

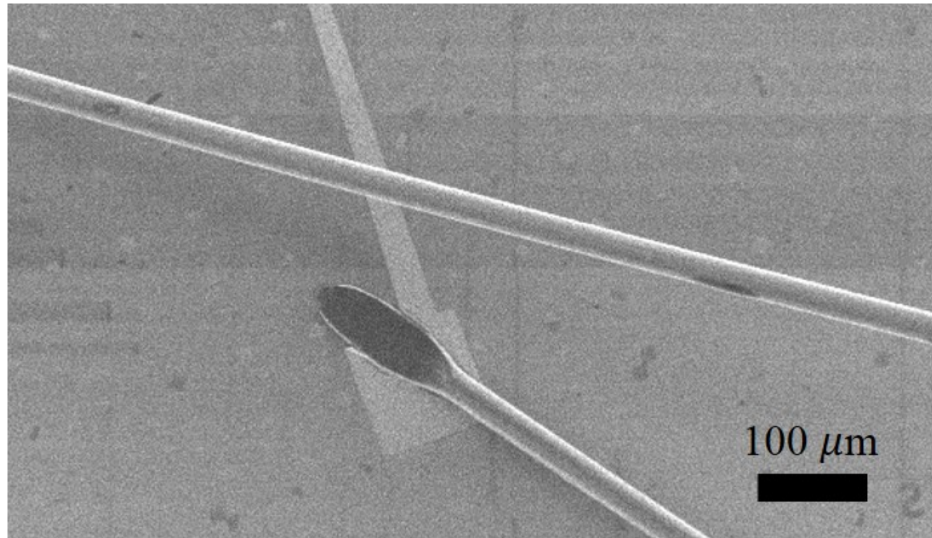

Figure 1.11: **Wirebond.** SEM micrograph of a 1 mil wire that was wirebonded to a 100μm x 100μm contact pad.

Upon completion of the lithography process, a pattern of micron-scale electrodes on a wafer must now be interfaced with macroscopic leads to the measurement instruments. To do this the sample is glued down with epoxy to a package with pins that eventually will interface with a socket on the measurement system. Once the sample is glued down to the package an electrical connection must be made between the 100μm x 100μm gold squares on the wafer surface to the millimeter diameter pads on the package. To do this a special instrument is used called a wirebonder. We used a wedge bonder in particular, which is similar in concept to a sewing machine. A very thin metal wire, 2-mil in diameter, is threaded through a metal rod with a wedge shaped heel. The wire passes below this heel, and when the wedge is pressed down onto a surface it pinches the wire between

the surface to be bonded and the heel of the wedge. When this contact is felt by the machine, and ultrasonic vibration is applied to the wedge, melting the wire with friction to perform the first bond. A clamp on the wire is released, so that the wire can be fed from the spool between the two bonds. The second bond is performed in the same way. Finally the clamp is engaged and the wire is quickly jerked to separate the remaining thread from the bonded metal. A SEM micrograph of a wirebond to a Au contact pad is shown in Figure 1.11. The Al wire was ultrasonically heated and pressed in order to create the flattened wire and melt the Al and Au together.

The sensitivity of our devices to electrostatic discharge (ESD) resulted in many devices that did not conduct after wirebonding. The Kulicke & Soffa wedgebonder used by our research group was a refurbished model, that accommodated heavy use by multiple research groups. The wirebonder manual suggested a yearly maintenance procedure. Unfortunately this had not been performed since the purchase date 5 years prior. An uncalibrated wedge bonder could produce either large surges of current on bonding or, if the bonding force was not set properly, could damage the SiO_2 of the substrate, shorting the device to the back gate. We followed the manual's maintenance procedure, finding that the ultrasonics circuit was not quite perfect. We used trimmers and potentiometers on the instrument board to adjust the resonance frequency of the circuit to the correct value. In addition, the counterweight system used to apply force to the sample was adjusted to meet the correct factory values. Finally, the torque on the washers holding the fulcrum of the bonding tool had to be set to a specific vale using a high accuracy torque wrench. After performing this maintenance, the wedgebonder was no longer found to destroy our devices.

1.2.7 Electronic Transport

By placing source and drain electrodes on graphene and using a local gating structure it is possible to create graphene field-effect transistors (FETs). Applying a voltage on the local gate, V_G, the carrier concentration in the graphene responds by $n = \varepsilon_0 \varepsilon_1 V_G / de$, where e is the elementary charge, d is the gate dielectric thickness, ε is the relative permittivity, and ε_0 is the vacuum permittivity. The field-effect mobility of a graphene device can be calculated using [30][31]

$$\mu = \frac{L}{W} \frac{1}{C_G V_{SD}} g_m \ , \tag{1.5}$$

where L and W are the channel length and width, respectively, C_G is the gate capacitance, V_{SD} is the source-drain voltage, and $g_m = \frac{\partial I}{\partial V_G}$ is the transconductance relating the change in current I and gate voltage V_G.

The characteristic transconductance of graphene, is shown in Figure 1.12 [3]. The resistivity of graphene ρ is measured as a function of back gate voltage V_G. The majority charge carrier for negative values of V_G are holes, while for positive values of V_G the majority carrier is electrons. The ambipolar nature of graphene FET conduction is shown. The mobility is proportional to the slope of this curve, and several regions of mobility can be seen. There is a high mobility region on either side, close to V_G = 0V. As the carrier density becomes larger around V_G = 15V the mobility is reduced. A schematic of the modulation of the Fermi energy is also shown, with the Dirac point, or minimum conductivity point, occurring at the K point between the two conical energy bands.

This is expected to occur at 0V of applied gate voltage, but is often shifted due to unintentional impurities.

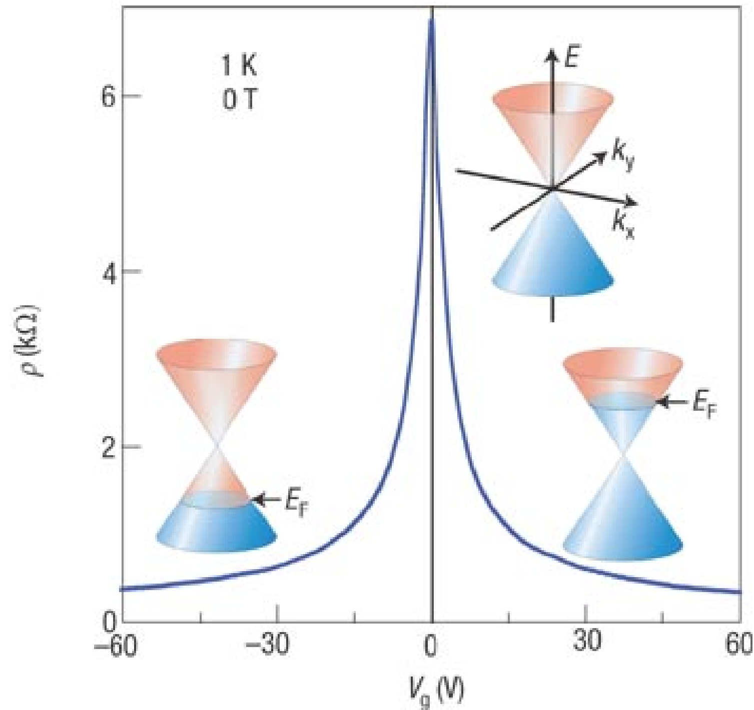

Figure 1.12: **Graphene Transfer Curve.** Characteristic graphene resistivity ρ as a function of the applied gate voltage V_G [3].

The electronic performance of graphene based FETs is affected by interactions with phonons in the substrate, as well as substrate-bound impurities and surface impurities. It has recently been reported that extraordinarily high carrier mobilities are observed by isolating graphene from impurities found in standard substrates [12]. These ultra-high mobility devices are made by suspending graphene above a substrate [15], or by using novel substrates like hexagonal boron nitride [32]. Although substrate isolation produces graphene FETs with extremely high mobility, surface impurities may still be present, contributing to a reduction in mobility and unintentional doping.

Our group has studied the electronic response of graphene to differing levels of surface impurities extensively [33][34][35]. By doping initially clean graphene with impurities in an ultra-high vacuum (UHV, $< 1 \times 10^{-9}$ Torr) environment at cryogenic temperatures, we are able to systematically increase the impurity density on graphene without fear of desorption or additional contaminants. To investigate the effects of long range surface impurities, the conductivity as a function of gate voltage was measured under increasing potassium exposure [33]. It was determined that the presence of these scattering sites led to a reduction in carrier mobility and a shift in minimum conductivity point (MCP) [33]. The reduction in mobility arises from a shorter mean free path for charge carriers in graphene, leading to a larger scattering rate, Γ. The MCP shift is due to doping of the sample, which affects the carrier density, and thus the Fermi energy.

In a related study we used atomic hydrogen to probe the effect of physisorbed hydrogen on bulk graphene [34]. As in the case for potassium (long range), the presence of physisorbed hydrogen (short range) decreased the carrier mobility and results in n-type doping with increasing coverage. In these studies the effect of impurities on the graphene FET was to decrease the mobility, and impart a nonzero Fermi energy at zero gate voltage.

1.2.8 Graphene Device Post-Processing

A study on the surface morphology of graphene [36] showed that the graphene surface is contaminated by a layer of residual polymer after conventional device fabrication. Using either photoresist or e-beam resist assisted fabrication of electrodes on graphene resulted in a difficult to remove

residue after stripping the polymer in the appropriate solvent. This residue was able to be removed by annealing the sample in a H_2/Ar atmosphere at 400°C. Using a scanning tunneling microscope (STM) before and after this treatment showed that atomic resolution of the graphene surface was only achieved after annealing. This surface layer complicates any experiment that is probing the impact of local impurities on the graphene surface. In addition, the electrical properties of graphene are very sensitive to the local environment of the film, and this residue can negatively affect these properties.

Many studies confirmed that indeed this residue was responsible for a decreased carrier mobility in the graphene. Moreover further methods for cleaning the graphene film were developed to combat these negative side effects of conventional device fabrication [37]. Many claims of improved electronic performance and surface cleanliness were reported [38][39], but there was no standout method adopted by the majority of research teams. In fact, it was reported [38][40] that some cleaning methods would go beyond improvement, and started to degrade the electrical performance. We wanted to characterize the various cleaning methods, and put a threshold on this degradation.

We wanted to test the effectiveness of each one of these methods, but certain processes were more difficult to control than others. The current annealing procedure was deemed too inhomogeneous of a process to explore. In addition the device throughput was lower than the other methods. With our instruments the device throughput of vacuum annealing was similarly very low. We decided based on the uniformity of the processing, and the high device throughput, the chloroform clean and furnace annealing would be the two processing techniques to explore.

1.2.8.1 Methodology

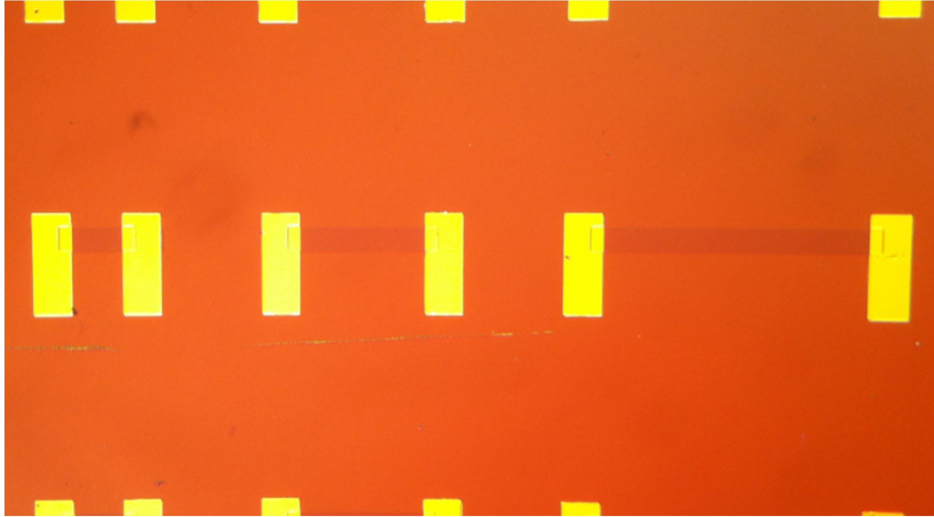

Figure 1.13: **Two-probe CVD Graphene Devices.** Optical image of patterned graphene between two electrodes made of pure gold.

We transferred CVD graphene to Si/SiO_2 wafer using the PMMA assisted etching method. Gold contacts were deposited on the graphene without the usual sticking layer of chromium. The contact resistance for two-probe devices made using pure gold contacts instead of gold/chrome contacts were measured to be much lower. The CVD graphene was then patterned into channels using photolithography. To simulate the more ubiquitous device fabrication by electron beam lithography, a buffer layer of PMMA was deposited on the graphene film before the photoresist layers. Graphene channels were defined in a negative photoresist, resulting in a thicker resist layer on top of the desired graphene. The unwanted graphene was etched using reactive ion etching. The protective polymer layer was then removed in the appropriate solvent, resulting in arrays of two-probe devices, as shown in Figure 1.13.

The samples were measured using a Keithley semiconductor parameter analyzer to extract various electronic characteristics such as carrier mobility and doping level. This was achieved using a probe station, which allowed for measurement without wirebonding after each processing step. We measured the samples directly after device fabrication in order to establish a baseline for these parameters. Half the samples were then subjected to the wet cleaning in chloroform solution, and then measured once again. The remaining samples were characterized after subsequent 2h annealing processes in H_2/Ar (4:96%) atmosphere at 200°C, 250°C, and 300°C.

1.2.8.2 Results

The transfer curves for a characteristic sample after the various processing methods is shown in Figure 1.14. The black curve, taken directly after fabrication has the lowest conductance overall, and a minimum point around 38V is barely visible. The slope of the transfer curve for the as-made sample is very low, with a hole mobility of only 38 cm^2/Vs. The conductance increases slightly for the chloroform clean (red), but the mobility and doping show very little sign of improvement. The 200°C anneal (blue) resulted in the largest change. The mobility increased to 50 cm^2/Vs, and the intrinsic doping level decreased, evidenced by a 13V shift in the MCP. The overall conductance is also increased with an anneal at this temperature. After annealing at 250°C (pink) this graphene device exhibited an increase in conductance, but a decrease in carrier mobility back to the initial value. Additioonally this device showed an increase in doping, shifting the minimum point to about

30V. Upon annealing at an even higher temperature of 300°C (green) the mobility and doping level no longer change, but the overall conductance decreases.

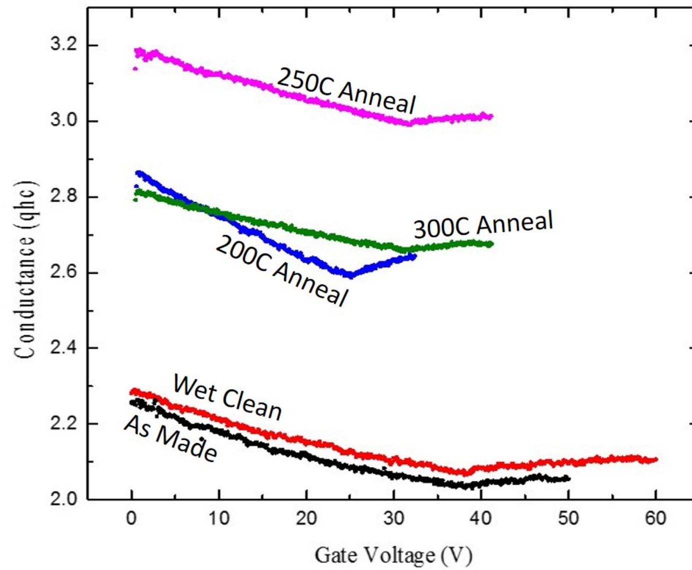

Figure 1.14: **Post Processing Transfer Curves.** Graphene transfer curves shown after device fabrication and other cleaning processes. The conductance versus gate voltage of the as-made sample (black), is compared to that of the chloroform cleaned sample (red), and the sample annealed at 200°C (blue), 250°C (pink), and 300°C (green).

This procedure was performed for over 80 devices to extract statistics about these cleaning processes. The change in hole mobility is an important indicator of improved electrical performance. Figure 1.15 shows the change in mobility for all 80 sample for chloroform cleaning (a), annealing at 200°C (b), and annealing at 250°C (c). The low survival rate for samples annealed at 300°C prevented the acquisition of good statistics for that temperature. The wet cleaning process

resulted in the only positive average mobility change. Both H_2/Ar annealing processes produced graphene samples with mobility lower, on average, than the initially made samples. Although subsequently higher temperature annealing was able to slightly recover the mobility of these samples. These results are contrary to the results published by others [38][40], and could be due to lower quality CVD graphene or furnace cleanliness. Though not conclusive, these results did indicate that the parameters of the cleaning process can be very crucial to improving graphene's electronic properties.

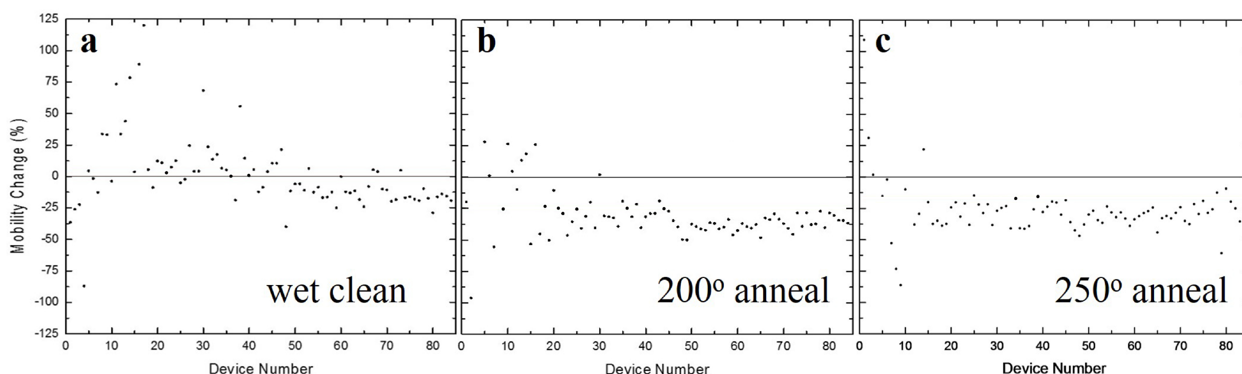

Figure 1.15: **Change in Graphene Mobility for Different Processing Techniques.** The mobility change of over 80 devices after various forms of post-process cleaning. (a) The effect of wet cleaning, or chloroform cleaning, on 80 graphene two-probe devices. The effect of thermal annealing at 200°C (b) and 250°C (c) for over 80 graphene two-probe devices.

1.3 Electrode Transfer

1.3.1 Background

In an additional attempt to explore methods of creating devices free of the damage caused by conventional lithographic device fabrication [41], we tested alternative methods to place metal electrodes on the surface of graphene. In addition to residue, the electron beam irradiation used to define electrodes in the polymer atop graphene was found to be responsible for device degradation [42]. The e-beam device fabrication step used by so many research groups to place electrodes on the graphene film was called into question.

In an attempt to fabricate devices without the damage accompanied by electron beam lithography, methods were devised to transfer electrodes to graphene without the electron beam making contact with the film. Some work in this regard had shown that this electrode transfer was possible with gold patterns deposited on top of SiO_2 capped silicon wafer [43][44]. Gold electrodes can be encapsulated in a polymer layer, and then transfered from one substrate to another in a method similar to CVD graphene transfer. The encapsulated electrodes can be separated from an oxide coated wafer by immersion in buffered oxide etch (BOE). We devised a simpler method for this process that utilized a water soluble layer atop the SiO_2, allowing for electrode transfer without the use of BOE.

1.3.2 Methodology

Silicon wafers with 280nm of thermally grown silicon oxide were used as a substrate, atop which a thick layer of Aquasave was formed by spinning at 3000RPM for 1 minute. Then MMA was coated at 4000RPM followed by a layer of PMMA at 4000RPM. This resulted in layer thicknesses of 600nm and 400nm for the MMA and PMMA, respectively. The pattern specific to a graphene film on a separate chip was written into the polymer, and developed in IPA:MIBK 1:3 for 60s. The sample was immediately placed into the thermal evaporation chamber, where Cr and Au were deposited at 1×10^{-6} Torr to reach the desired thickness of 2nm and 80nm, respectively. Acetone and PG remover both resulted in the liftoff of the Aquasave layer. Dioxane was found as a selective liftoff solution, leaving behind the wafer with Aquasave and gold contacts on top. Then MMA was coated at 4000RPM followed by 4 layers of PMMA at 4000RPM with a 175°C bake for 10 minutes in between each layer. This produced a very thick ($> 1\mu$m) layer of polymer, which was found to be beneficial for structural integrity throughout the transfer process. A target sample was then coated with an adhesion promoter, HMDS, and then a drop of PMMA was used to glue the two coated surfaces together. The polymer sealed electrode pattern was then able to be separated by submerging the wafer in deionized water. The Aquasave was selectively dissolved in the water, and the film supporting the electrode pattern was left behind on the underside of the target surface. Then, using an optical microscope with long range objective lenses, the film could be aligned to the target flake. This alignment process proved to be very challenging, and care during the drying

stage was taken to avoid unintentional repositioning of the electrodes. If performed correctly, the electrodes could be deposited, and then the supporting polymer dissolved away in acetone.

1.3.3 Results

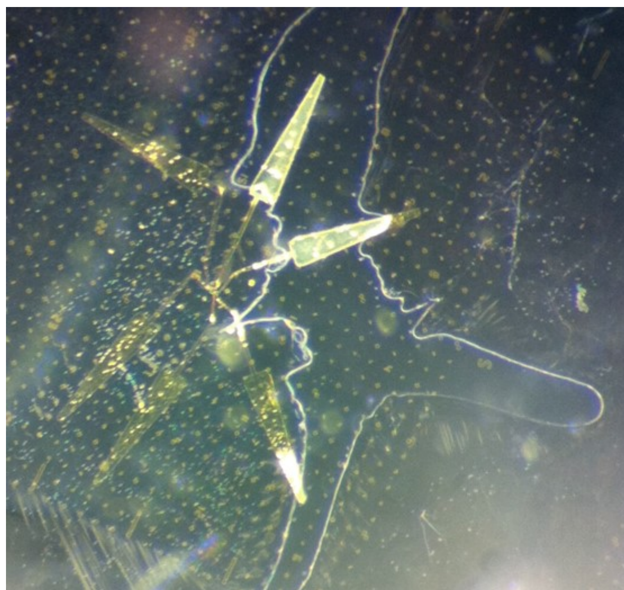

Figure 1.16: **Electrodes transferred to Transparent Substrate.** Partially transferred electrode pattern at 100x magnification. The brighter gold has been transferred to the transparent substrate correctly.

The particulars of the layer compatibility were a hurdle in this process. The correct solvent, baking temperature, and adhesion promoter were all chosen carefully as to not change the layer properties. Aquasave in direct contact with PMMA would become difficult to remove, so an MMA buffer layer was a necessity. A polymer support too thin produced tears that would result in only a

portion of the electrodes transferring to the intermediate wafer. Figure 1.16 shows an electrode pattern that has only been partially transferred to a transparent quartz substrate. The bright electrodes are on the underside of the quartz, while the dull gold pattern remains on the original substrate.

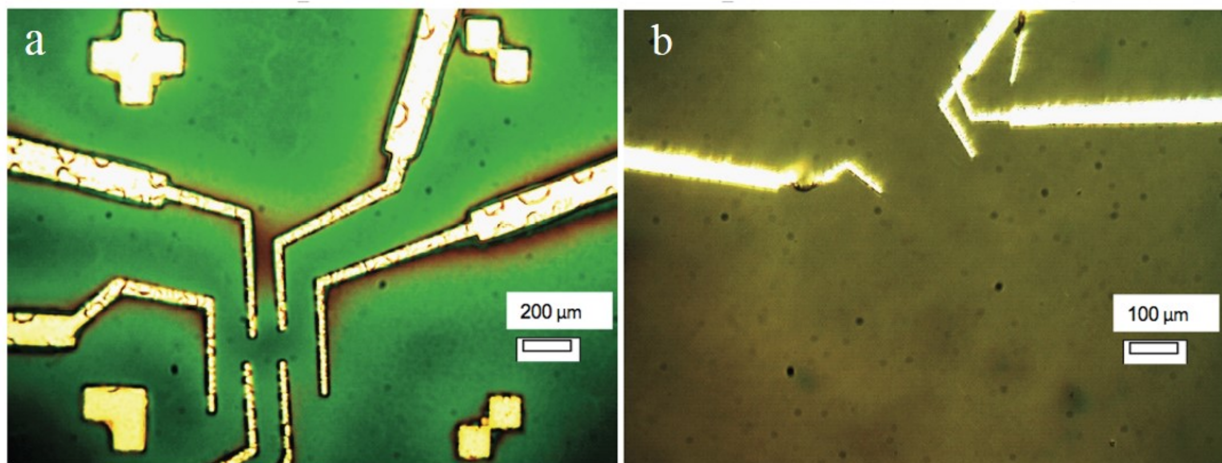

Figure 1.17: **Electrodes transferred to Target Substrate.** (a) Electrode pattern encapsulated in polymer on top, and Aquasave below. The same electrode pattern, after partial transfer to target substrate. The larger features transferred more successfully, but the fine features in the center show signs of incomplete transfer.

Once the electrodes were successfully transferred to the quartz substrate, careful alignment was needed to place the electrodes on the target surface. We were never able to successfully place the electrodes onto a graphene film. Once brought into conformal contact, it proved difficult to promote the adhesion of the contacts to the target wafer. Various heating temperatures were tried, and a temperature of 380°C or higher was able to remove PMMA, while retaining the electrode position. Unfortunately some of the electrodes would be secured to the desired substrate, while others would be affixed to the transparent carrier substrate. Figure 1.17 shows an optical image of

the encapsulated electrode pattern to be transferred (a) and the result of the transfer is shown in (b). The accuracy, and successful yield of this method was never high enough for adoption.

CHAPTER 2
GRAPHENE NANORIBBONS

2.1 Background

The poor applicability of graphene to digital circuits is due to the low on-off ratio of the material. It was predicted that electronic bandgaps would form in graphene constricted regions, and it would behave according to lattice orientation and edge type termination [45][46]. Many studies were then conducted in order to attempt to create this bandgap [47][48][49]. Although these groups measured regions of very low conductivity, it was argued whether the graphene nanoribbons actually exhibited bandgapped behavior. Unfortunately the lithographic conscription process used to fabricate these nanoribbons out of graphene are not of sufficiently high resolution to produce precise edge termination. Contrary to the perfect edges used in theoretical studies, the edges of the constrictions made using electron beam lithography and reactive ion etching are rough and disordered.

The transport properties of these graphene constrictions are characterized by insulating behavior at certain source-drain bias voltages V_{SD}, as well as certain gate voltages V_G. These regions of very low conductance are referred to as the source-drain gap and the gate gap, or transport gap. Predictably, these gaps do not correlate to the theoretically predicted electronic bandgaps. Instead, substrate-bound charged impurities are suspected to be responsible for these observed regions of

very low conductance [50][51][52]. It is then suspected that the electrical potential fluctiations induced by these charged impurities, combined with the width variation produced by the lithographic constriction process, are thought to create carrier paths similar to those observed in quantum dots [52]. We designed an experiment in order to test the effect of charged impurity density on this system. Graphene nanoribbons would be annealed in order to remove existing impurities, and to free the surface of polymer residue. Then, in UHV the graphene nanoribbon would be exposed to cesium. The cesium would follow a line of sight to the graphene nanoribbon, attach to the surface, and was expected to donate an electron. This would result in a cesium ion on the surface of the graphene ribbon. The exposure time to the cesium would directly relate to the charged impurity density on the nanoribbon surface, and electronic measurements would be performed at varying levels of impurity density.

2.2 Methodology

Graphene nanoribbon devices were fabricated using graphene exfoliated from kish graphite. We used the rubbing method to isolate thin graphite flakes free of the tape residue and bulk graphite associated with samples prepared by tape exfoliation. Raman spectra of the graphene candidates were used to confirm the single-layer nature of the films. These graphene sheets were exfoliated atop heavily doped silicon wafer capped with 280nm of thermally grown oxide. The silicon would act as the back gate for the field-effect transistor structure. The sample was coated with 600nm of MMA and 400nm of PMMA. We defined electrodes in e-beam resist, and used the SEM and

CAD software to design custom electrodes for each graphene film. The graphene was divided into segments, separated by parallel contacts, later to become two-probe channels. The graphene segments could be thinned down to varying widths, creating a graphene nanoribbon width gradient.

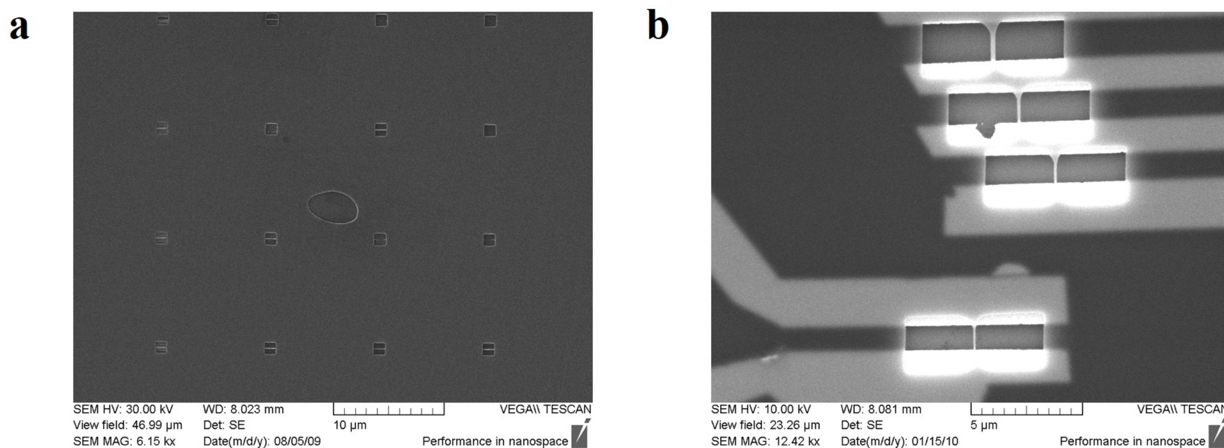

Figure 2.1: **SEM Image of Etch Matrix and Nanoribbon Etch Mask.** (a) SEM micrograph of nanoribbon etch mask matrix with different dosage and geometrical parameters. Regions with no visible ribbon in the developed mask had either too high a dosage or too thin a ribbon design. (b) Nanoribbon etch masks over graphene between pairs of electrodes. The graphene has been etched away, and the remaining graphene is protected by the visible etch mask, that when removed leaves behind a graphene nanoribbon.

During this initial exposure, a set of additional alignment markers were exposed in the region close to the graphene film to aid in the subsequent writing processes. The contact pattern was developed in IPA:MIBK 1:3 at room-temperature, and then Cr and Au was evaporated on the wafer at 1×10^{-6}Torr at 2nm and 80nm thickness, respectively. The unwanted metal was lifted off in an acetone solution with light agitation at 60°C. The sample was dried, and a fresh layer

of PMMA was applied to the surface. This second lithography step was used to define the shape of the nanoribbon, by using reactive ion etching (RIE) to remove the unwanted graphene, while the graphene constriction was protected under the polymer. The MMA undercutting layer was unnecessary, and the device can be coated in only the PMMA resist, which withstands the etching times necessary to remove graphene. This time PMMA A2, a different formulation with lower concentration of polymer solids, was spincast on the surface of the graphene device at 6000RPM. An electron beam sensitive layer only 50nm thick was the result, and this very thin layer was crucial in achieving nanoribbon widths below 100nm. Incident electrons are scattered as they travel through the polymer film and secondary methods of exposure combine to cause a bleeding of the pattern when writing very fine features into thick resist. Using a resist that was ten times thinner than normal alleviates much of the scattering that leads to fine features merging upon development. For the fine writing, a beam current of 4pA was used, with a spot size of about 30nm. The alignment markers deposited with the electrodes were much smaller than the normal markers, and in a tighter array, allowing for more precise alignment at a much higher magnification. The second alignment takes place at 2000x magnification, with 1μm x 1μm patterns. The etch pattern was then exposed into the graphene, whereby the developed regions will later be exposed to the plasma and removed. A thin strip of polymer connects the two contacts, with designs anywhere from 100nm to 10nm wide and 500nm long. As the plasma etch was anisotropic the sidewalls of the protective mask were etched as the graphene was etched. This thinning of this protective strip has been accounted for by the array of various width ribbons on each graphene nanoribbon device. The smallest width etch masks get completely removed, with no graphene ribbon remaining after

the etching process. The larger width etch masks were thinned, but survived the etching process. The width gradient allowed for the thinnest possible graphene constriction, even in the face of minute changes in beam profile, resist makeup, and etching parameters. Figure 2.1 shows a SEM micrograph of a diagnostic etch matrix (a), allowing exposure parameters to be tuned for minimum ribbon thickness. A SEM micrograph of a graphene nanoribbon etch mask after the unwanted graphene was removed is shown in Figure 2.1 (b).

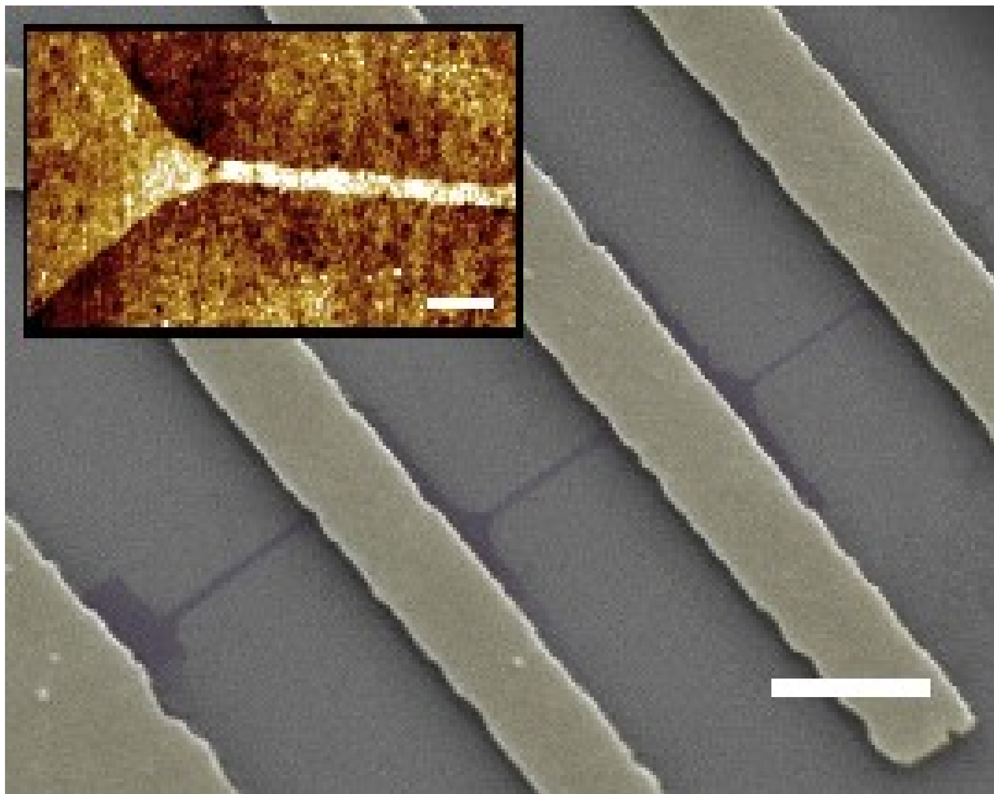

Figure 2.2: **SEM and AFM Images of Fabricated Graphene Nanoribbons.** Scanning electron micrograph of a typical device configuration (false color). Graphene Nanoribbons (purple) are lithographically defined between electrodes (gold). Scale bar is 2μm. Inset shows an atomic force micrograph of an atomically clean nanoribbon before measurement. Scale bar is 200nm.

Figure 2.2 shows a false color SEM micrograph of a characteristic graphene nanoribbon device. The inset of Figure 2.2 shows an AFM measurement of the graphene nanoribbon device for which experimental data will be presented. These nanoribbon devices were then subjected to annealing in a H_2/Ar atmosphere at 300°C for 3 hours at atmospheric pressure. This was done to produce a surface cleaned down to the atomic scale [36]. The clean devices were then bonded and placed on the cold finger of a helium flow cryostat, and pumped into a UHV transport chamber. The graphene nanoribbon was then annealed at 495K for 20h to remove any surface adsorbed impurities prior to doping. At UHV pressures the graphene nanoribbon was exposed to a constant cesium flux (Figure 2.3 (a)), produced by a cesium getter. Using a residual gas analyzer and partial pressure measurements we estimated the dose rate to be ~ 0.09cesium $s^{-1}\ \mu m^{-1}$.

2.3 Results

We measured the transport properties of a graphene nanoribbon 40nm wide, and 900nm long (Figure 2.2 (b) inset) at low temperature. The undosed ribbon exhibited the thermally activated gapped behavior reported by others [47][48][49]. The inset of Figure 2.3 (b) shows the measured transconductance of the 40nm width graphene nanoribbon at 270K, 95K, and 11K. A thermal activation energy of 6.56meV was extracted from a best fit to an Arrhenius plot, shown in Figure 2.3 (b). This thermal activation energy is similar to the value measured by others for nanoribbons of this size [53]. The field-effect mobility of the graphene is found to be 360cm^2/Vs and 410cm^2/Vs before dosing for holes and electrons, respectively.

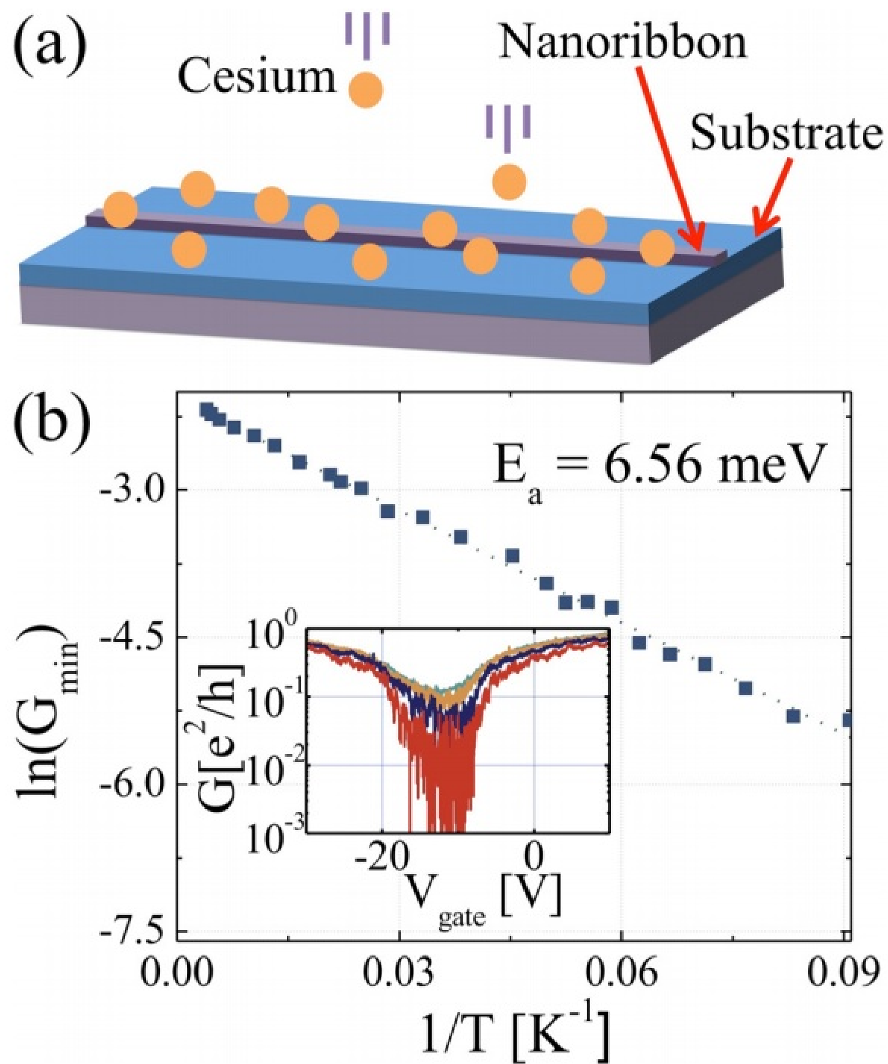

Figure 2.3: **Experimental Schematic and Initial Measurement.** (a) Schematic showing the graphene nanoribbon under the presence of a cesium flux. (b) Arrhenius plot showing the minimum conductance of the gate voltage scan for the 40nm graphene nanoribbon studied, prior to cesium dosage. The inset shows transconductance measurements performed at 270K, 95K, and 11K.

The graphene nanoribbon was cooled to 11K before cesium exposure, to limit thermal desorption. Figure 2.4 shows the transconductance of the 40nm wide graphene nanoribbon under increasing cesium coverage, with cesium dosage time given. Increasing cesium coverage reduces the field-effect mobility, increases n-type doping (shifting the charge neutral point to increasingly negative values), and affects the source-drain and gate gaps.

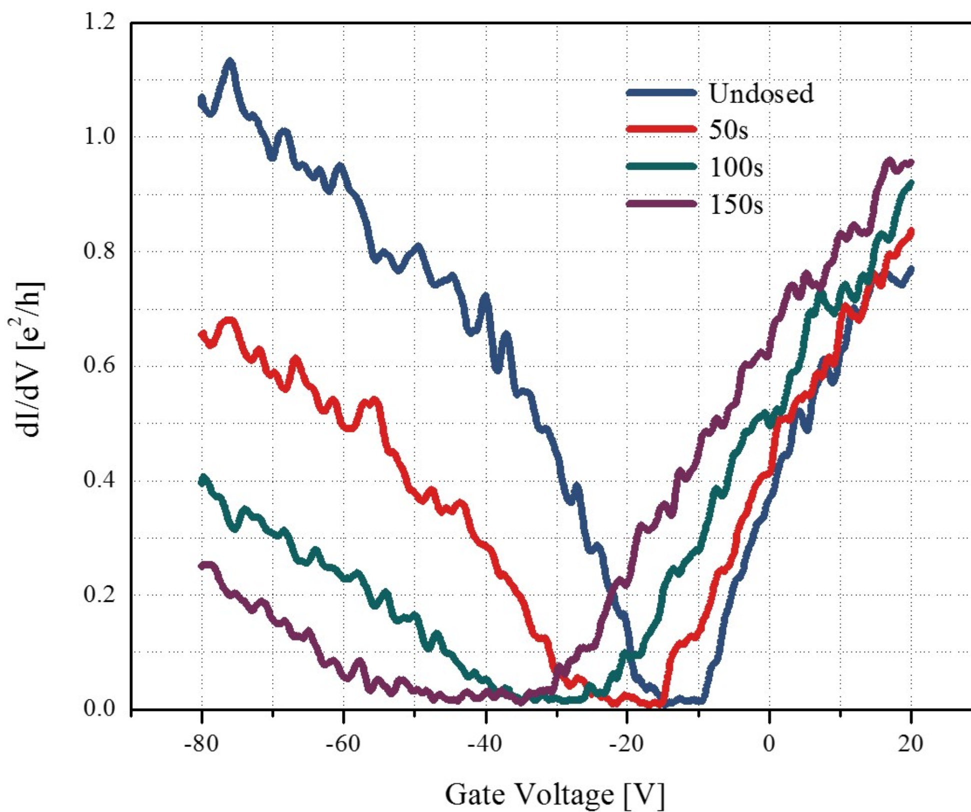

Figure 2.4: **Transconductance of Graphene Nanoribbon.** Transconductance measurement of 40nm-width graphene nanoribbon. Curves are shown for 4 increments of dosage time.

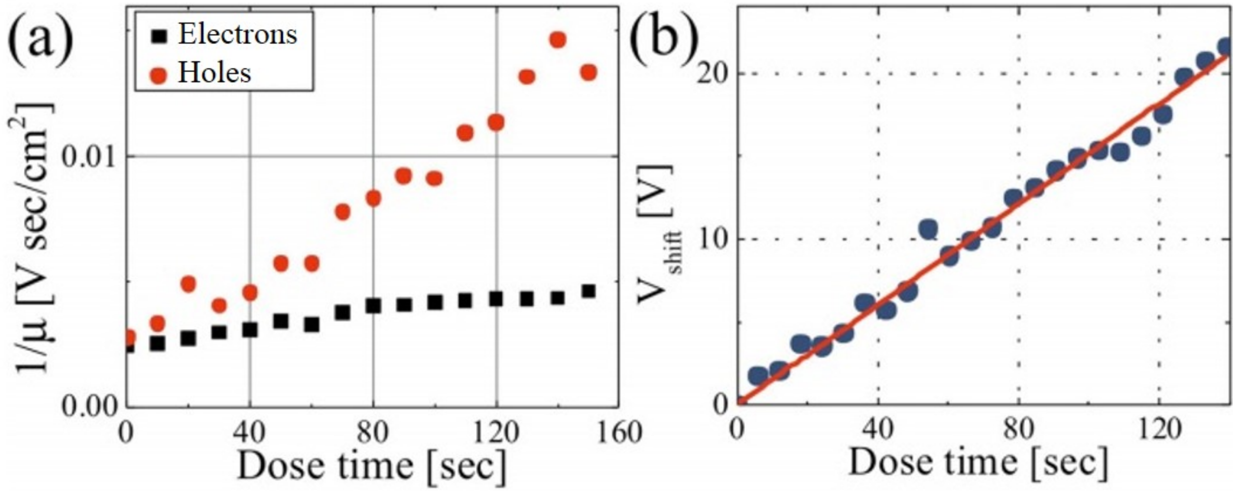

Figure 2.5: **Inverse Mobility and MCP Shift for Graphene Nanoribbon.** (a) Inverse mobility in the presence of increasing impurity density. (b) Minimum conductivity point shift as number of charged impurities is increased.

The effect of increasing impurity density on the electron and hole inverse mobilities, as well as the shift of the minimum conductivity point are presented in Figure 2.5 (a) and (b), respectively. The inverse electron mobility shows a sub-linear behavior under increasing dosage time, while the inverse hole mobility shows a super-linear dependence. Linear dependence on charged impurity density is to be expected from diffusive transport in graphene [50]. Our data may indicate that Boltzmann transport theory alone may be unable to describe scattering due to charged impurities in nanoribbons. A linear fit well describes the charge neutral point shift, with an approximate slope of 0.15V/s of cesium dosage. Using the geometric capacitance formula with a phenomenological reduction factor of 2 [54], it is found that 0.29electrons s^{-1} μm^{-1} are added to the nanoribbon. This corresponds to about 0.6-0.8 electrons transferred from each adsorbed cesium atom according

to our flux calculation, which was based on cesium partial pressure [55]. This linear dependence is different from bulk graphene, where V_{shift} has a super-linear power law dependence on the charged impurity density [33]. This indicates that the charge screening in bulk graphene is different than that in graphene nanoribbons.

2.4 Discussion

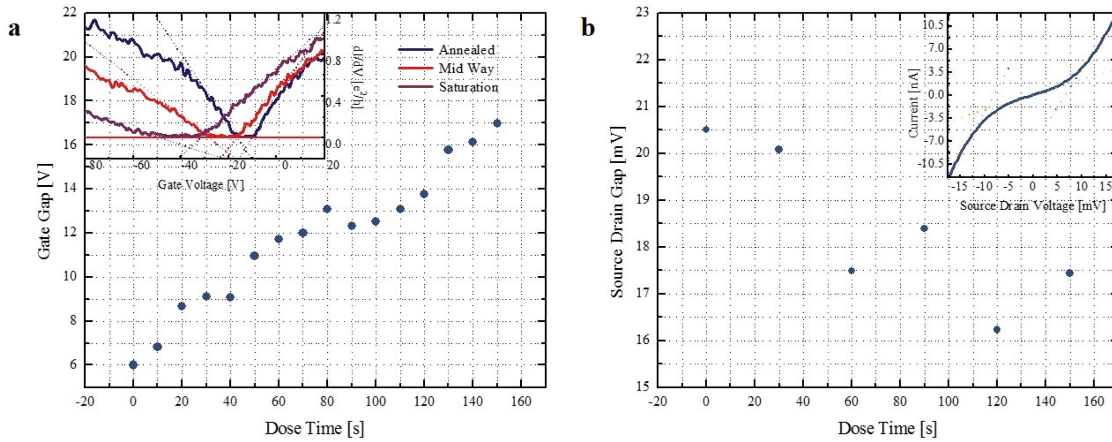

Figure 2.6: **Nanoribbon Gap Behavior for Cesium Dosage.** (a) The relationship between the gate gap and the number of added impurities for 40nm width graphene nanoribbon. (b) The effect of added impurities on the source-drain gap for the same graphene nanoribbon. Insets show gap characterization.

In order to characterize these gaps, we developed a routine in the coding language Python. For the gate gap the code determined a best fit linear line on each side of the transconductance curve,

and extrapolated this fit to the zero conductance region. The region between these intersections defined the width of the gate gap, and has been used to quantify this gap [51]. Similarly, for the source-drain gap, the code fited a linear line on each side of the non-linear conductance region near zero bias, and extrapolated these fits to the zero current line. These intercepts give the source-drain gap width. Figure 2.6 shows these extracted gap values under increasing cesium flux time. The gate gap is observed to increase under the presence of increasing charged impurity density. In the framework of conducting islands caused by potential fluctuations this is to be expected. The added cesium increases these potential fluctuations, further confining the regions of allowable conductance. In comparison the source-drain gap is reduced for increasing cesium dosage. This behavior is consistent with the charged impurity theory in which the source-drain gap is dependent on the size of the smallest dot, with the charging energy inversely proportional to the size of this dot [53]. Since the adsorbed cesium is expected to be situated 2.8Å away from the graphene surface [55], compared to substrate bound impurities assumed to be more than 1nm away [50], the potential fluctuation is more sensitive to the cesium density. The source-drain gap charging energy is inversely proportional to the size of the smallest dot, therefore the adsorbed cesium is creating taller fluctuations over larger regions, thus reducing the size of this gap.

A common method for determining the conductance properties for quantum dot systems is to measure the channel current over a wide range of source drain voltages, as well as gate voltages. This results in a graph known colloquially as a “diamond plot” due to the diamond-like shapes that are typically produced. The size and shape of the minimum conductance regions of these plots can

be indicative of the size of the smallest quantum dot, and is useful for determining the smallest conducting island in the nanoconstriction.

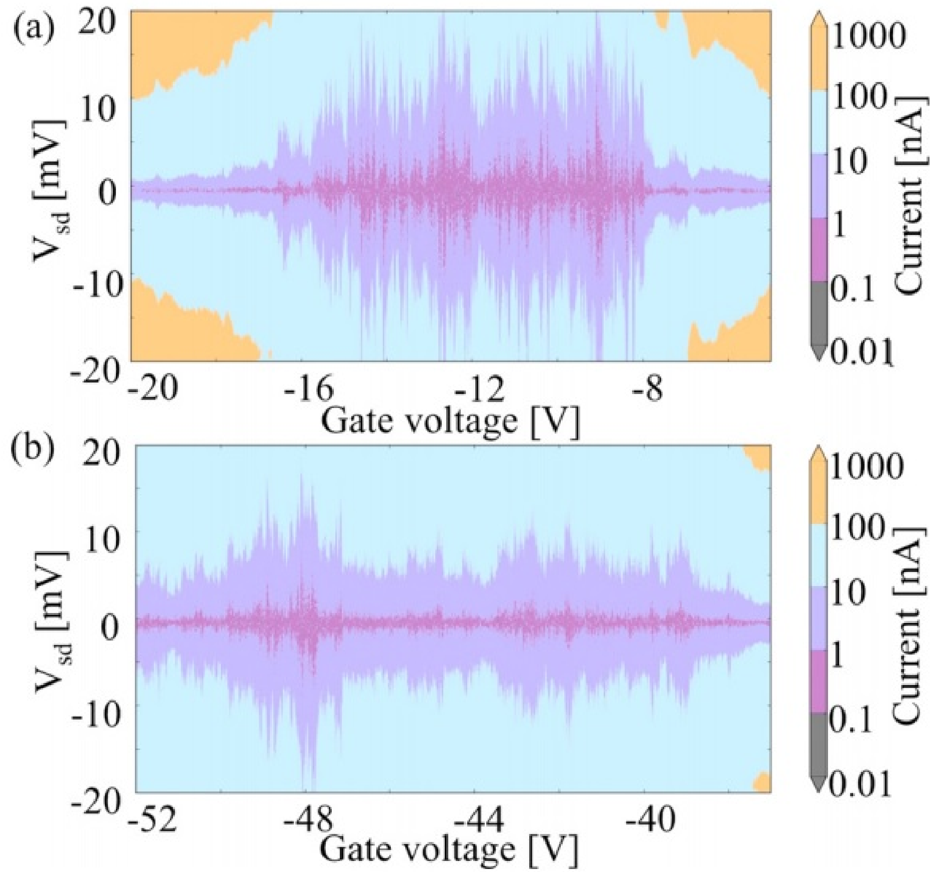

Figure 2.7: **Graphene Nanoribbon Contour Plot.** Current through a graphene nanoribbon for a wide range of source-drain and gate voltages. Measurements were performed on the pre-dosed ribbon (upper), and fully dosed ribbon (lower).

Figure 2.7 shows the current dependence of our graphene nanoribbon for a wide range of source-drain and gate voltages. It is evident that the width of the low conductance gate voltage region increases upon dosing, but the average low conductance source-drain voltage region decreases.

This observation enforces the conclusion above, showing that the gapped regions are more plentiful (gate voltage), but with a smaller charging energy (source-drain voltage).

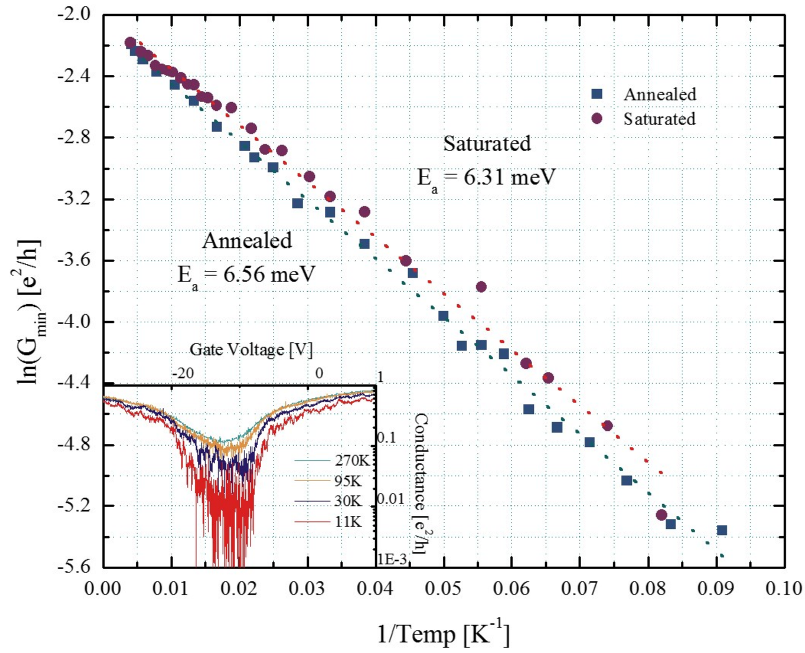

Figure 2.8: **Arrhenius Plot for Annealed and Dosed Graphene Nanoribbon.** Arrhenius plot showing the dependence of the minimum conductance on the temperature of the graphene nanoribbon. Thermal activation energies are shown for both annealed and saturated graphene nanoribbons. The inset shows the temperature dependence of the transconductance.

The last parameter that has a large effect on the conductance of the graphene nanoribbon is temperature. Before dosing the thermal activation energy was calculated to be 6.56meV. Figure 2.8 shows the measured minimum conductance of the graphene nanoribbon for a range of temperatures

before and after dosing with cesium. The thermal activation energy E_a is related to temperature T by

$$G_{min} = e^{E_a/2k_BT} \tag{2.1}$$

where G_{min} is the minimum conductance measured over the full range of gate voltage, and k_B is Boltzmann's constant. The temperature dependent measurements performed before and after dosing allow for extraction of the thermal activation energy, which is observed to change from 6.56meV to 6.31meV. The regions of suppressed conductance are observed to depend not only on the temperature and size of the ribbon, but also on the size and density of the potential fluctuations caused by local impurities. Thus for thinner nanoribbons measured at lower temperatures the effect of these added impurities may be more elucidating.

2.4.1 Increasing Insulating Behavior

In an attempt to see more of a conductivity gap in our graphene nanoconstrictions, we made many attempts to both lower the measurement temperature and reduce the ribbon width. The helitran used to perform the graphene nanoribbon transport measurements was able to typically reach stable temperatures around 10K. This was possible by completely opening up the needle valve used to throttle the helium exhaust. By doing this the helium was allowed to flow more freely, consuming more liquid helium, but bringing the cold finger to lower temperatures. One way we learned to bring the cryostat to lower temperatures was to, in effect, pull helium through the helitran by using

a high volume rough pump on the exhaust port. Even more liquid helium would be consumed, but the temperature could approach the limit of liquid helium-4 ($\sim$ 4K). We were able to measure a sample temperature of 5K by using this method, although it was short lived. The temperature of the sample would often oscillate due to the alternating flowing and boiling of the liquid helium. The exhaust flowrate, and dewar pressure were normally tuned to minimize these oscillations, but in this configuration there was only dewar pressure to adjust. The amount of helium that would be needed to sustain the stabilization phase, as well as a prolonged measurement at this temperature was more than what was feasible.

The other factor in enlarging the region of zero conductance in graphene nanoconstrictions is the width of the channel. As the width is reduced, the charged islands occupy more of the carrier path, and result in a larger barrier to conduction. We had thought that by using our array of incremental widths we had exhausted the parameter space leading to width reduction. This was until we came across an article about reducing the sensitivity of the exposed PMMA film [56]. It was reported that by using the familiar developing solution of MIBK:IPA at a ratio of 1:3 but cooled to 6°C that very fine features were produced in PMMA. The reason for the increased resolution with lowered sensitivity is because of an increased selectivity between regions of relative exposure. This development method would allow for a more granular removal of fully and partially exposed areas. Due to this reduced sensitivity a new dose matrix was performed, and we determined that a dosage of 400uC/cm^2 would produce the sharpest features after this cold development.

Using this method we were able to produce graphene nanoribbons with widths down to 30nm. Figure 2.9 shows a graphene nanoribbon where the thinnest regions have been etched down to

30nm. The AFM scan shows prominent ribbon width fluctuations, but the transport is limited by the thinnest region, analogous to a quantum dot system. These ribbons held the promise of larger gapped regions to explore without pushing to lower temperatures. Unfortunately these nanoribbons were more sensitive to electro static discharge (ESD) than the thicker nanoribbons. Improper grounding in our wirebonder caused a surge of current through the device upon wirebonding, destroying this ribbon, and several more like it.

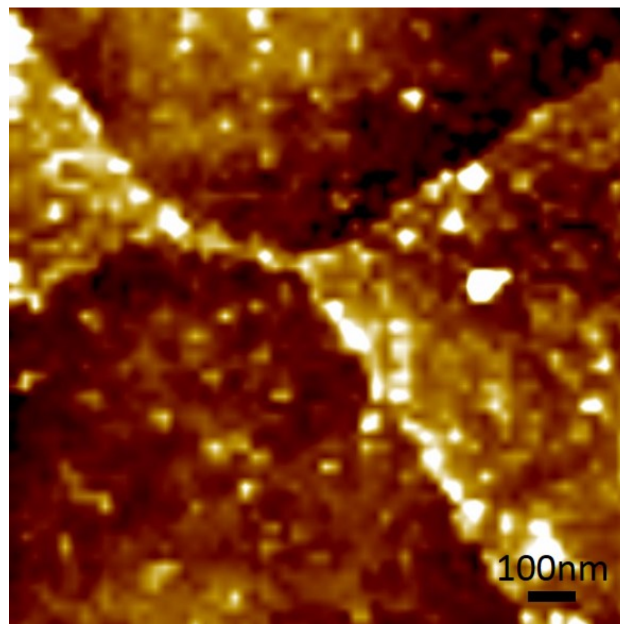

Figure 2.9: **AFM Image for a 30nm Width Graphene Nanoribbon.** An AFM image showing one of the thinnest-width graphene nanoribbons that we were able to produce using the cold development technique.

CHAPTER 3
OTHER 2D MATERIALS

3.1 Hexogonal Boron Nitride

3.1.1 Background

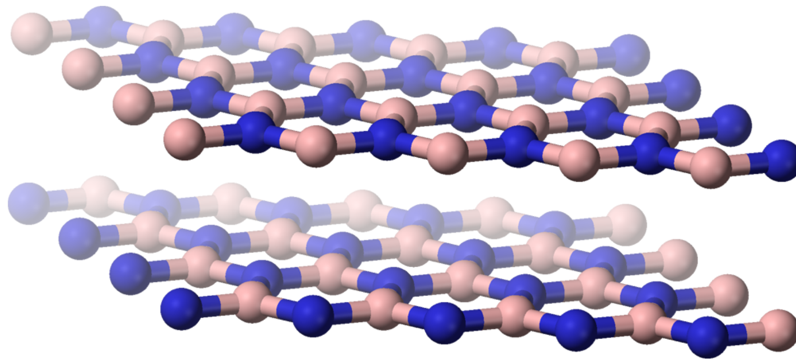

Figure 3.1: **hBN Atomic Structure.** A schematic showing the crystal structure of two single-layer hBN films. The blue spheres denote boron atoms, with nitrogen atoms denoted by tan spheres.

Other two-dimensional atomic films are anticipated to possess unique desirable properties similar to graphene. The alternating boron and nitrogen atoms in hexagonal Boron-Nitride (hBN) are arranged in an honeycomb structure similar to graphene (Figure 3.1). Due to weak van der Waals-like stacking between the layers, like graphene, this material could be exfoliated in a sim-

ilar fashion [3]. A single-layer sheet of hBN has been predicted to behave as a 4.3eV indirect gap semiconductor [57]. Some have claimed to have isolated a two-dimensional hBN film, and measured it to be highly insulating [3]. Despite this result, others have futher investigated the isolation of single hBN sheets [58]. The thinnest flake able to be produced was 3.5nm thick at the thinnest region, expected to be between 6-10 layers. The interlayer spacing for hBN has been long ago measured to be ~ 3Å [59], but it has been shown that AFM measurements of graphene and other thin films with similar interplane spacing produce an apparent thickness contrast of 0.5-1nm [10][3]. Adsorbed water and other atmospheric impurities can account for this large thickness discrepancy, and AFM measurements should be accompanied by other studies to correctly determine the number of actual hBN layers.

3.1.2 Methodology

We used a method similar to the tape exfoliation used in our early stages of graphene production. Hexogonal Boron-Nitride powder grade AC6004 purchased from Momentive Performance Materials had an average crystal size of about 10 μm. The powder was lightly dusted onto the adhesive surface of a piece of tape. Then we folded the tape so that the adhesive surfaces would make contact on either side of the boron nitride powder many times until sufficient exfoliation was met. This was determined after using the electrostatic repulsion method to place the exfoliated flakes on the surface of the desired wafer, and inspecting the surface optically. The boron nitride flakes

benefited from the same thickness oxide as the graphene, so a silicon wafer with 280nm of SiO_2 was used as the deposition target.

Figure 3.2: **Optical Image of Exfoliated hBN Flake.** Optical micrograph showing an exfoliated and bulk hBN flake. Thicker hBN crystals are yellow in color, then change from green, to blue as the number of layers decreases. The thin region used to create a device is circled in red.

Figure 3.2 shows an optical image of exfoliated hexagonal boron nitride flakes. As the thickness is reduced the perceived color of the flakes on the surface changes from gold, to yellow, green, and blue until finally reaching a very faint blue color. A catalog of candidates located optically was created, and atomic force microscopy was used to determine the apparent thickness of each film.

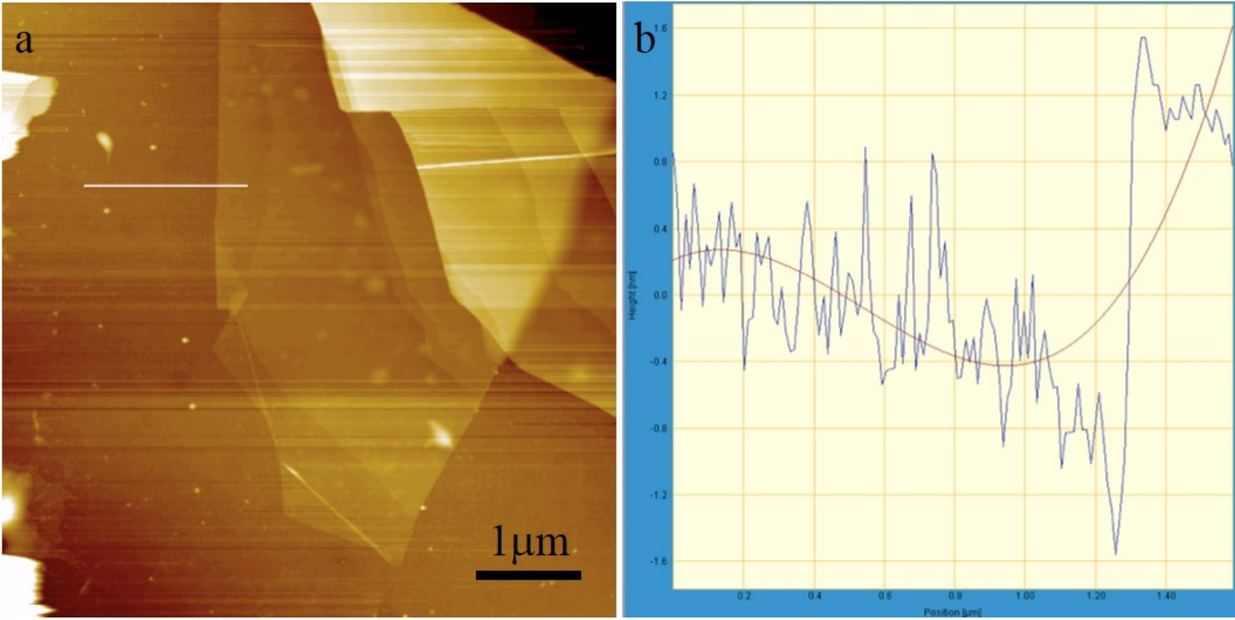

Figure 3.3: **AFM Image and Step Profile for Thin hBN.** (a) AFM scan of the thin hBN flake shown in the optical image (Figure 3.2). (b) Step profile of the line trace shown in (a).

An AFM micrograph of one of the thinnest samples isolated is shown in Figure 3.3 (a). The step height above the baseline of the SiO_2 is $\sim$ 1-1.5nm (Figure 3.3 (b)). This is a similar value to that sometimes measure for graphene. Therefore this particular hBN flake could be a single atomic layer or as thick as 3-5 layers.

As the dimensions of the target hBN areas were very small, we used electron beam lithography to write the contacts on the target HBN flake. The wafers supporting the thinnest candidates were first coated in MMA to a thickness of 600nm, and then a 400nm layer of PMMA was spincast onto the MMA undercutting layer. Then the custom electrode patterns were designed for each hBN candidate, and exposed into the resist for each wafer. After development, a metalization layer of 2nm Cr and 80nm Au was deposited with thermal evaporation. The unwanted metal was lifted off

in a heated acetone bath, leaving behind the desired electrode pattern. We then mounted the wafer and performed wirebonding before interfacing the device with the measurement system.

3.1.3 Results

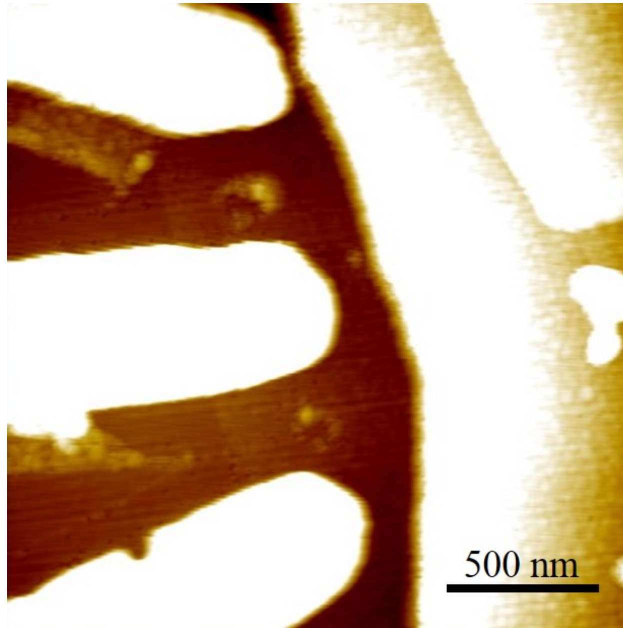

Figure 3.4: **AFM Image of Fabricated hBN Device.** AFM image showing the contacted region of the hBN flake from Figures 3.2 & 3.3. The contacts are visible as bright white regions (much taller than hBN step height), entering the image from the left side. Another contact can be seen along the right side. The hBN step can be seen between the left electrodes.

Figue 3.4 shows the same region measured by the AFM in Figure 3.3 after depositing electrodes on the $\sim 500\mu$m x 2μm region. With this electrode configuration a two-probe measurement is accommodated. This sample and others were measured, over a range of bias, and gate volt-

ages. We found these thin flakes of hBN to be largely insulating. Although this result agrees with some previous experimental studies [3], theoretical studies do predict a semiconductor-like behavior can occur [57]. It is difficult to determine the exact atomic thickness of hBN through AFM measurements alone, so further investigation may shed more light on this topic.

3.2 BSCCO

3.2.1 Background

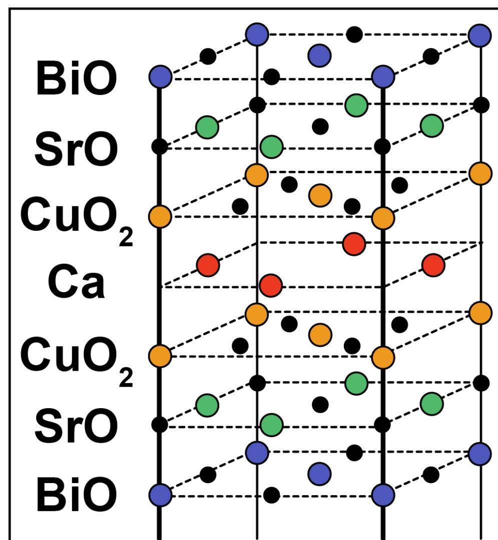

Figure 3.5: **BSCCO Atomic Structure.** A schematic showing the crystal structure of a single BSCCO layer. Oxygen atoms are shown in black, with Bi, Sr, Cu, and Ca shown in blue, green, yellow, and orange, respectively.

We studied another layered material, the high critical temperature (T_c) superconductor $Bi_2Sr_2CaCu_2O_{8+\delta}$ (BSCCO). The unit cell for BSCCO is shown in Figure 3.5. It was found previously that two-dimensional BSCCO was highly insulating [3], but we wanted to investigate where this insulating transition occurs. It was hypothesized that BSCCO would act as an anti-ferromagnetic insulator initially, but would become metallic upon O_2 annealing. It would be interesting to induce high-temperature superconductivity in a two-dimensional material, as no 2D superconductors have been isolated.

3.2.2 Methodology

To produce a single-layer of BSCCO we again used the tape method to exfoliate bulk crystal. To begin we placed the adhesive tape directly onto the single-crystal BSCCO. Peeling off the tape from the crystal we were left with a thin sheet of the material on the tape. Sandwiching the material between both halves of the tape we exfoliated the flake several times. Using the electrostatic repulsion technique we transferred the exfoliated BSCCO to a silicon wafer capped with 280nm of SiO_2. The substrates were visually inspected in the optical microscope, looking for thin flakes with flat surfaces for contacting. It was found that these BSCCO flakes would exhibit an array of different colors according to their thickness (Figure 3.6). Several thin film candidates were determined, and the location was noted for further investigation.

The AFM was used to determine the step height of these BSCCO crystals. Figure 3.6 shows a large range of thicknesses. The films shown were measured by AFM to be 220nm, 170nm, 135nm,

110nm, 80nm, and 25nm from (a)-(f), respectively. A few samples with AFM thickness as little as 14 and 6nm were isolated. The z-axis half-unit cell length of BSSCO is known to be $\sim$ 1.545nm [60][61]. This means that the smallest isolated films could be as thin as 2 full BSCCO layers.

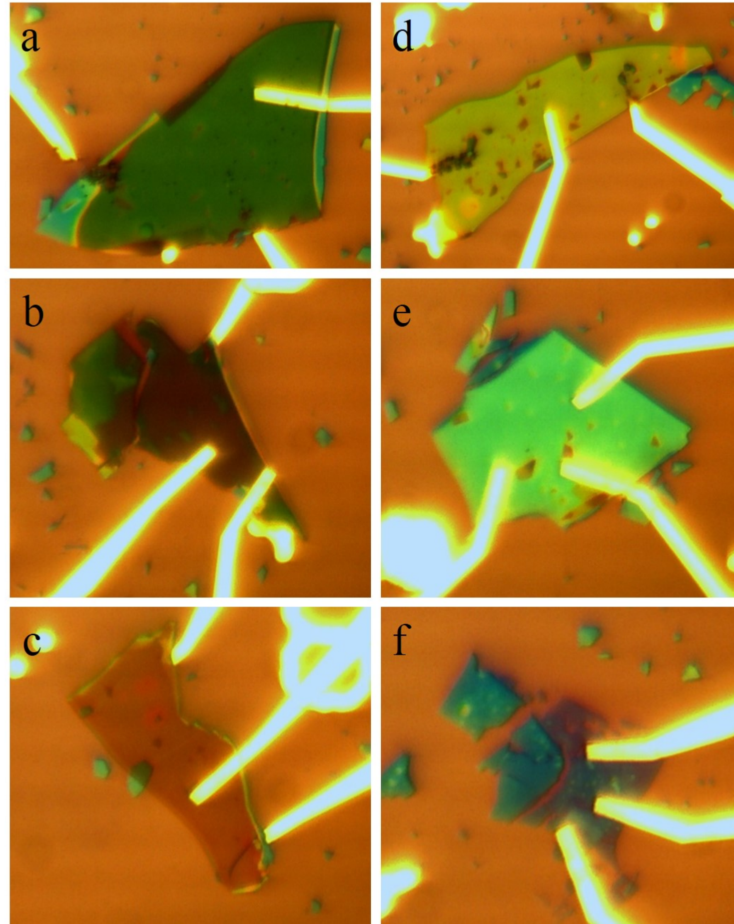

Figure 3.6: **Optical Images of BSCCO Devices of Various Thickness.** Optical images of various thickness BSCCO flakes contacted by Cr and Au electrodes. The thicknesses of the flakes are 220nm, 170nm, 135nm, 110nm, 80nm, and 25nm for (a)-(f), respectively. The devices have been annealed in O_2.

All the BSCCO devices were fabricated using e-beam lithography. Optical images were taken and imported into CAD software for device design. Once design was complete, samples were coated with 400nm MMA and 600nm PMMA at 4000RPM baking each coating at 175°C for 10 minutes. The design was then exposed into the electron beam resist using the SEM, and developed in 1:3 MIBK:IPA for 60s. Cr and Au was then thermally evaporated on the sample in high vacuum, and liftoff was performed in heated acetone. The thickness of the contacts was sufficient to cover 120% of the BSCCO film thickness. Devices were wirebonded and mounted to a package for electrical measurement.

3.2.3 Results

Figure 3.7 shows SEM and optical micrographs of one of the thinest flakes, measured with the AFM to have an apparent step height of $\sim$ 6nm. Initial testing showed that this sample, and many of the other samples were electrically insulating. Micromechanical cleavage of this material is thought to deoxygenate the film, and in order to recover conduction samples were annealed in O_2 [62]. The samples were annealed at 540°C for 2 hours and then cooled rapidly. Some electrodes were destroyed in this annealing process (Figure 3.6 (a)-(d)) but with only two electrodes a resistance measurement was able to be performed. The annealing process was successful in reducing the resistance of some of the bulk BSCCO flakes, but the thinnest flakes were never observed to become conducting.

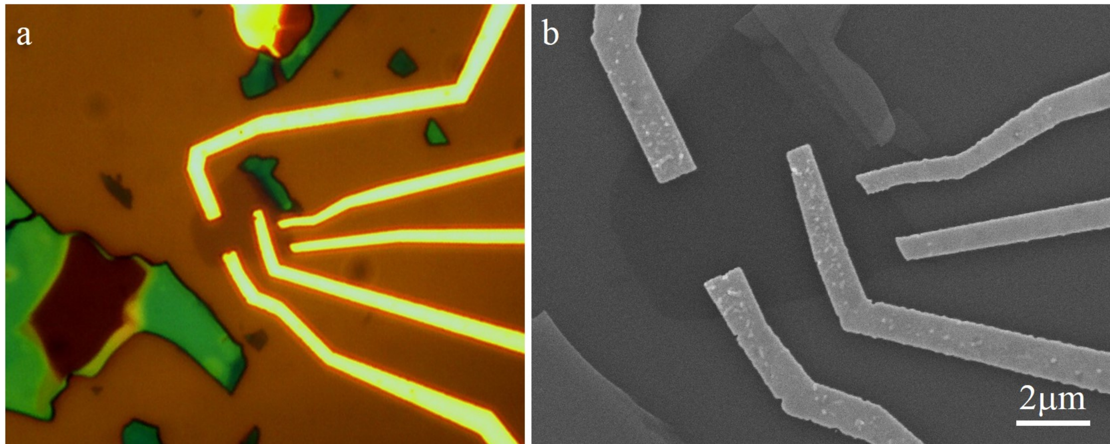

Figure 3.7: **Optical and SEM Images of Contacted Thin BSSCO Flake.** (a) Optical image of one of the thinnest isolated BSCCO flakes after electrode contact. (b) SEM image of the same device, with the two leftmost contacts on a region with 14nm step height, and the two rightmost contacts on a 6nm step height region.

Samples with step height from $\sim$ 200nm down to $\sim$ 6nm were measured, and Figure 3.8 shows the resistance value of these devices after the O_2 anneal. The samples with 20nm or less apparent step height were all found to be highly resistive (on the order of GΩ). This highly resistive behavior was observed for samples with 6nm and 14nm step heights, but a sample with 20nm step height was measured to have $\sim$ 200kΩ resistance. No larger trend was observed in the BSCCO flakes of larger thickness, samples from $\sim$ 20 - 200nm all fell within $\sim$ 200 - 600kΩ. With $\sim$ 3nm comprising the z-axis height of the full BSCCO unit cell, it appears that this transition between insulating and metallic behavior is happening between $\sim$4 and $\sim$6 BSCCO layers. Also of note is that the thinnest isolated samples seemed to all be multiples of two BSCCO layers ($\sim$6nm).

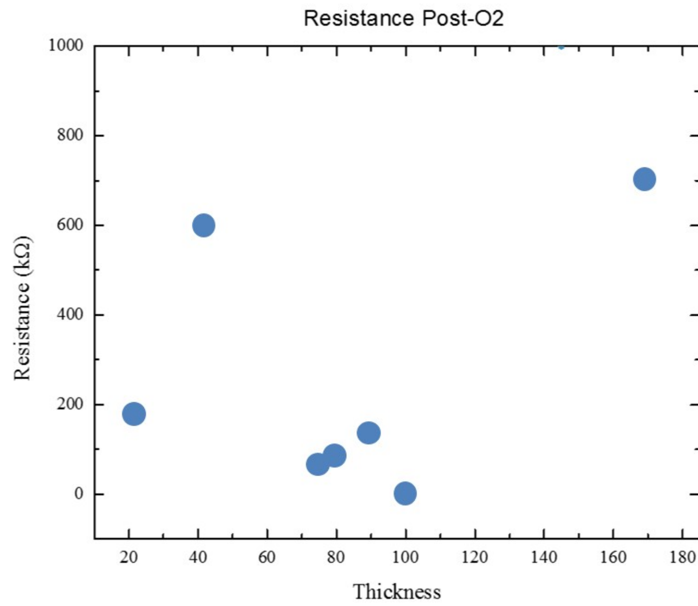

Figure 3.8: **Measured Resistance for BSSCO Films of Varying Thickness.** The measured resistance for BSSCO flakes ranging from 200nm - 20nm step heights. Very thin samples with highly resistive behavior are not shown.

CHAPTER 4
PLASMON COUPLED DEVICES

4.1 Background

To discuss plasmonics we first consider electrons in a metal. They can be described as a free electron gas of negative charges, balancing the positive ion cores and forming a plasma. Under an external electric field E with time t dependence $e^{-i\omega t}$ at an angular frequency ω, the electrons experience a polarization [63]

$$P = \frac{-ne^2}{m\omega^2}E, \tag{4.1}$$

with fundamental charge e, charge carrier concentration n, and mass m. The Drude model gives the dielectric function for a free electron gas in the high-frequency limit as [7] [63]

$$\varepsilon(\omega) = 1 + \frac{P}{\varepsilon_0 E} = 1 - \frac{\omega_p^2}{\omega^2}, \tag{4.2}$$

where we have introduced the plasma frequency ω_p. Combining Eq. 4.1 and 4.2 we can define the square of the plasma frequency as

$$\omega_p^2 = \frac{ne^2}{\varepsilon_0 m} \,. \tag{4.3}$$

The plasma frequency is the natural frequency at which an electron gas oscillates, and can be measured using scattering experiments such as electron energy loss spectroscopy (EELS). For most metals the plasma frequency has been measured to reside in the ultraviolet, between 5-15eV [63].

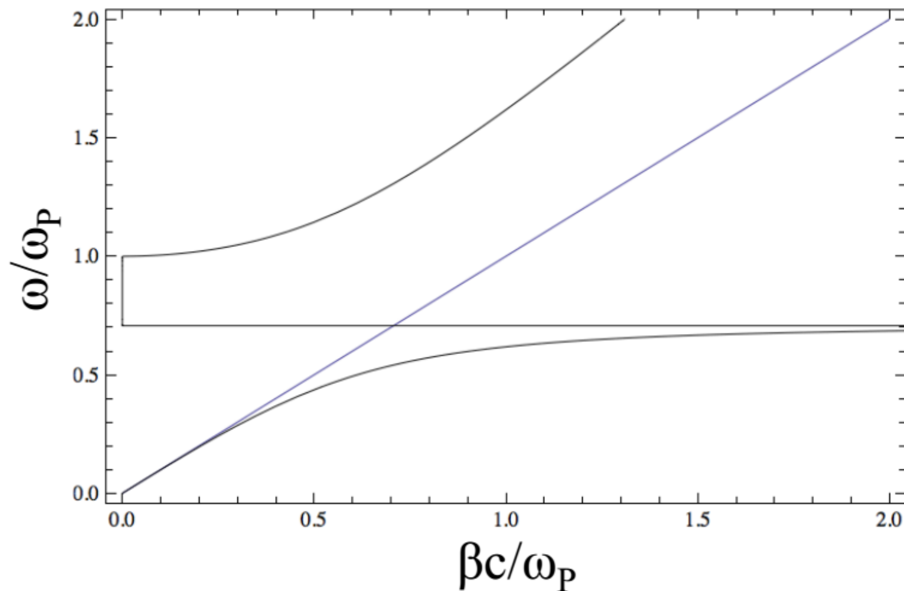

Figure 4.1: **Plasmon Dispersion for Metals.** Real part of the plasmon dispersion (black) for a metal with negligible dampening at an interface with air. The light line is also shown (blue).

Equations 4.1-4.3 are valid for frequencies close to ω_p, where damping due to electron-electron and electron-phonon scattering is negligible. But for low frequencies we need to take into account the scattering rate $\Gamma = 1/\tau$, where τ is the electron lifetime. The polarization [64] then becomes

$$P = -\frac{ne^2}{m(\omega^2 + i\Gamma\omega)} E \ , \tag{4.4}$$

and the dielectric function in the presence of dampening becomes

$$\varepsilon(\omega) = 1 - \frac{{\omega_p}^2}{\omega^2 + i\Gamma\omega} \ . \tag{4.5}$$

At frequencies above the plasmon frequency the free electron sea of a metal can sustain modes of oscillation, such as transverse optical modes, and longitudinal plasma oscillations; the quantum of which is the so-called plasmon [63].

In contrast to the volume plasmons of metals, which require particle collision for excitation, surface plasmons can be excited by coupling to transverse electromagnetic waves. Plasmonics relies on these plasma oscillations to couple with incoming photons, producing surface plasmon polaritons (SPPs). SPPs are modes of electromagnetic excitation that propagate along the boundary of two media. These SPPs can sustain electromagnetic fields well below the diffraction limit of light, by the evanescent confinement of the fields in the direction perpendicular to the interface. SPPs are only supported at the interface between a conducting medium with permittivity ε_1 and a dielectric medium with permittivity ε_2 [65]. Maxwell's equations can be solved with appropriate boundary conditions to yield the dispersion relation of SPPs propagating along the interface,

$$\beta = \frac{\omega}{c}\sqrt{\frac{\varepsilon_1 \varepsilon_2}{\varepsilon_1 + \varepsilon_2}} \ , \tag{4.6}$$

with the propagation constant β equal to the component of the wave vector in the direction of the traveling wave, where c is the speed of light in free space [64] [66]. Figure 4.1 shows the SPP dispersion for a metal-air interface in the high-frequency regime, for example, where Eq. 4.2 is sufficient to describe the dielectric function of the metal. The bound non-radiative modes of the SPPs are supported to the right of the light line, and above a normalized frequency of unity radiation into the metal occurs (transparency region).

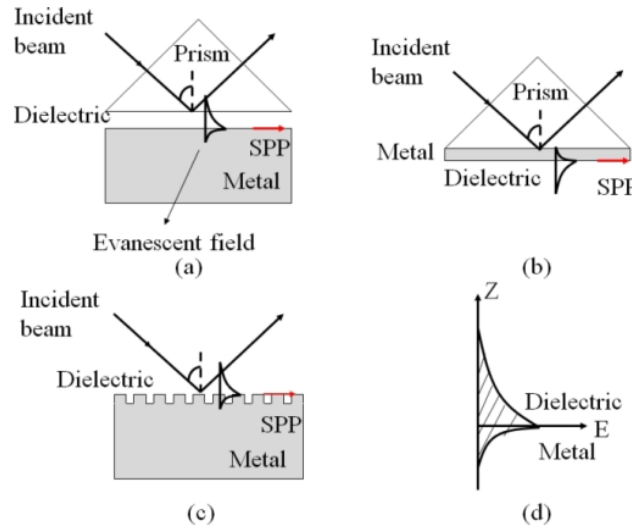

Figure 4.2: **Common SPP Coupling Techniques.** A schematic of some of the most common SPP coupling geometries [4]. The Otto configuration (a) separates the metal from the bottom of the prism with a thin dielectric layer, and the SPP wave propagates along the interior surface of the metal. The Kretschmann configuration (b) places the metal directly on the bottom prism face, and the SPP wave propagates along the exterior surface of the metal. A metal grating coupling design is shown in (c), with the SPP wave propagating along the surface exposed to radiation. The electric field profile of the SPP wave is enlarged for clarity in (d).

The propagating SPPs can be characterized by a propagation length L = 1/2Im[β], and an evanescent decay length $\zeta = [\beta^2 - \varepsilon_2(\omega/c)^2]^{-1/2}$ (corresponding to a decay of 1/e) [64]. We can also characterize the propagation efficiency of the material given the loss $\chi = Re[\beta]/Im[\beta]$, which is a measure of how many wavelengths the propagating wave can sustain before losing most of its energy. Although metals have been discussed thus far, they suffer from large losses arising partly from electronic interband transitions, especially in the visible and ultraviolet [67][68].

4.1.1 Kretschmann configuration

The excitation of surface plasmons require that the in-plane wavevector of the incident radiation matches with the SPP wavevector of the material. There are several methods that have been developed to excite these SPP modes [69][70][71] (Figure 4.2). One such method used to couple visible radiation into plasmonic oscillations in metal films is known as the Kretschmann configuration [70] (Figure 4.2 (b)). In this method, a dielectric prism has one face metalized with a skin depth (∼30-50nm) of conducting material, and light incident on the uncoated prism face is slowed as it impinges on the metal film from the inside of the prism. This slowing of incident radiation in the total internally reflecting mode allows for the momentum matching necessary for SPP excitation. Noble metals such as silver and gold are typically used as the conducting film due to low plasma frequencies. Other transition metals have bulk plasma frequencies larger than 12eV, requiring excitation in the UV [72][73][74]. Silver and gold have bulk plasma frequencies of $\sim$ 9.2 and 6.5eV, respectively, which allows excitation in the visible and nearUV range.

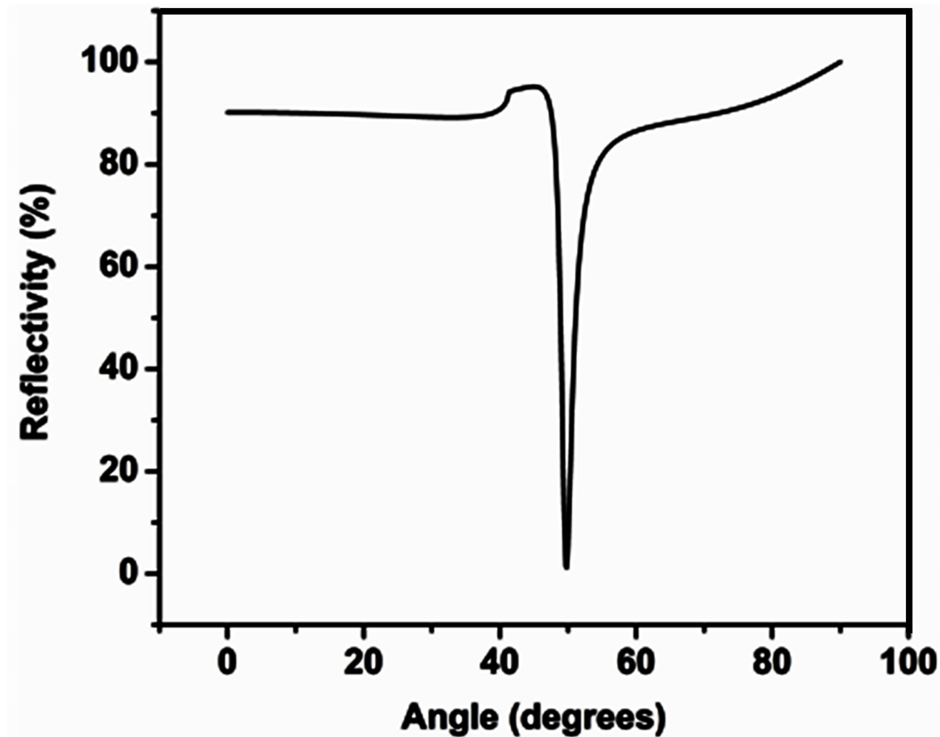

Figure 4.3: **Characteristic SPP Reflectivity Dip.** The characteristic measured reflectivity of a metal film in the Kretschmann configuration as a function of the illumination angle of incidence [5]. The characteristic absorption due to SPP excitation is observed to occur at $\sim 50^\circ$.

Figure 4.3 shows the characteristic measured reflectivity of the metal film in the Kretschmann configuration. The reflectivity of the metal film is measured as a function of the incident angle of TM-polarized radiation. The measured increase in reflected intensity at $\sim 40^\circ$ is due to total internal reflection (TIR) within the prism. The strong absorption at $\sim 50^\circ$ is due to the absorption of the incident radiation as the SPP mode is excited within the metal layer. The width and depth of this absorption are highly dependent on the dielectric permittivity of the metal and boundary layers, as well as the thickness of the metal film.

4.2 Methodology

We created a device in which the graphene FET sat atop a surface plasmon coupler, anticipating that the evanescent fields would perturb the transport properties of the FET in a measurable way. The plasmon coupler we used for the visible range was a right angle prism, coated with about a skin depth of either gold or silver in the Kretschmann configuration. At the appropriate conditions for surface plasmon excitation, the incident electromagnetic radiation is efficiently converted to a guided mode at the exposed surface of the plasmonic coupler. The electromagnetic fields produced upon surface plasmon excitation are tightly confined around the conductor surface, to within about half of the free-space wavelength. These intense electromagnetic fields are expected to modulate the Fermi energy of the graphene FET positioned nearby. Early attempts to fabricate transistor device geometry on the underside of a coated prism proved difficult. Specifically, spin-coating photoresist required a custom-machined chuck in order to secure the prism and keep the surface level throughout the spin cycle. Additionally graphene transfer, which is difficult to perform with a thin flat substrate, becomes a tedious endeavor with a large right angle prism. As an alternative to our original design, we decided that coupling a coated prism to a FET fabricated on a Si/SiO_2 wafer would be an easier task, without overtly modifying the principle of the initial design. The degree of precision necessary to center and keep the excitation region in place above an exfoliated flake was deemed implausible at best. In order to minimize any motion of the beam spot on the back face of the prism, we determined that the FET region needed to be on the order of the beam

spot or larger. To this end we grew graphene by chemical vapor deposition (CVD) in-house using a 1 quartz-glass tube-furnace.

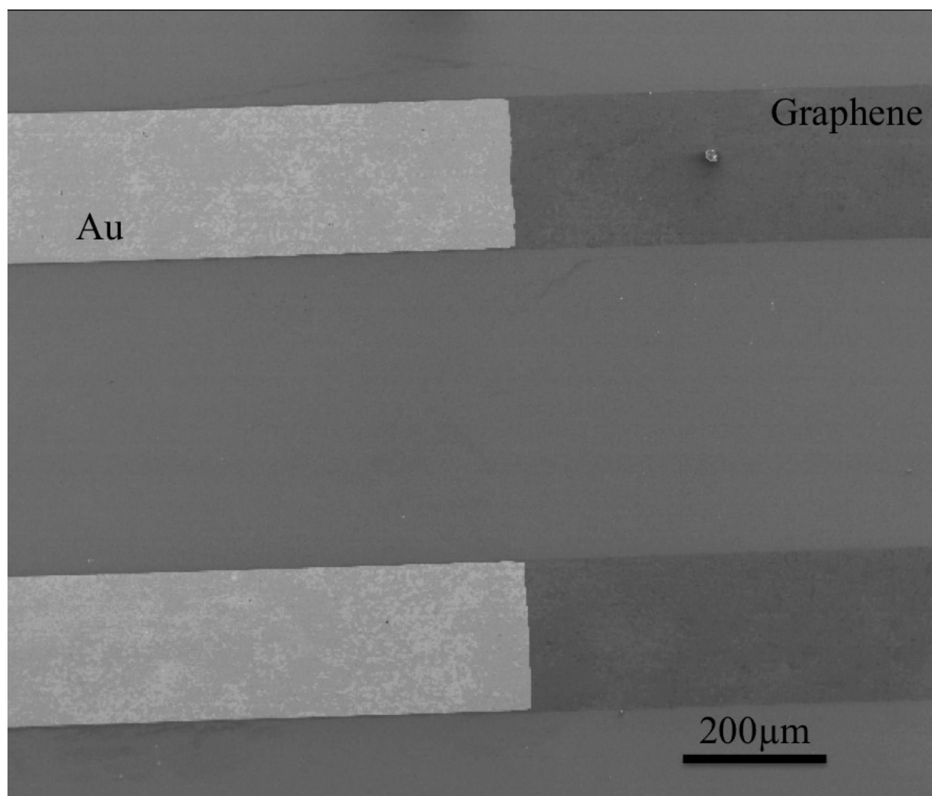

Figure 4.4: **SEM Image of Graphene Channel.** A SEM micrograph of a graphene channel array. One of the source drain electrodes is shown connected to the graphene channel.

For our FET devices we used CVD growth consisting of a predominantly single-layer continuous film. We performed the transfer using 600nm PMMA as the support layer. The backside of the Cu foil was etched for 10s in O_2 using a de-scum procedure before floating the foil in 1% APS solution. The foil was allowed to etch overnight, and the following day the PMMA supported graphene was transferred to a bath of deionized water to clean overnight. The graphene film was transferred to a new deionized water bath for the final clean, while a Si/SiO_2 wafer was etched

for 5 minutes to produce a clean hydrophilic surface. The graphene could then be fished onto the hydrophilic oxide of the target wafer. With the graphene placed correctly on the substrate, a hotplate was used to assist in the evaporation of the water using light heat. Once the sample was completely dry the hotplate was turned up to 175°C, allowing for the graphene to relax any ripples in its morphology. After heating at this temperature for 30 minutes the heat was reduced, and the sample cooled to room-temperature. Finally the PMMA was stripped in acetone, and the sample was ready for additional processing.

Photolithography can be used to fabricate these millimeter-sized FET devices. Photo-sensitive resists work similarly to the E-beam resists, with photoactive compounds (PAC)s being activated by photons of sufficient energy, rather than electrons. Photolithography is typically performed by shining ultraviolet (UV) light from a mercury lamp through a metalized quartz mask that allows light to pass only through regions with no metal. This process is much faster to perform than electron beam lithography, but does not benefit from the customizability of device geometry afforded by electron beam lithography. Additionally, the lower limit on feature size is dependent on the diffraction limit of the light source, around 2μm for the mercury I-line, and 32nm for deep ultraviolet (DUV) lithography. As our facilities did not have DUV lithography capabilities, e-beam was used where accuracy below 2μm was needed.

The graphene transferred to Si/SiO_2 wafers was coated in 1.3μm of Shipley 1800 series photoresist. The photoresist was exposed in an array of rectangles to form contact pads. These exposed regions were removed in RD6 developer, and then the sample was rinsed in DI water. An 80nm Au layer with a 2nm Cr sticking layer were deposited onto the surface of the sample by thermal

evaporation in high vacuum. The gold film had a discontinuity at the boundary between remaining polymer and developed regions, and when the film was stripped in acetone only the regions free of polymer remained. The rectangles formed devices once the graphene was patterned to match. Similarly, the graphene was again spin cast with photoresist, and the photo mask was aligned to the existing contacts. The second mask does not allow the UV to affect the graphene channel between each contact pair, but does allow the rest of the surface to be exposed. This results in a protective polymer layer connecting each pair of contacts in order to selectively etch the unwanted graphene. The sample was subjected to plasma cleaning for 10 seconds using 50W RF power in 5sccm O_2 atmosphere, removing the exposed graphene, but not etching completely through the polymer. Finally the protective polymer was removed in acetone, and the sample was ready for measurement. The contact region of the completed graphene channel devices is shown in the SEM micrograph of Figure 4.4.

Initial attempts to mount the prism onto a seperate wafer with a FET were aided by the use of a 60nm buffer polymer layer. This layer of PMMA that was spin cast onto the completed FET was implemented to protect the graphene film from scraping against the underside of the prism during the mounting process. In order to mount the prism to the FET the prism was placed with conducting film facing upwards. A drop of isopropyl alcohol (IPA) was deposited on the metal coated prism surface, and the wafer was brought into contact with the FET facing the prism. The IPA was used to allow for final adjustments to be made after contact between the wafer and prism was established. After positioning the wafer and prism in the correct orientation, a 40g weight was placed on top of the wafer, and the IPA was allowed to dry. Then a small drop of cyanoacrylate on

each of the prism corners was used to secure the prism to the Si/SiO_2 wafer. The prism coupler was then secured atop the FET device, completing the detector device. Finally, the wafer was glued to a chip package, and a wedge bonder was then used to bond a thin wire between the contact pads of the FET and the package. The completed device was mounted in a complimentary chip socket secured to an optical post.

4.3 Experimental Setup

The optical post atop of which the completed device was secured, was placed at the center of rotation of a motor controlled goniometer. The goniometer is a device that allows for precise adjustment and monitoring of the incident angle. A laser diode was mounted at a fixed position while the sample and detector are rotated in relation to the incident beam. The gear ratio between the sample stage and detector arm can set the detector rotation to be twice that of the sample rotation, allowing for the ordinary reflection to be tracked by the detector. The angle of incidence is used in order to achieve momentum matching between the incident photons and the guided mode in the conductor. When the condition for the excitation of this surface plasmon mode is met, the reflectance of the film drops close to zero as the energy is efficiently transferred to this guided mode, and eventually dissipates in the film due to ohmic losses. Thus sweeping the angle of incidence and monitoring reflection, there is a prominent drop in reflectance at the angle corresponding to SPP generation. A laser diode operating at 651nm, with TM polarization, was used initially as the excitation source. The laser diode was rotate-able in order to measure the response to TE-polarization. We created

a custom LabVIEW program to record the position of the goniometer, while also capturing the voltage of the detector and the transport properties of interest in the graphene channel. Figure 4.5 (a) shows the optical setup used to measure the reflectance of the metal film.

Preliminary experiments to check the effects of the local field due to SPPs were simple. We established a steady source-drain current across the graphene with a fixed source drain bias and zero applied gate bias. We then monitored the change in current produced by the excitation of nearby surface plasmons. There was no measurable change in the DC current through the channel. The graphene retained the same resistance throughout the angular sweep, and longtime exposures to the fields of nearby SPPs produced no measurable change in the graphene FET. Changing the gate voltage and performing the same experimentation produced no new results. In order to achieve higher signal-to-noise we used a custom made circuit and function generator to digitally chop the laser diode. The detector signal and graphene signal were both demodulated using lock-in amplifiers triggered to the chopping frequency. Surprisingly, the lock-in output did show some change around the SPP excitation angle, but it was troubling that the magnitude of this effect seemed to be frequency dependent. Looking at the signal from the device in the oscilloscope cleared up the initial confusion, but introduced many more questions. Rather than observing a steady change that spanned the length of the optical excitation, we observed a transient response that had a decay length of about 30μs. The relationship between the transient response time and the chopping frequency effected the measured DC level. As the frequency was decreased, the transient occupied only a small segment of each sampling window, and the apparent magnitude of the signal was lessened.

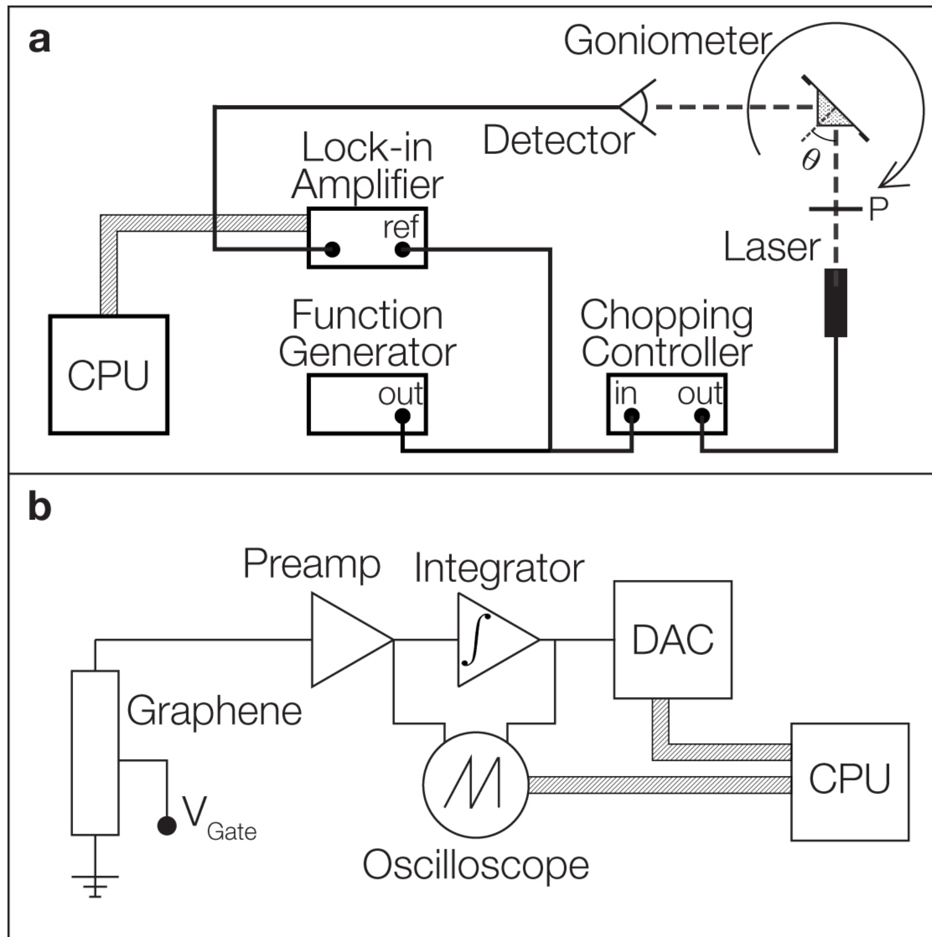

Figure 4.5: **Experimental Measurement and Electronic Setup.** (a) A schematic of the experimental measurement setup showing the optical path of the laser. A laser diode is fixed in front of a polarizer (P) as the sample is rotated by the goniometer and the reflected intensity is measured by the detector. A pulsed signal is demodulated by the lock-in amplifier. (b) The graphene channel closed circuit current is measured using an integrator after amplification, and the signal is recorded using a DAC board.

In order to obtain a DC level from this transient response, a gated boxcar averager was used. The electronic experimental setup is shown in Figure 4.5 (b). By placing the gate of the boxcar

averager only around the transient pulse we were able to approximate the intensity, and the average of this region was recorded. Immediately it became clear that the average of this transient had a maximum at the angle corresponding to surface plasmon excitation. The lingering question about this observation was the reason for a transient response, and the damping rate of 30μs was not a native quantity for graphene.

The first wave of devices suffered from a relatively broad and weak SPP feature, as compared to the measured prism before mounting to the FET. We tuned the thickness of the gold film between 30nm and 60nm, eventually settling on using a 45nm thick conducting layer to produce the sharpest and deepest resonant feature. Although a troubling occurrence was that as we fabricated more devices the unmounted coated prisms showed improvement in the resonant feature, while the mounted prism devices began to show no resonance at all. It took many diagnostic tests to determine what had changed between our initial devices that exhibited strong plasmonic resonance, and the later devices that had no plasmonic resonance at all. It turned out that the first few mounted devices that produced positive results had an unintentional air gap that formed between the conducting prism surface and the buffer polymer layer on top of the FET. This inefficiency in mounting the two surfaces together was actually crucial in preserving the conditions necessary for surface plasmon excitation. In order for the incident radiation to be converted to the guided mode at the surface of the conductor, there must be sufficient dielectric contrast between the bounding materials of the conducing film. The BK-7 glass prism is necessary for the momentum matching, and has a mostly real dielectric permittivity of $\varepsilon \sim 2.29$ at a wavelength of 632nm. The 50nm PMMA buffer layer on the opposite side of the conducting film has a dielectric permittivity $\varepsilon \sim 2.29$, fol-

lowed by the negligibly thick graphene layer, and finally an amorphous SiO_2 layer with dielectric permittivity $\varepsilon \sim 2.12$. Thus a perfect interface with no air gap between the prism and FET does not provide sufficient dielectric contrast. We began incorporating this air gap into the fabrication of the devices, by using a shadow mask technique to deposit 500nm of electron beam evaporated SiO_2. This insulating standoff allowed for gapless interfacing at the sides of the prism, while preserving the conditions necessary for SPP generation in the center of the prism over top the graphene FET.

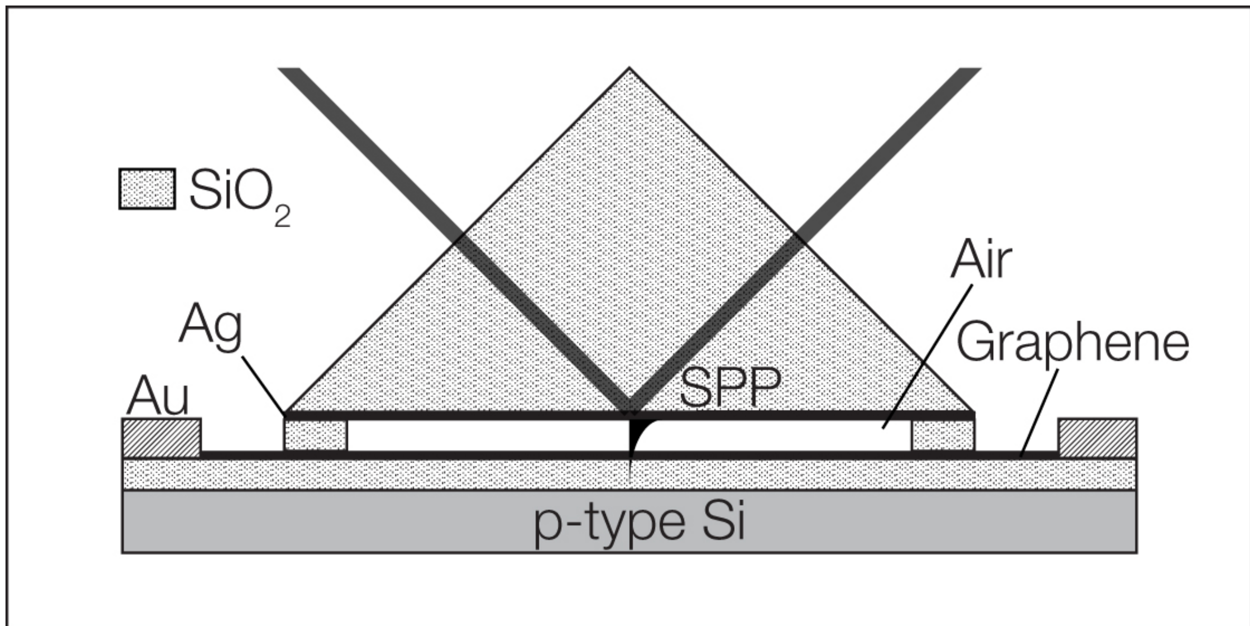

Figure 4.6: **SPP Coupled FET Device Schematic.** A schematic of the SPP coupled FET device geometry. A graphene FET is situated below a right angle prism coupler. The bottom face of the prism is coated in silver, and an air gap between the coupler and FET allow for SPP excitation in the silver film.

The second generation of devices all succeeded in exhibiting surface plasmon excitation. Figure 4.6 shows the schematic of the final device design, incorporating an air gap between the

graphene FET and SPP coupler. The transient phenomenon was stronger than ever, owing to the increased plasmonic absorption. In order to confirm the nature of this transient current, the polarization of the laser diode was changed, and the response to TE polarized illumination was studied over the range of incidence angles. Under the same conditions necessary for plasmon excitation, but without the correct polarization for this excitation, the transient signal ceased to exist. With this check completed, the effect appeared as if it could be attributed to an interaction with the SPP fields. We demonstrated that the wavelength selectivity afforded by the Kretschmann configuration translated to an optical sensor that was also wavelength selective, with observations of sensitivity at 445nm, 532nm, and 651nm wavelengths. The need for a separate detecting circuit could be alleviated by this type of device. The problem was that there was still no good explanation for the transient nature of the response, or the time frame over which it was observed. Furthermore the size of the air gap was expected to have a significant role in the response of the graphene channel, as the evanescent SPP fields fully decay over roughly half the freespace wavelength away from the conducting surface. Devices fabricated with 500nm air gaps did not have a lower response from those with 400nm air gaps.

4.4 Results

In Figure 4.7 we present the time dependent response of the graphene channel for both TM and TE polarization at the angle of incidence corresponding to SPP excitation. For TM polarization, as the laser is pulsed the current grows from near 0nA to $\sim$200nA, falling again to zero with a decay

time of $\sim 30\mu s$. As the laser excitation is removed a negative current less than half the magnitude is observed with a similar decay time. When SPPs are no longer excited upon illumination (TE polarization) there is no transient current observed in the graphene channel (Figure 4.7, dotted line).

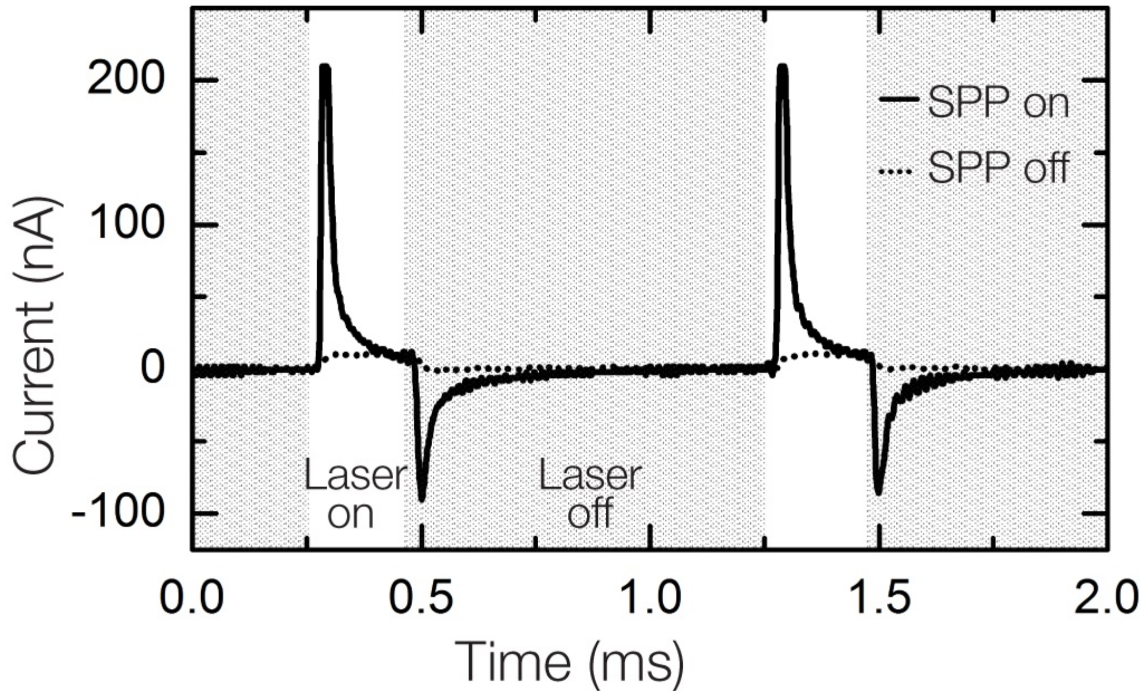

Figure 4.7: **Graphene Channel Transient Response.** Measured transient current through the graphene channel. The response is shown for about two laser cycles. Shown are the channel response for the conditions required for SPP excitation under TM (SPP on, solid) and TE (SPP off, dotted) polarizations.

The photodetector and graphene channel response to 651nm laser excitation at varying angles of incidence is shown in Figure 4.8. The reflectivity of the prism, measured at the detector, is

shown in black, and exhibits the characteristic dip due to plasmonic excitation. The integrated graphene channel response to both TM (blue) and TE (red) is shown. Etalon formation between the SPP propagation layer and the different layers of the device (Figure 4.6) is responsible for the oscillations spanning 35° - 39° angle of incidence. In the graphene channel response both polarizations produce features below the TIR angle.

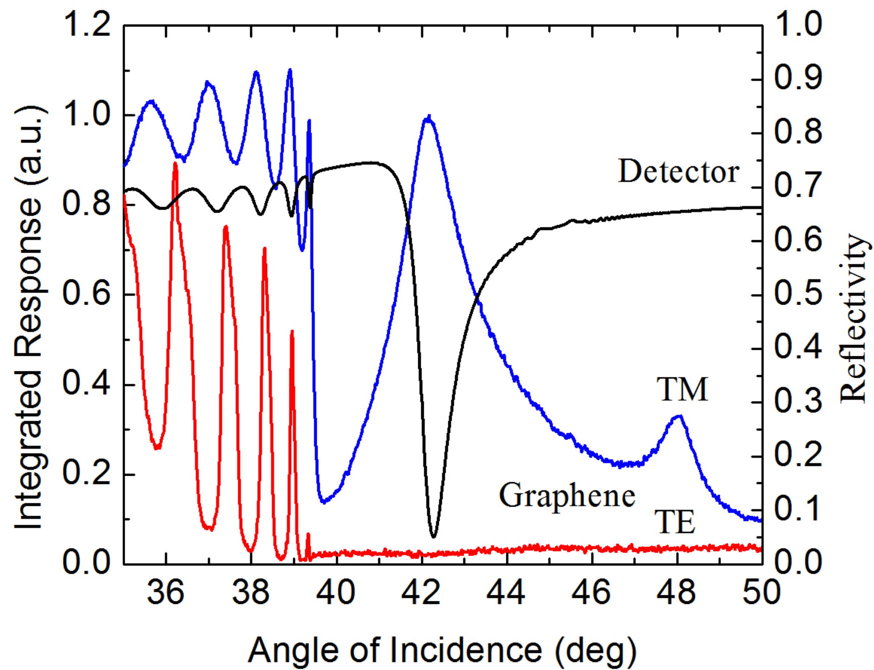

Figure 4.8: **Graphene Channel Response to Different Polarizations.** Averaged transient graphene channel response over a range of incidence angles. The graphene channel response to both TM-polarized (blue) and TE-polarized (red) incident radiation are shown. The reflectivity of the metal film was simultaneously captured, and is shown in black.

Once total internal reflection is achieved slightly past 39° the signal from the graphene drops precipitously, as the substrate is no longer exposed directly to direct laser illumination. For 651nm excitation the absorption due to SPP excitation causes a sharp decrease in the reflected intensity measured at the photodetector at approximately 42.27° angle of incidence. At the angle for SPP excitation the graphene channel exposed to TM radiation experiences an enhancement of the transient current, but the TE polarized radiation shows no such enhancement. As only TM polarized radiation is capable of exciting surface plasmons, this effect can be linked to SPP excitation. The graphene peak, while broader than that of the detector, occurs at a slightly shallower angle. A Gaussian fit to the SPP peaks confirms that the graphene response is centered 0.2° shorter than the detector peak, arising at 42.15° angle of incidence. The FWHM of the graphene response is 1.56°, while that of the detector is 0.60°. Additionally, a shoulder at $\sim 48°$ is visible in the graphene channel response. These results are consistent regardless if the SPP propagation layer is Ag or Au.

The graphene FET structure allows for modulation of the observed effect. By applying an external voltage to the back gate, we are able to drastically amplify or reduce the magnitude of the effect. As little as +1V applied to the gate electrode resulted in a reduction of the channel voltage in resonance by 97.1%, while applying -1V to the back gate is sufficient to amplify this voltage drastically (Figure 4.9). This effect contradicts the ambipoloar gating characteristic of graphene, and hints at the mechanism for transient enhancement at the SPP condition.

The frequency selectivity of the SPP excitation translates to the measured response. Figure 4.10 shows the wavelength dependent graphene channel response for a wide range of angles of

incidence. TM polarized source excitation wavelengths of 651nm, 532nm, and 445nm were used to excite SPPs in the plasmon coupler.

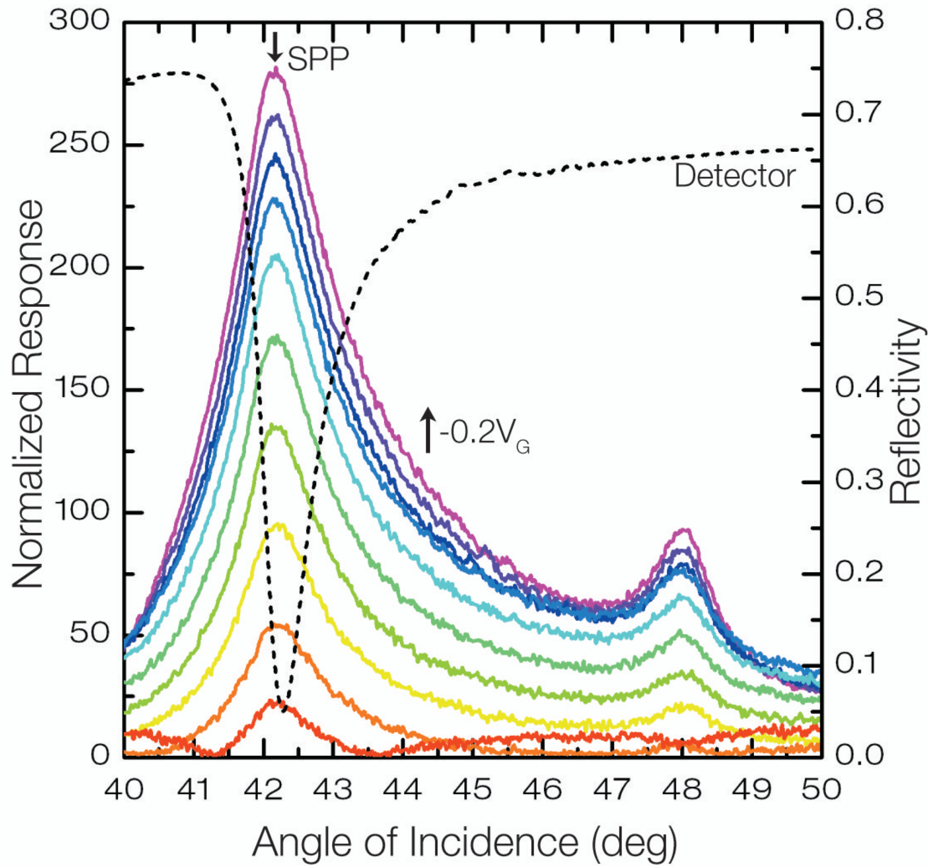

Figure 4.9: **Channel Response to Gating.** Measured transient current through the graphene channel for different levels of applied gate bias, upon SPP excitation at 651nm. Each curve is separated by 0.2V of gate voltage from the bottom to the top (+.4V to -1.4V, respectively).

For 445nm excitation the peak is relativity broad, occurring at $\sim 47.3^\circ$. The graphene channel response for 445nm excitation wavelength shows the poorest signal-to-noise, as well as the lowest rise in signal as compared to the background at 40° or 50°. A 532nm wavelength laser excitation

produces a SPP peak centered at 43.62° in the detector response, and a peak in the graphene channel voltage at 43.27°. The $\sim 1°+$ difference in SPP feature centers is sufficient to differentiate the source excitation wavelengths.

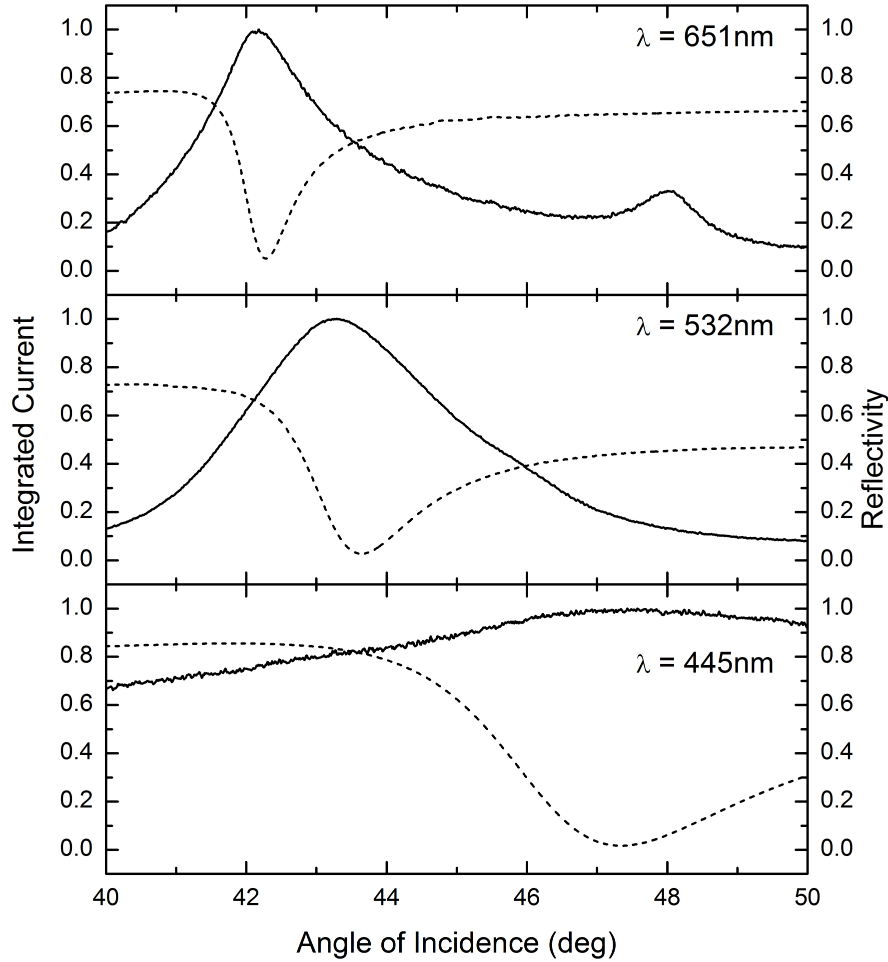

Figure 4.10: **Channel Response to Different Wavelengths.** Measured transient current through the graphene channel for different excitation wavelengths.

Once again the graphene maximum occurs at a slightly shorter angle, as compared to the reflectivity minimum of the detector. The time dependent response of the graphene channel for both the 445nm and 532nm SPP excitation is consistent with the results as discussed previously. The ATR coupler used not only contributes frequency sensitivity to the graphene response, but should also donate the surface sensitivity of the SPP fields utilized in surface plasmon resonance (SPR) spectrometers.

4.5 Discussion

The mechanism for this excitation became clear after analyzing the observed graphene channel response. The first indication came from the fact that the air gap size did not produce the strong effect expected from a highly confined field in the gap region. Although the 500nm gap seemed to place the graphene outside the region of influence of the SPP fields, the effect was ever-present. Testing the FET devices before mounting the prism coupler, we noticed that there still existed a transient current upon illumination. Initial concerns were that the polymer layer may be responsible, but upon removal of this layer the effect persisted. Nothing seemed to effect this transient current at all, and more troubling it was measurable with the laser excitation spot positioned to the side of the graphene channel. The conclusive diagnostic measure was unexpected, and dependent upon using a new type of silicon wafer as the substrate. The lightly doped wafers used in the first two generations of devices exhibited the transient current, while the new heavily doped silicon wafers had no effect whatsoever. We determined that the lightly doped silicon wafers played an important role in the observed response. The carrier lifetime in lightly doped silicon is larger than that in

heavily doped silicon [75]. This realization coupled with the observation that at angles lower than the TIR angle there was a similar transient current observed in the graphene channel alluded to the fact that transmitted radiation was reaching the silicon substrate.

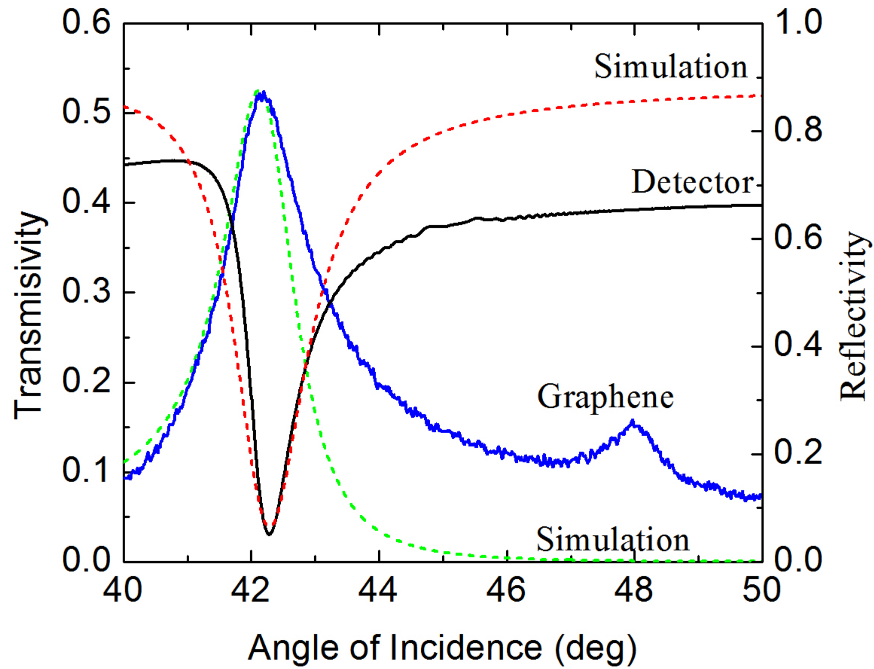

Figure 4.11: **Reflectance and Transmittance Simulation.** Calculated reflectance and transmittance through the multilayer stack. Measured reflectance, and graphene channel response normalized to the peak calculated transmittance.

To test this we must study the anticipated transmission through this multilayer stack. The reflection and transmission through a multilayer stack can be calculated using the transfer matrix method, described in [76]. Figure 4.11 shows the measured data for 651nm excitation, along with the calculated transmission and reflection through a glass-Ag-air-glass stack, with Ag and air

thicknesses of 42nm and 680nm, respectively. The calculated reflectance is in good agreement with that measured by the detector, although the reflection outside of the SPP angle is expected to be much higher. This can be due to the particulars of the deposited metal film measured in the experiment. The calculated transmission shows that up to 50% of the incident radiation is expected to transmit through the stack at angles larger than the TIR angle. The measured graphene data is plotted, with the peak of the measured signal normalized to the maximum transmission. The shape of the calculated transmission peak at the SPP angle is strikingly similar to the shape of the measured graphene response. Again the experimental data deviates from the simulation at angles larger than the SPP angle, but this can be due to imperfections in the device.

Thus, the observed effect was due to photoexcitation in the underlying silicon substrate. Photoexcited electrons and holes are formed in the silicon as a result of the incident radiation. These charge carriers are then separated due to energy band bending at the silicon SiO_2 interface [75]. For our P-type silicon the photo-generated electrons diffuse towards this interface, while the holes are repelled. The effect is a charge buildup at the interface, which in turn, creates a charging current in the graphene channel due to the natural capacitor created between the silicon, SiO_2, and graphene. The application of gate voltage results in the enhancement or depletion of the region of band bending near the interface, allowing or preventing electrons from diffusing towards this boundary.

Regardless of the actual mechanism for the observed response it remains that the device performs excellently as an on-chip spectral photosensor. This device design alleviates the need for external sensing elements, and can directly and clandestinely act as an optical detector in a com-

pact package. Additionally, this technology can be easily adapted throughout the electromagnetic spectrum by simply selecting the appropriate plasmonic coupling element.

4.5.1 Second Generation Coupled Devices

Lastly, we tested the effect of AC gating on graphene by placing the graphene film closer to the conducting film. A third generation of graphene FET coupled plasmonic detector eliminated the need for an air gap entirely, and placed the graphene film only 50nm apart from the intense SPP fields. To eliminate the hurdle of fabricating the graphene FET directly on top of the prism face, an index matching gel was used to join the prism face with a standard glass microscope slide atop which the FET could be fabricated with ease. As before, a skin depth of 45nm of silver was evaporated on the microscope slide, acting as the conductor in which the surface plasmons were to be excited. The fact that the conducting material and the graphene film needed to be electrically isolated did not change. This isolation layer prompted a trade off between a very thin dielectric to preserve the intense plasmonic fields, and a layer thick enough to prevent dielectric breakdown. Simulations we performed of the SPP damping imparted by a thin layer of SiO_2 on top of the silver showed that SiO_2 any thicker than 50nm would result in less than 60% conversion of the incident radiation. Thus this metal was capped with 50nm of oxide, after which the center was shadow masked in order to cover the sidewalls of the conducting film with an additional 60nm of oxide to prevent shorting to the silver. Then graphene was transferred to the oxide, and contacts to the graphene and silver were made with conducting epoxy. The contacts were made in this way to

limit additional processing that contacts defined by photolithograpy would entail. Then the index matching gel was used to form an optically unintrusive marrying of the prism and uncoated side of the slide. The incident radiation passes through the bottom face of the prism into the slide, and reflects off the back surface of the metal film.

In this new device geometry the graphene film is placed at the most intense region of the SPP fields. This device was tested by applying an external bias voltage, and measuring the effect of the SPP fields on the graphene channel resistance. Even when placed in a much more intense region of the SPP fields, the AC gating provided by the plasmon mode did not affect the graphene channel resistance in any significant way. In addition, the transient response observed in the previous generation of devices was absent, as expected from removal of the silicon substrate. Theoretically the strength of the fields generated upon surface plasmon excitation should be more than sufficient in gating the graphene film. We believe the problem arises from the intrinsic doping level of the graphene film upon transfer. Transferred graphene films are almost exclusively P-type doped, as reported by others [77]. For most applications this does not pose a significant problem. Although when the oscillation frequency of the SPP fields is in the terahertz, a net effect must be observed, as sampling at a sufficient rate is not yet possible. Thus the only way in which a net change in resistance would be observable from gating at this rate would be for graphene with Fermi energy corresponding to the charge neutrality point. For graphene that is doped sufficiently to have a majority carrier, the result of positive and negative external electric fields becomes equal and opposite, with the net effect vanishing. But for graphene that has the lowest possible charge density, an alternating electric field would increase channel conductivity regardless of the sign of the field.

While it is possible to move the Fermi energy in this geometry by applying external bias to the silver layer, the thin oxide limits the range of voltages which can be safely applied. We tested the dielectric breakdown strength of the SiO_2 films able to be deposited with our equipment, and found that for a 50nm layer breakdown occurs between only 5-10V of external bias. Separately it was determined that on average to shift our transferred graphene films to the charge neutral point an external voltage of 30-100V applied to the back gate was required over 280nm of oxide. The corresponding voltage needed to achieve the same effect with only 50nm of oxide would be 5-10V. An alternative doping method is to use an electrolytic gel on the exposed surface of graphene, which is able to shift the Fermi energy of the film substantially. This is not possible in our device due to the necessity that the material on the upper boundary of the graphene film possess a sufficiently low dielectric constant for SPP generation.

4.6 Grating Devices

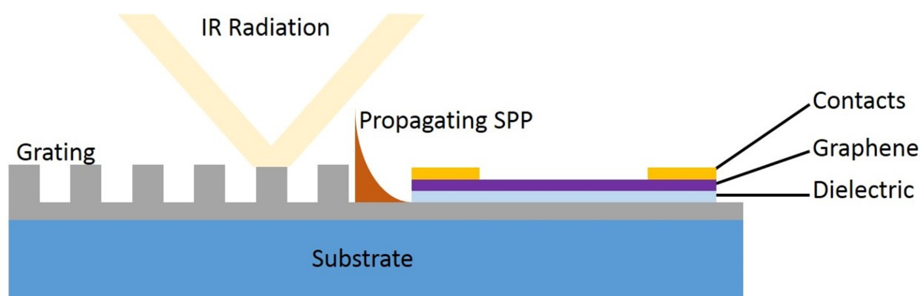

Figure 4.12: **SPP Coupled Graphene FET Grating Schematic.** A schematic for grating–graphene FET coupling geometry for infrared measurements.

In an attempt to further the impact of these devices, an effort was made to bring this sensing technology to new spectral regions, specifically the infrared (IR). In order to move the active spectral range of our coupled transistor device into the IR, the prism coupler would need to be replaced by a coupler more suited to longer wavelengths. Two possible routes exist, one in which the material of the prism is changed from glass to an IR transparent material such as Si or Ge. The other method would be to change the coupler entirely to a grating made of metal. It has been determined previously that a grating structure is preferred over a right angle or hemispherical prism for plasmon excitation in the IR [78]. To excite surface plasmons in a grating its charge carriers must be able to travel transverse to the grating grooves. A metal layer spanning the bottom of the trenches must be deposited in addition to the metal rulings. It has also been demonstrated that the greatest SPP fields are obtained for a grating with groove depth of $\sim 1\mu$m [79]. The period can be set close to the source wavelength, with higher order harmonics observable as the period becomes larger. Thus a new device geometry would need to be devised in order to incorporate a grating coupler in the place of the old prism coupler. Ideally, a similar geometry to the previous devices could be fabricated. It is easy to envision depositing a thin oxide atop the grating structure, and then simply transferring the graphene on top of this stack. Unfortunately the tensile strength of graphene is limited by the polycrystalline nature of the CVD film, and the tilted grain boundaries have ruptured for much shorter suspensions [80]. Instead, using the cm long propegation length of SPPs on metal in this spectral range, the graphene FET can be fabricated nearby the edge of the grating structure. In this way the graphene transistor can be fabricated using conventional methods. A thin dielectric layer is used to isolate the graphene film from the silver surface upon which the surface plasmons

are propagating. Then a channel and contacts can be fabricated using photolithography. Incident radiation is directed toward the edge of the grating structure, and the SPPs propegate beneath the FET in the silver gate layer. The transistor is subject to the concentrated AC fields produced by the surface plasmons. A cross-sectional schematic for the coupling of infrared SPPs, and a graphene FET is shown in Figure 4.12.

4.6.1 Methodology

Gratings of various periods and heights were fabricated using photolithography. We tested several methods of grating fabrication including liftoff and etching. Etching is a subtractive process, and positive resist should be used to get as close as possible to the correct duty cycle. In the etching process metal was first evaporated onto a target substrate as thick as the desired groove height. Then resist was spincast onto the metalized wafer at the thickness appropriate for the particular type of etching. The resist was then exposed to UV radiation through a photomask with the desired grating pattern. The resist was developed, and then the exposed metal was subjected to etching. A selective etching, such as chemical etchant, does not attack the protective polymer, but does etch the sidewall as the trench is created. An anisotropic plasma etch will result in sharper sidewalls, but the protective resist must be thick enough to survive the etching process. The protective polymer can then be stripped in solvent, and then the wafer is left with the metalized grating rulings. In order to provide a conducting layer across the trenches, the wafer was then metalized with 100nm of additional metal. This thin layer should not change the grating profile substantially, but a thicker

layer of capping metal may result in a more sinusoidal profile. The liftoff method can be performed either with a bare wafer and final capping layer, or a basal conducting layer. To achieve a complete liftoff it is important to have a negative sidewall profile for the developed resist. We tried both a negative tone resists, as well as resists of different sensitivity stacked one atop the other to achieve what is known as an undercut. Metal was then evaporated over the entire wafer, making contact with the base substrate in the developed regions. When the photoresist has a negatively sloping sidewall and is thicker than the deposited metal, the overhang creates a small shadow-masked region to separate the metal from the resist. This allows the resist to separate cleanly from the surface, without pulling the desired metal with it. Having a precise sidewall profile is very important for fabricating gratings using metal liftoff. Without these precautions the entire metal film is liable to lift off the surface rather than just the unwanted metal. We found several methods worked, but had the most luck achieving the desired duty cycle with a bare wafer coated in photoresist stacked atop an undercutting layer, performing metallization followed by liftoff, and then finally capping with another metallization layer.

4.6.2 Results

A pulsed tunable quantum cascade laser (QCL) was employed to test these new devices in the IR. The QCL had a tunable range from 7.9 - 10.5μm, and was pulsed at 100kHz. The excitation spot was placed at the edge of the grating region with the graphene FET along the optical path, such that the propagating mode would affect the graphene. As with the previous tests we first checked

the graphene for a change in resistance when exposed to the SPP fields. This was performed by applying an external bias to the graphene film, and measuring the change in current through the graphene. The excitation of surface plasmons nearby had no measurable effect on the graphene. Looking at the time dependent response there was no perceivable change in the graphene during the on pulse of the beam. The transient response due to charging was predictably absent from this device design. This result mimics the measurements performed on the graphene coupled prism device that used the glass slide substrate. Again we believe the doping concentration of the graphene film to be the main hurdle in observing an effect due to the AC gating.

CHAPTER 5
SPP FACILITATED DIFFRACTION INTO PROHIBITED ORDERS

5.1 Backround

In working with gratings and surface plasmon polariton excitations in the infrared we learned of a theory counter to the accepted understanding of grating diffraction. We worked on a project that involved observing a forbidden diffraction order. Until this project we have focused on the primary reflection, the zeroth order diffraction, and the absorption of surface plasmons due to the first diffracted order moving across the boundary of the conductor. A grating can be described by it's grating wavevector $k_g = 2\pi/P$, where P is the grating period. The diffraction order m can take positive or negative integer values ($m = 0, \pm1, \pm2, \pm3...$) as the fundamental grating vector k_g is added to the in-plane momentum of the incident radiation. For a grating with a half wave symmetric profile, symmetry laws prohibit incident radiation from diffracting into even orders. According to the theoretical calculations, the resonant case of grating diffraction could produce an astonishingly large diffraction efficiency into these forbidden orders. Owing to the large propagation length of SPPs on metal gratings in the infrared, the 1st order guided mode was able to re-radiate into forbidden orders. The allowed transition of -3 from the +1st order would result in a diffraction into the -2nd order. The simulations pointed to an extraordinary 65% of the incident radiation being

channeled into this symmetry-forbidden order. We designed an experiment to observe this mode, and confirm that this theoretical efficiency was possible.

The angle at which higher order diffractions are scattered into θ_m is given by

$$P(\sin\theta_m - \sin\theta_i) = m\lambda \tag{5.1}$$

where λ and θ_i are the wavelength and incidence angle of the source radiation. For the m = 0 reflected beam, the wavelength dependence in Eq. 5.1 disappears. The angle of the reflected beam is equal to the incidence angle, only measured in opposite directions from the surface normal. Higher diffraction orders retain the wavelength dependence in the diffraction equation, so that for a specular measurement the detector angle must be adjusted as the wavelength of the source changes. The goniometer used previously to control the incidence angle would not be capable of performing this measurement. Instead a goniometer with two independent motors to control the sample stage and detector arm was used. It would not be sufficient to simply calculate the expected position of the diffracted order and take measurements. Imperfections in the setup or sample could lead to a slightly different measured angle of diffraction, and because the sensitivity of the detector is maximum in the center this difference could result an incorrectly measured intensity. To remedy this, we wrote a custom labview program for this experiment that swept the detector in an arc around the expected angle. The result was a Gaussian-beam profile, measured at each wavelength that we fit to extract the intensity maximum.

5.2 Methodology

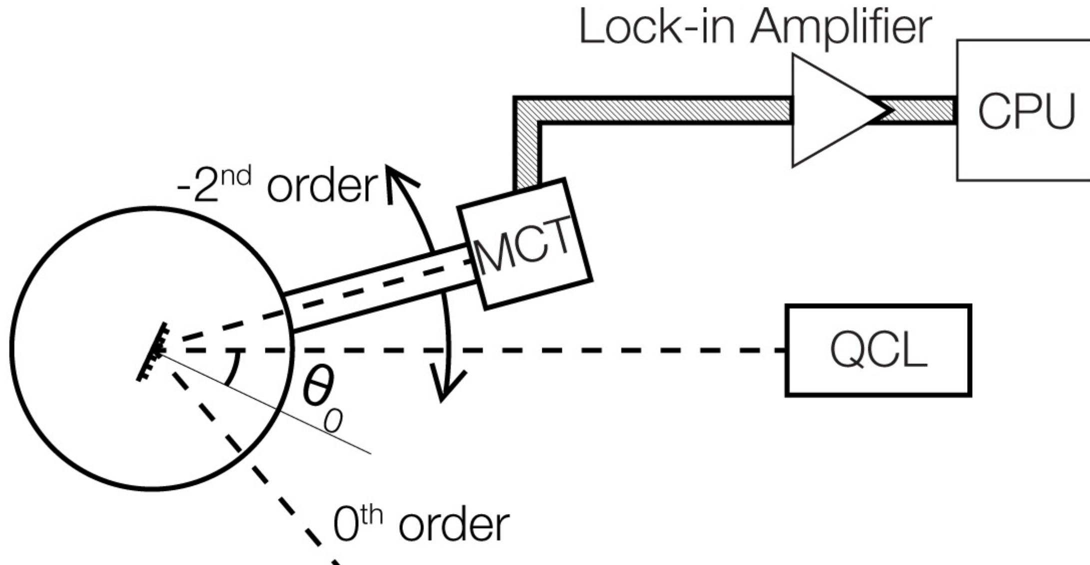

Figure 5.1: **Experimental Schematic.** A schematic showing the optical setup for the experiment. A two-axis motor-driven goniometer is used to position the sample and detector. The reflection from a pulsed QCL is measured by a MCT detector and demodulated by a lock-in amplifier.

We fabricated silver gratings using the methods discussed in the previous chapter. According to the simulated results, the highest diffraction efficiency for the wavelength range of the QCL was expected to occur for 15μm period gratings with 700nm groove depth. A 15μm period photomask with 50% duty cycle was used to obtain the necessary half wave symmetric rectangular profile. It was anticipated that the duty cycle of these gratings would have a large effect on the efficiency of this diffraction order. We made a concerted effort to produce gratings with as close to 50% duty cycle as possible, and we fabricated many gratings in a variety of ways in order to achieve this.

Metal gratings were produced by liftoff on bare wafers, followed by a capping layer of silver, using negative-tone resist, and two-layer resists. We also performed liftoff on wafers with a basal layer of silver already in place, using both methods of undercutting. We were able to produce gratings with duty cycle ranging from 45% to 50%.

We measured these gratings using the two-axis goniometer, with the TM-polarized incident radiation of the QCL pulsed at 100kHz. The source wavelength was incremented between 7.9μ and 10.5μm. The detector signal was demodulated by a lock-in amplifier at the chopping frequency of the QCL. A schematic of the measurement setup used is shown in Figure 5.1. A sighting HeNe was used for alignment. The samples were mounted so that they could be tilted such that the sample was normal to the radiation at 0° incidence angle. The stage also allowed for rotational positioning of the sample to ensure the TM component of the incident radiation was perpendicular to the grating. This rotation is important because the diffracted orders are affected by a vertical shift, and must be at the centerline of the detector. The angle rastering process was performed on both the ordinary (m=0) refection, as well as the -2nd order diffraction, followed by the same process on the ordinary reflection of a mirror. We wrote a custom Python code in order to fit the Gaussian profiles at each measured wavelength, and then extract the maximum intensity for each. We then performed a baseline measurement with the beam blanked, and a noise level for the detector was extracted. Then, to calculate the reflectance, we removed the noise level from every measurement, and divided each grating spectra by the reflectance spectrum of the mirror.

5.3 Results

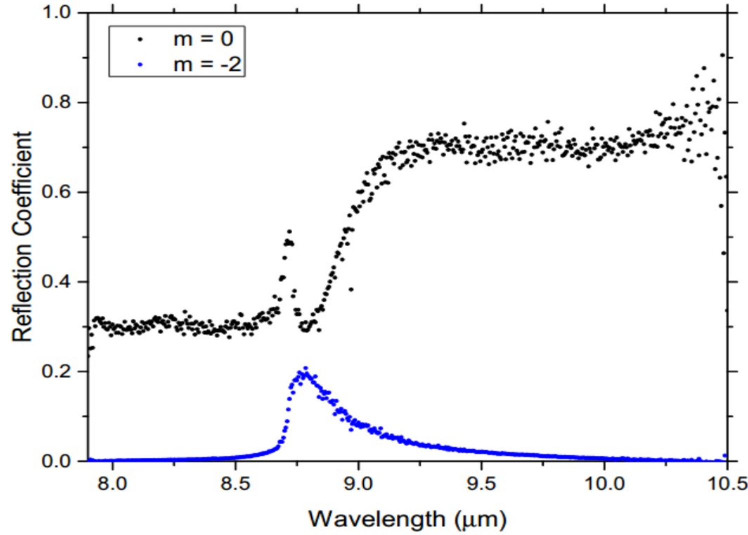

Figure 5.2: **Experimental Observation.** Initial observation of diffraction into the forbidden m = -2 order. Reflection coefficients for different diffraction orders measured for a 15μm-period Ag grating with 1.3μm deep rectangular grooves, and $\sim$ 50% duty cycle. The ordinary reflection is shown (black), alongside the m = -2 diffraction (blue).

Remarkably, we were able to observe the forbidden second order (Figure 5.2). Just as anticipated from theoretical models, the intensity was very near zero over the range of wavelengths away from the first order SPP excitation. But for the wavelength range over which the guided mode in the metal was observed, there was a nonzero diffraction efficiency into the -2nd order. Figure 5.2 shows the measured reflection coefficient for both the m = 0 (black) and m = -2 (blue) orders. As exciting as this observation was, there was a discrepancy between the predicted intensity of 65%

and the measured intensity of 20%. The grating used for this measurement had groove depths of $\sim$ 1.3μm, and did not exhibit high reflectivity for wavelengths lower than 8.7μm. Additionally, this grating did not produce a very narrow or deep SPP feature at $\sim$ 8.8μm. The weak SPP absorption exhibited by this grating resulted in a low diffraction efficiency into the m = -2 order.

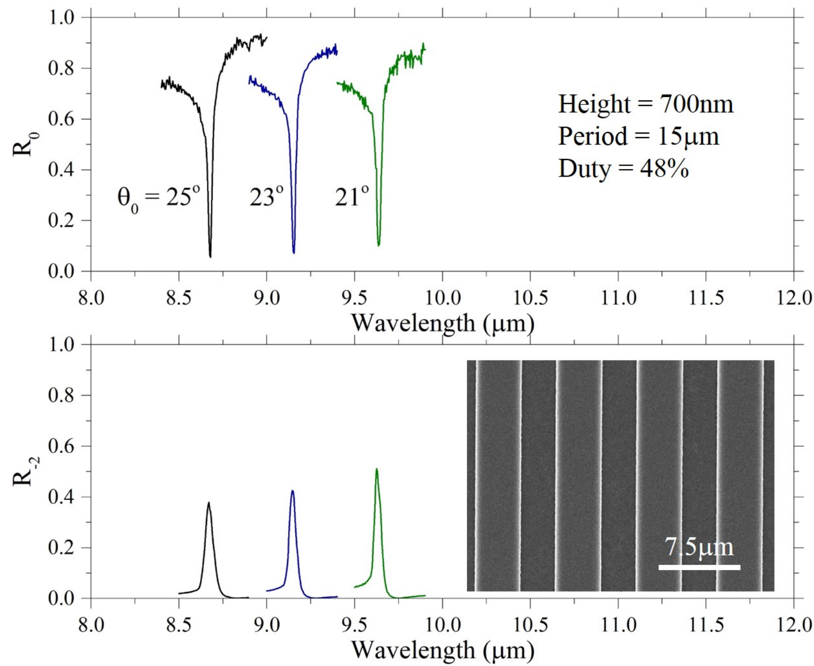

Figure 5.3: **Grating with Higher Diffraction Efficiency.** Measured reflection coefficients for a 15μm-period Ag grating with 700nm deep rectangular grooves, and 48% duty cycle. The reflection coefficients for the m = 0 and m = -2 are shown for three different incidence angles: 25° (black), 23° (blue), 21° (green). A top down SEM micrograph of the measured grating is shown in the lower inset.

The next measured sample showed a marked improvement, with over 50% of the incident radiation re-emitted into the forbidden mode. Figure 5.3 shows the reflected intensity of the m = 0 and

m = -2 diffraction orders for three different angles of incidence. An SEM image of the measured grating is shown in the inset of Figure 5.3. The grating grooves are 700nm deep with a 15μm period. The parameters of this grating agree with the simulated values that resulted in maximum diffraction efficiency, except the experimental duty cycle was approximately equal to 48%. This sample exhibited double to triple the diffraction efficiency into the symmetry prohibited order, as compared to the initial observation. This is likely due to the groove depth, and a more precise duty cycle. Although this sample has diffraction efficiency approaching 60%, the measurement does not yet confirm the 65% expected by the theory. The last parameter to optimize was the duty cycle, and many gratings were fabricated in an attempt to create grating with a duty cycle of exactly 50%. We were able to fabricate the desired grating using a bare wafer, an undercutting resist layer, and a capping layer of metal as our method of choice.

The reflection coefficients for the m = 0 and m = -2 for a Ag grating with groove depth 700nm, 15μm period, and duty cycle of 50% is shown in Figure 5.4. We used a scanning electron microscope to capture a high magnification image and determine the duty cycle (Figure 5.4 inset). The result was a grating that had a diffraction efficiency into the forbidden order of over 80%. As expected, an angle of incidence of 25° produced a diffraction into the forbidden order at just over 65% efficiency. More surprising still was that for shallower incidence angles the diffraction efficiency exceeded 80%.

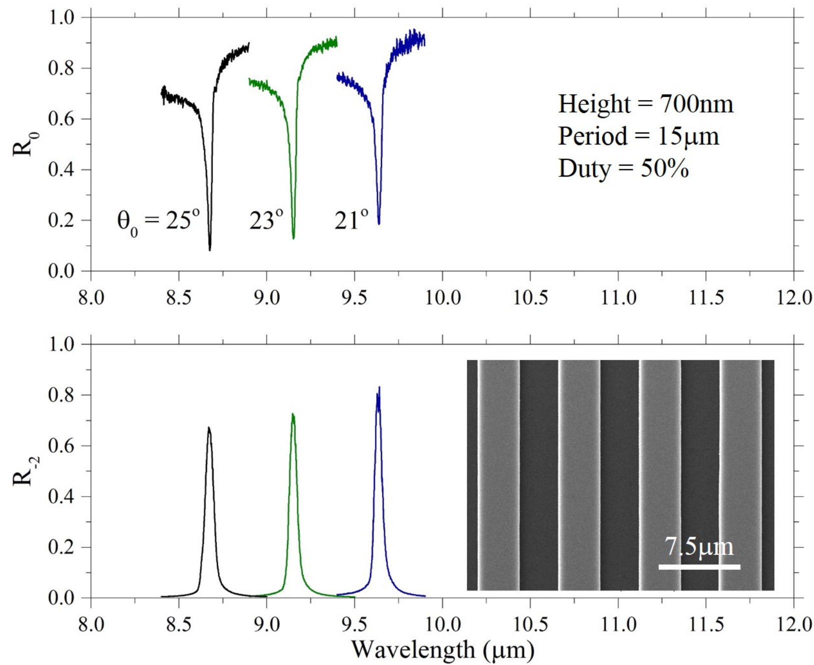

Figure 5.4: **Highest Diffraction Efficiency Measured.** Measured reflection coefficients for a 15μm-period Ag grating with 700nm deep rectangular grooves, and 50% duty cycle. The reflection coefficients for the m = 0 and m = -2 are shown for three different incidence angles: 25° (black), 23° (blue), 21° (green). A top down SEM micrograph of the measured grating is shown in the lower inset.

5.4 Discussion

This is the first experimental observation of this unique phenomenon. The conventional wisdom for SPPs to enhance absorption of electromagnetic radiation, rather than transmit, is reversed in this situation. Here we observe the extraordinary resonant enhancement of diffraction into symmetry prohibited orders by SPPs. This new observation helps to inform our understanding of matter-light

interactions. This result opens up new avenues for devices that exploit SPP resonances, shedding light on a new outlet for the electromagnetic energy accumulated in the SPP mode.

CHAPTER 6
CONCLUSIONS

In these studies we have facilitated the implementation of graphene into applied devices. We studied various methods of graphene exfoliation, CVD graphene transfer, and graphene post-processing. The more consistently with which this material can be produced, transferred, and cleaned, the faster the adoption of this material will become. The absence of a bandgap in graphene is one of the most prominent hurdles to overcome for digital applications. We have studied methods to produce graphene nanoconstrictions to address this issue. We performed a study on the role impurities play in these graphene nanoconstricions, concluding that these local charged impurities play an important role in determining the potential landscape of the nanoribbon. In turn, these potential fluctuations can be used to control the energy necessary for conduction through the ribbon. We also studied two possible candidates for other thin film devices, H-BN and BSCCO. We found that these materials are both difficult to isolate in two-dimensional form, and they may likely be insulating. Other than digital applications, we studied the possibility of a new type of optical device using graphene. We produced an optical sensor using graphene and a SPP coupler capable of wavelength selectivity and sensitivity in the visible range. In addition we studied a new phenomenon of SPPs in which they can resonantly facilitate diffraction into forbidden orders, previously thought impossible.

APPENDIX A
SCANNING ELECTRON MICROSCOPE STANDARD OPERATING PROCEDURE

A.1 Setup

1. Launch the Tescan Vega software and Login to the proper account.

2. Using the manual vertical control for the stage, lower the stage to the lowest position.

3. Open the nitrogen cylinder, and ensure that no greater than 10psi is used during venting.

4. Use the Vega software to vent the chamber of the SEM.

5. Tighten the sample mount to the stage and close the chamber door.

6. Close the nitrogen cylinder.

7. Use the Vega software to pump down the chamber of the SEM.

8. Acquire image using imaging guidelines.

9. Ensure that the vertical position of the stage is at its minimum and the stage tilt is set to zero degrees.

10. Open the nitrogen cylinder, and ensure that no greater than 10psi is used during venting.

11. Use the Vega software to vent the chamber of the SEM.

12. Remove your sample mount and close the chamber door.

13. Close the nitrogen cylinder.

14. Use the Vega software to pump down the chamber of the SEM.

15. Use the Vega software to turn off the microscope system, logging you out of your account in the process.

A.2 Imaging

1. Turn the accelerating voltage on using the HV button.

2. If the Filament does not auto heat then turn the heating on as well.

3. With the stage tilt at zero degrees find an unobstructed spot on the stage and change your working distance so that the stage comes into focus.

4. With the stage in focus, filling the scan, and at low magnification, press the Auto button in the top right of the emission and accelerating voltage control.

5. Let the microscope use an automated procedure to change the emission current, gun shift, and gun tilt to optimal values.

6. Depending on the required imaging, the user now can either continue to optimize the beam for high magnification imaging, or for low magnification imaging can skip the following procedures.

7. Next move to the gold standard, manually set the working distance to 8mm and physically raise the stage until the image of the gold standard comes into focus.

8. Find an area which contains a spot of high contrast to the surrounding surface, and focus on this spot (usually a spot of dust or other large impurity).

9. Create a smaller raster window over the spot in question and use the manual adjustment to have the software sweep the working distance back and forth.

10. The image will "wobble" and the trackball is used to counteract this by rolling the trackball in the direction of the image movement (choosing the proper direction to roll the trackball dampens these oscillations while the reverse happens for an incorrect choice).

11. When you have dampened the wobbling as much as possible, find a smaller spot similar to the first, increase the magnification and change your probe current to 12 and repeat the procedure to dampen the oscillations of the image.

12. Proceed to zoom in further until small islands of gold are visible on the surface of the gold standard.

13. Finely tune the working distance so that the surface is in good focus and click the degauss button, then repeat until further degaussing has no perceivable effect on focus.

14. At a probe current of 16 scan window of around 4-6μm find a gold island with high contrast and create a small raster scan on this spot.

15. By using the keyboard buttons to lock the X and Y axis of the trackball independently change the stigmation for X and then Y until the scan is in the most focus possible. Note: without any astigmatism, as working distance is changed slightly a circular island will defocus radially, but with astigmatism the island will defocus in either the vertical or horizontal direction.

16. At this magnification alternate the wobble correction and astigmatism correction procedures until no further change is necessary.

17. Move the stage so that the scan is over the sample to be imaged.

18. Attain desired magnification and resolution then use the image saving capabilities to acquire an image.

19. After imaging lower the stage manually and follow the standard operating procedures to remove the sample and turn off the SEM.

Tips:

1) Always use a sample which is conducting, an insulating sample should be sputtered with a thin conducting film before imaging.

2) Select the correct accelerating voltage for your sample, the accelerating voltage dictates the penetration depth of the imaging electrons. Lowering the accelerating voltage lowers the resolution but allows imaging of thin materials which are not visible at higher voltages.

3) Wide field mode can be used to image a larger viewfield if need be, but always switch back to resolution mode for imaging.

4) Increasing the probe current, increases the resolution by lowering the beam spot size, but lowers the signal to the detector. Using a slow scan rate will increase the signal-to-noise of the image.

5) When very fine features require imaging, tilting the stage is a great tool, as proper tilting angles the deflected electrons into the detector (column on left of chamber). Using a small working distance of 6mm, and probe current of 16-18 at 30KV will also allow for better results at high magnification

6) When planning on using either tilt or working distances under 8mm, use the extender stub, which raises the sample above the gold standard, and plan on the sample placement and stage rotation before closing the chamber.

7) Use extreme caution when either tilting or working at sub 8mm working distance: 1) Never rotate the stage when the stage is under 8mm in distance or tilted off of zero degrees; and 2) always tilt at a working distance greater than 20mm and then manually raise the sample into closer

focus. When tilting, the sample should be positioned to that it is closest to the column after tilting.

APPENDIX B
WIREBONDER STANDARD OPERATING PROCEDURE

B.1 Setup

1. Before wirebonding it is recommended to let the machine warm up for 30 minutes.

2. Tighten the chip socket to the workholder and insert the sample.

3. Ensure that the sample is securely held, as any motion of the sample during bonding will prevent proper bonds from forming.

4. Lower the workholder by rotating it clockwise to ensure that the sample does not run into the wedge, as various workholder heights will be used.

5. To ensure proper bonding, the relative height between your lowest bond and the tip of the wedge must be set precisely in the following way:

(A) Make sure that the motor switch is in the up position (not off).

(B) Ensure the machine is in its reset position by pushing the setup/reset switch to the reset position, the LED by 1st should be illuminated.

(C) Move the workholder from the workbench so that the path of the wedge is clear and press the button under your finger on the chessman, this places the machine in semi-automatic mode.

(D) You should see the bonding head move and the LED by 2nd illuminate.

(E) The bonding head height can now be adjusted by rotating the Loop dial, rotate the dial clockwise until the loop is set to 10.

(F) Place the workholder on the workbench and position the sampleunder the wedge, lower the wedge slowly by lowering the loop setting.

(G) The wedge should come into contact with the shallowest bonding surface at Loop = 1 with a tolerance of .5 in each direction.

(H) If the wedge does not touch the surface even at Loop 0 then the workholder should be raised, by rotating it counter-clockwise.

(I) The workholder should not be adjusted while under the wedge, andthe wedge should be raised to Loop 10 each time before lowering.

(J) Once the wedge is making contact with the lowest bonding surface at Loop 1 then set the loop to 4-6, remove the workholder, and press the chessman button or reset switch to bring the cycle back to reset position.

(K) When changing spools of wire, ensure that the wire unravels from thebottom of the spool, and that it is threaded through the closer hole on the transducer, which is the setup for our 30° wedge hole.

6. To thread the wire into the wedge raise the clamp with the leftmost lever on the left of the chassis next to the tail control.

7. Then, using a newly clipped strait segment of wire, angle the wire with tweezers to about 30° and try to pass the wire through the hole on the the back of the wedge.

8. Note that the user should wear gloves for this step, as touching the wire, spool, or wedge with bare hands will affect bonding quality.

B.2 Bonding

1. With the machine setup properly, the bonding parameters must now be adjusted to suit the sample to be bonded.

2. Bonding parameters can be fine tuned by the user in the following way:

(A) **Force**: Additional force applied on top of the static force. Note: too little force and the wire will lift from the bond without adhering. The resulting wire will not be flattened. Too much force and the wire will be clipped upon bonding. You will see a flattened wire that is left on the surface, and the wire will break past the bond.

(B) **Time**: Amount of time to apply ultrasonic oscillations. Note: too little time and the ultrasonics are not applied long enough to soften the wire for bonding. Too much time and the initial bond that is formed will be weakened.

(C) **Power**: Ultrasonic vibration amplitude. Note: too little power and the ultrasonics will not be able to soften the wire. Too much power and the ultrasonics will break the wire below the bond and tear it free from the surface.

3. The upper dials control the 1st bond parameters, while the lower dials control the 2nd bond parameters, and should be adjusted depending on the direction of bonding.

4. While optimizing these settings the user should try to use the lowest parameters possible while still achieving bonds that take some force to remove with tweezers (pull testing).

5. Bonding should be performed along a straight line, so before bonding make sure the first and

second bond are along a line parallel with the bonding arm, by rotating the workholder.

6. Bonding can be performed in either Semi-Automatic or Manual modes

(A) **Semi-Auto Mode:** The finger button on the chessman is pushed and held to lower the wedge to the first search position, which can be changed by adjusting the upper search dial. In the first search position, manipulate the sample with the chessman until the wedge is directly over the first bonding surface and release the chessman button. The first bond will be performed and the wedge will be lifted to the loop position to create the wire loop. The second bond is performed in the same way and the search is adjusted using the lower search dial.

(B) **Manual Mode:** The manual Z-lever is located on the right of the front panel dials, and can be used to directly control the height of the wedge. In this mode lower the wedge slowly and manipulate the sample with the chessman until the bonding surface is under the wedge, then fully depress the lever to initiate the bond. Raise the lever slowly as the loop is controlled entirely by the user by manipulating the wedge height. The second bond is performed in the same way. The clamp position is setup based on the recommended settings for proper tear and tail motions. DO NOT MOVE THE CLAMP! If you are unable to make a bond due to improper clearance of the clamp, then you must reposition the sample and try a different bonding direction.

7. When finished lower the workholder and turn off the machine.

APPENDIX C
GONIOMETER STANDARD OPERATING PROCEDURE

C.1 General Goniometer Control

Only click the zero button if you need to re-calibrate (if someone else zeroed incorrectly or a collision causes a stepper motor to slip). This program can be used to set the speed of the two axis by entering the desired values and clicking the config button (the fastest speed is the default values when the program is loaded). You can step either axis in both directions in large medium small and fine increments (1, 0.1, 0.01 and 0.001 degree respectively). Specific angles can be achieved by using the buttons on the far right. The toggle between relative angle and absolute angle accounts for the current sample mounting of the goniometer. The absolute angle corresponds to the physical dial, while the relative angle is related to the incident beam.

C.2 Measurement

The two primary forms of measurement are controlled using the Angle Sweep and Wavelength Sweep programs. Both programs are intended to follow the primary reflection, and operate in Relative incidence angle, where the detector angle is twice as large

The Angle Sweep program has an outer loop to control the wavelength, and an inner loop to control the incidence/detector angle. This means that the angle is swept quickly between the specified bounds, and the wavelength is stepped at the end of each angular sweep in “automated” mode. For this program the fast axis is angle.

Similarly the Wavelength Sweep program has an outer loop to control the angle, and an inner loop to control the wavelength. For this program the fast axis is wavelength.

In each of these programs there is a control near the top for the fast axis bounds, and the wavelength step or angle sweep speed. Using an angle sweep speed of .125deg/sec the continuous sampling of the lock-in yields approx 0.003deg resolution. The slow axis bounds have a minimum that is always executed, regardless of the automated setting. If the program is not in automated mode then the program will execute just the minimum slow axis bound and then show a dialog to save your file. If running the program in automated mode then the path must be set to the directory where you want to save your files and the file name will be the base name with the slow axis appended. (Note: when you choose your path the interface expects you to select a file, so if you create a new folder for your data the easiest thing to do is to make a new text file in that folder and choose this file in the path dialog window in LabView. Be sure to delete this file name from the path, i.e. the path must end in a "\".

Run the program, click the start button, and the data should update in real time. Stick around long enough to see the data show up. If automated is selected when you click quit the program will increment the slow axis. Ensure the slow axis is at the desired number when clicking start.

Approximate Runtimes: 1) 5-degree scan for $\sim$10 minutes at 0.125deg/sec, and 2) 7.9μm-10.5μm scan for $\sim$10 minutes at a 5nm increment.

LIST OF REFERENCES

[1] D. R. Cooper, B. D'Anjou, N. Ghattamaneni, B. Harack, M. Hilke, A. Horth, N. Majlis, M. Massicotte, L. Vandsburger, E. Whiteway, and V. Yu, "Experimental review of graphene," *ArXiv e-prints*, Oct. 2011.

[2] A. Kumar and C. H. Lee, "Synthesis and biomedical applications of graphene: Present and future trends," 2013.

[3] K. Novoselov, A. K. Geim, S. Morozov, D. Jiang, M. K. I. Grigorieva, S. Dubonos, and A. Firsov, "Two-dimensional gas of massless dirac fermions in graphene," *nature*, vol. 438, no. 7065, pp. 197–200, 2005.

[4] D. Zhang, L. Men, and Q. Chen, "Microfabrication and applications of opto-microfluidic sensors," *Sensors*, vol. 11, no. 5, pp. 5360–5382, 2011.

[5] P. Mulpur, S. Patnaik, A. Chunduri, T. M. Rattan, A. M. Rao, and V. Kamisetti, "Detection of cd 2+ ions using surface plasmon coupled emission on engineered silver-α nano alumina thin film hybrids," *Soft Nanoscience Letters*, vol. 2013, 2013.

[6] P. R. Wallace, "The band theory of graphite," *Phys. Rev.*, vol. 71, pp. 622–634, May 1947. [Online]. Available: http://link.aps.org/doi/10.1103/PhysRev.71.622

[7] G. Mahan, *Condensed Matter in a Nutshell*, ser. In a Nutshell. Princeton Univers. Press, 2011. [Online]. Available: http://books.google.com/books?id=v3FVOH2XK4gC

[8] S. Das Sarma, S. Adam, E. H. Hwang, and E. Rossi, "Electronic transport in two-dimensional graphene," *Rev. Mod. Phys.*, vol. 83, pp. 407–470, May 2011. [Online]. Available: http://link.aps.org/doi/10.1103/RevModPhys.83.407

[9] R. Saito, G. Dresselhaus, and M. S. Dresselhaus, "Trigonal warping effect of carbon nanotubes," *Phys. Rev. B*, vol. 61, pp. 2981–2990, Jan 2000. [Online]. Available: http://link.aps.org/doi/10.1103/PhysRevB.61.2981

[10] K. S. Novoselov, A. K. Geim, S. Morozov, D. Jiang, Y. Zhang, S. Dubonos, I. Grigorieva, and A. Firsov, "Electric field effect in atomically thin carbon films," *science*, vol. 306, no. 5696, pp. 666–669, 2004.

[11] K. Novoselov, D. Jiang, F. Schedin, T. Booth, V. Khotkevich, S. Morozov, and A. Geim, "Two-dimensional atomic crystals," *Proceedings of the National Academy of Sciences of the United States of America*, vol. 102, no. 30, pp. 10 451–10 453, 2005.

[12] X. Du, I. Skachko, A. Barker, and E. Andrei, "Approaching ballistic transport in suspended graphene," *Nature Nanotechnology*, vol. 3, no. 8, pp. 491–495, 2008.

[13] K. Novoselov, A. Geim, S. Morozov, D. Jiang, M. Grigorieva, S. Dubonos, and A. Firsov, "Two-dimensional gas of massless dirac fermions in graphene," *Nature*, vol. 438, no. 7065, pp. 197–200, 2005.

[14] Y.-W. Tan, Y. Zhang, K. Bolotin, Y. Zhao, S. Adam, E. H. Hwang, S. Das Sarma, H. L. Stormer, and P. Kim, "Measurement of scattering rate and minimum conductivity in graphene," *Phys. Rev. Lett.*, vol. 99, p. 246803, Dec 2007. [Online]. Available: http://link.aps.org/doi/10.1103/PhysRevLett.99.246803

[15] K. Bolotin, K. Sikes, Z. Jiang, M. Klima, G. Fudenberg, J. Hone, P. Kim, and H. Stormer, "Ultrahigh electron mobility in suspended graphene," *Solid State Communications*, vol. 146, no. 910, pp. 351 – 355, 2008. [Online]. Available: http://www.sciencedirect.com/science/article/pii/S0038109808001178

[16] P. Blake, E. Hill, A. C. Neto, K. Novoselov, D. Jiang, R. Yang, T. Booth, and A. Geim, "Making graphene visible," *Applied Physics Letters*, vol. 91, no. 6, p. 063124, 2007.

[17] X. Li, W. Cai, J. An, S. Kim, J. Nah, D. Yang, R. Piner, A. Velamakanni, I. Jung, E. Tutuc *et al.*, "Large-area synthesis of high-quality and uniform graphene films on copper foils," *Science*, vol. 324, no. 5932, pp. 1312–1314, 2009.

[18] X. Li, C. W. Magnuson, A. Venugopal, J. An, J. W. Suk, B. Han, M. Borysiak, W. Cai, A. Velamakanni, Y. Zhu *et al.*, "Graphene films with large domain size by a two-step chemical vapor deposition process," *Nano letters*, vol. 10, no. 11, pp. 4328–4334, 2010.

[19] X. Li, C. W. Magnuson, A. Venugopal, R. M. Tromp, J. B. Hannon, E. M. Vogel, L. Colombo, and R. S. Ruoff, "Large-area graphene single crystals grown by low-pressure chemical vapor deposition of methane on copper," *Journal of the American Chemical Society*, vol. 133, no. 9, pp. 2816–2819, 2011.

[20] K. S. Kim, Y. Zhao, H. Jang, S. Y. Lee, J. M. Kim, K. S. Kim, J.-H. Ahn, P. Kim, J.-Y. Choi, and B. H. Hong, "Large-scale pattern growth of graphene films for stretchable transparent electrodes," *Nature*, vol. 457, no. 7230, pp. 706–710, 2009.

[21] A. Reina, X. Jia, J. Ho, D. Nezich, H. Son, V. Bulovic, M. S. Dresselhaus, and J. Kong, "Large area, few-layer graphene films on arbitrary substrates by chemical vapor deposition," *Nano letters*, vol. 9, no. 1, pp. 30–35, 2008.

[22] X. Li, Y. Zhu, W. Cai, M. Borysiak, B. Han, D. Chen, R. D. Piner, L. Colombo, and R. S. Ruoff, "Transfer of large-area graphene films for high-performance transparent conductive electrodes," *Nano letters*, vol. 9, no. 12, pp. 4359–4363, 2009.

[23] X. Liang, B. A. Sperling, I. Calizo, G. Cheng, C. A. Hacker, Q. Zhang, Y. Obeng, K. Yan, H. Peng, Q. Li *et al.*, "Toward clean and crackless transfer of graphene," *ACS nano*, vol. 5, no. 11, pp. 9144–9153, 2011.

[24] J. W. Suk, A. Kitt, C. W. Magnuson, Y. Hao, S. Ahmed, J. An, A. K. Swan, B. B. Goldberg, and R. S. Ruoff, "Transfer of cvd-grown monolayer graphene onto arbitrary substrates," *ACS nano*, vol. 5, no. 9, pp. 6916–6924, 2011.

[25] S. Bae, H. Kim, Y. Lee, X. Xu, J.-S. Park, Y. Zheng, J. Balakrishnan, T. Lei, H. R. Kim, Y. I. Song *et al.*, "Roll-to-roll production of 30-inch graphene films for transparent electrodes," *Nature nanotechnology*, vol. 5, no. 8, pp. 574–578, 2010.

[26] C. J. L. de la Rosa, J. Sun, N. Lindvall, M. T. Cole, Y. Nam, M. Löffler, E. Olsson, K. B. Teo, and A. Yurgens, "Frame assisted h2o electrolysis induced h2 bubbling transfer of large area graphene grown by chemical vapor deposition on cu," *Applied Physics Letters*, vol. 102, no. 2, p. 022101, 2013.

[27] A. C. Ferrari, J. C. Meyer, V. Scardaci, C. Casiraghi, M. Lazzeri, F. Mauri, S. Piscanec, D. Jiang, K. S. Novoselov, S. Roth, and A. K. Geim, "Raman spectrum of graphene and graphene layers," *Physical Review Letters*, vol. 97, no. 18, p. 187401, 2006, copyright (C) 2010 The American Physical Society Please report any problems to prola@aps.org PRL.

[28] A. Das, S. Pisana, B. Chakraborty, S. Piscanec, S. Saha, U. Waghmare, K. Novoselov, H. Krishnamurthy, A. Geim, A. Ferrari *et al.*, "Monitoring dopants by raman scattering in an electrochemically top-gated graphene transistor," *Nature nanotechnology*, vol. 3, no. 4, pp. 210–215, 2008.

[29] L. Cancado, K. Takai, T. Enoki, M. Endo, Y. Kim, H. Mizusaki, A. Jorio, L. Coelho, R. Magalhaes-Paniago, and M. Pimenta, "General equation for the determination of the crystallite size l a of nanographite by raman spectroscopy," *Applied Physics Letters*, vol. 88, no. 16, pp. 163 106–163 106, 2006.

[30] F. F. Fang and A. B. Fowler, "Transport properties of electrons in inverted silicon surfaces," *Phys. Rev.*, vol. 169, pp. 619–631, May 1968. [Online]. Available: http://link.aps.org/doi/10.1103/PhysRev.169.619

[31] M. C. J. M. Vissenberg and M. Matters, "Theory of the field-effect mobility in amorphous organic transistors," *Phys. Rev. B*, vol. 57, pp. 12 964–12 967, May 1998. [Online]. Available: http://link.aps.org/doi/10.1103/PhysRevB.57.12964

[32] C. Dean, A. Young, I. Meric, C. Lee, L. Wang, S. Sorgenfrei, K. Watanabe, T. Taniguchi, P. Kim, K. Shepard *et al.*, "Boron nitride substrates for high-quality graphene electronics," *Nature nanotechnology*, vol. 5, no. 10, pp. 722–726, 2010.

[33] J. Chen, C. Jang, S. Adam, M. Fuhrer, E. Williams, and M. Ishigami, "Charged-impurity scattering in graphene," *Nature Physics*, vol. 4, no. 5, pp. 377–381, 2008.

[34] J. Katoch, J.-H. Chen, R. Tsuchikawa, C. W. Smith, E. R. Mucciolo, and M. Ishigami, "Uncovering the dominant scatterer in graphene sheets on sio_2," *Phys. Rev. B*, vol. 82, p. 081417, Aug 2010. [Online]. Available: http://link.aps.org/doi/10.1103/PhysRevB.82.081417

[35] C. Smith and M. Ishigami, "Impact of coulomb impurities on transport properties of graphene nanoribbons," in *APS Meeting Abstracts*, Mar. 2010, p. 21001.

[36] M. Ishigami, J. H. Chen, W. G. Cullen, M. S. Fuhrer, and E. D. Williams, "Atomic structure of graphene on sio2," *Nano Letters*, vol. 7, no. 6, pp. 1643–1648, 2007, doi: 10.1021/nl070613a.

[37] J. Moser, A. Barreiro, and A. Bachtold, "Current-induced cleaning of graphene," *Applied Physics Letters*, vol. 91, no. 16, p. 163513, 2007.

[38] Z. Cheng, Q. Zhou, C. Wang, Q. Li, C. Wang, and Y. Fang, "Toward intrinsic graphene surfaces: a systematic study on thermal annealing and wet-chemical treatment of sio2-supported graphene devices," *Nano letters*, vol. 11, no. 2, pp. 767–771, 2011.

[39] Y. Dan, Y. Lu, N. J. Kybert, Z. Luo, and A. C. Johnson, "Intrinsic response of graphene vapor sensors," *Nano Letters*, vol. 9, no. 4, pp. 1472–1475, 2009.

[40] W. Xueshen, L. Jinjin, Z. Qing, Z. Yuan, and Z. Mengke, "Thermal annealing of exfoliated graphene," *Journal of Nanomaterials*, vol. 2013, p. 11, 2013.

[41] W. Bao, G. Liu, Z. Zhao, H. Zhang, D. Yan, A. Deshpande, B. LeRoy, and C. N. Lau, "Lithography-free fabrication of high quality substrate-supported and freestanding graphene devices," *Nano Research*, vol. 3, no. 2, pp. 98–102, 2010.

[42] I. Childres, L. A. Jauregui, M. Foxe, J. Tian, R. Jalilian, I. Jovanovic, and Y. P. Chen, "Effect of electron-beam irradiation on graphene field effect devices," *Applied Physics Letters*, vol. 97, no. 17, p. 173109, 2010.

[43] A. Carlson, A. M. Bowen, Y. Huang, R. G. Nuzzo, and J. A. Rogers, "Transfer printing techniques for materials assembly and micro/nanodevice fabrication," *Advanced Materials*, vol. 24, no. 39, pp. 5284–5318, 2012.

[44] S. Jeong, M.-W. Jung, J.-Y. Lee, H. Kim, J. Lim, K.-S. An, Y. Choi, and S. S. Lee, "Graphene electrodes transfer-printed with a surface energy-mediated wet pdms stamp: impact of au doped-graphene for high performance soluble oxide thin-film transistors," *J. Mater. Chem. C*, vol. 1, no. 36, pp. 5632–5637, 2013.

[45] K. Nakada, M. Fujita, G. Dresselhaus, and M. S. Dresselhaus, "Edge state in graphene ribbons: Nanometer size effect and edge shape dependence," *Physical Review B*, vol. 54, no. 24, p. 17954, 1996.

[46] Y.-W. Son, M. L. Cohen, and S. G. Louie, "Half-metallic graphene nanoribbons," *Nature*, vol. 444, no. 7117, pp. 347–349, 2006.

[47] M. Y. Han, B. Özyilmaz, Y. Zhang, and P. Kim, "Energy band-gap engineering of graphene nanoribbons," *Physical review letters*, vol. 98, no. 20, p. 206805, 2007.

[48] Z. Chen, Y.-M. Lin, M. J. Rooks, and P. Avouris, "Graphene nano-ribbon electronics," *Physica E: Low-dimensional Systems and Nanostructures*, vol. 40, no. 2, pp. 228–232, 2007.

[49] K. Todd, H.-T. Chou, S. Amasha, and D. Goldhaber-Gordon, "Quantum dot behavior in graphene nanoconstrictions," *Nano letters*, vol. 9, no. 1, pp. 416–421, 2008.

[50] S. Adam, E. Hwang, V. Galitski, and S. D. Sarma, "A self-consistent theory for graphene transport," *Proceedings of the National Academy of Sciences*, vol. 104, no. 47, pp. 18 392–18 397, 2007.

[51] F. Molitor, A. Jacobsen, C. Stampfer, J. Güttinger, T. Ihn, and K. Ensslin, "Transport gap in side-gated graphene constrictions," *Physical Review B*, vol. 79, no. 7, p. 075426, 2009.

[52] P. Gallagher, K. Todd, and D. Goldhaber-Gordon, "Disorder-induced gap behavior in graphene nanoribbons," *Physical Review B*, vol. 81, no. 11, p. 115409, 2010.

[53] C. Stampfer, S. Fringes, J. Güttinger, F. Molitor, C. Volk, B. Terrés, J. Dauber, S. Engels, S. Schnez, A. Jacobsen *et al.*, "Transport in graphene nanostructures," *Frontiers of Physics*, vol. 6, no. 3, pp. 271–293, 2011.

[54] Y.-M. Lin, V. Perebeinos, Z. Chen, and P. Avouris, "Electrical observation of subband formation in graphene nanoribbons," *Physical Review B*, vol. 78, no. 16, p. 161409, 2008.

[55] M. Caragiu and S. Finberg, "Alkali metal adsorption on graphite: a review," *Journal of Physics: Condensed Matter*, vol. 17, no. 35, p. R995, 2005.

[56] W. W. Hu, K. Sarveswaran, M. Lieberman, and G. H. Bernstein, "Sub-10 nm electron beam lithography using cold development of poly (methylmethacrylate)," *Journal of Vacuum Science & Technology B*, vol. 22, no. 4, pp. 1711–1716, 2004.

[57] N. Kharche and S. K. Nayak, "Quasiparticle band gap engineering of graphene and graphone on hexagonal boron nitride substrate," *Nano letters*, vol. 11, no. 12, pp. 5274–5278, 2011.

[58] D. Pacile, J. Meyer, C. O. Girit, and A. Zettl, "The two-dimensional phase of boron nitride: Few-atomic-layer sheets and suspended membranes," *Applied Physics Letters*, vol. 92, no. 13, pp. 133 107–133 107, 2008.

[59] R. S. Pease, "An x-ray study of boron nitride," *Acta Crystallographica*, vol. 5, no. 3, pp. 356–361, 1952.

[60] S. Sunshine, T. Siegrist, L. Schneemeyer, D. Murphy, R. Cava, B. Batlogg, R. Van Dover, R. Fleming, S. Glarum, S. Nakahara *et al.*, "Structure and physical properties of single crystals of the 84-k superconductor bi 2.2 sr 2 ca 0.8 cu 2 o 8+ δ," *Physical Review B*, vol. 38, no. 1, p. 893, 1988.

[61] M. Subramanian, C. Torardi, J. Calabrese, J. Gopalakrishnan, K. Morrissey, T. Askew, R. Flippen, U. Chowdhry, and A. Sleight, "A new high-temperature superconductor: Bi2sr3-x cax cu2o8+ y," *Science*, vol. 239, no. 4843, pp. 1015–1017, 1988.

[62] Z. Zhang and C. M. Lieber, "Measurement of the energy gap in oxygen-annealed bi 2 sr 2 cacu 2 o 8+ δ high-t c superconductors by tunneling spectroscopy," *Physical Review B*, vol. 47, no. 6, p. 3423, 1993.

[63] C. Kittel, *Introduction to Solid State Physics*. John Wiley & Sons, 2004. [Online]. Available: http://books.google.com/books?id=kym4QgAACAAJ

[64] S. Maier, *Plasmonics: Fundamentals and Applications*. Springer Science+Business Media, LLC, 2007. [Online]. Available: http://books.google.com/books?id=yT2ux7TmDc8C

[65] S. J. Allen, D. C. Tsui, and R. A. Logan, "Observation of the two-dimensional plasmon in silicon inversion layers," *Phys. Rev. Lett.*, vol. 38, pp. 980–983, Apr 1977. [Online]. Available: http://link.aps.org/doi/10.1103/PhysRevLett.38.980

[66] M. Jablan, H. Buljan, and M. Soljačić, "Plasmonics in graphene at infrared frequencies," *Phys. Rev. B*, vol. 80, p. 245435, Dec 2009. [Online]. Available: http://link.aps.org/doi/10.1103/PhysRevB.80.245435

[67] P. B. Johnson and R. W. Christy, "Optical constants of the noble metals," *Phys. Rev. B*, vol. 6, pp. 4370–4379, Dec 1972. [Online]. Available: http://link.aps.org/doi/10.1103/PhysRevB.6.4370

[68] J. P. Marton and B. D. Jordan, "Optical properties of aggregated metal systems: Interband transitions," *Phys. Rev. B*, vol. 15, pp. 1719–1727, Feb 1977. [Online]. Available: http://link.aps.org/doi/10.1103/PhysRevB.15.1719

[69] A. Otto, "Excitation of nonradiative surface plasma waves in silver by the method of frustrated total reflection," *Zeitschrift für Physik*, vol. 216, no. 4, pp. 398–410, 1968.

[70] E. Kretschmann and H. Raether, "Radiative decay of non radiative surface plasmons excited by light(surface plasma waves excitation by light and decay into photons applied to nonradiative modes)," *Zeitschrift Fuer Naturforschung, Teil A*, vol. 23, p. 2135, 1968.

[71] E. Kretschmann, "Die bestimmung optischer konstanten von metallen durch anregung von oberflächenplasmaschwingungen," *Zeitschrift für Physik*, vol. 241, no. 4, pp. 313–324, 1971.

[72] F. Yang, G. Bradberry, and J. Sambles, "The study of the optical properties of obliquely evaporated nickel films using ir surface plasmons," *Thin Solid Films*, vol. 196, no. 1, pp. 35–46, 1991.

[73] R. J. Bussjager and H. A. Macleod, "Using surface plasmon resonances to test the durability of silver-copper films," *Applied optics*, vol. 35, no. 25, pp. 5044–5047, 1996.

[74] S. Franzen, "Surface plasmon polaritons and screened plasma absorption in indium tin oxide compared to silver and gold," *The Journal of Physical Chemistry C*, vol. 112, no. 15, pp. 6027–6032, 2008.

[75] E. H. Nicollian, J. R. Brews, and E. H. Nicollian, *MOS (metal oxide semiconductor) physics and technology*. Wiley New York et al., 1982, vol. 1987.

[76] H. R. Gwon and S. H. Lee, "Spectral and angular responses of surface plasmon resonance based on the kretschmann prism configuration," *Materials transactions*, vol. 51, no. 6, pp. 1150–1155, 2010.

[77] A. Pirkle, J. Chan, A. Venugopal, D. Hinojos, C. Magnuson, S. McDonnell, L. Colombo, E. Vogel, R. Ruoff, and R. Wallace, "The effect of chemical residues on the physical and electrical properties of chemical vapor deposited graphene transferred to sio2," *Applied Physics Letters*, vol. 99, no. 12, p. 122108, 2011.

[78] M. Shahzad, G. Medhi, R. E. Peale, W. R. Buchwald, J. W. Cleary, R. Soref, G. D. Boreman, and O. Edwards, "Infrared surface plasmons on heavily doped silicon," *Journal of Applied Physics*, vol. 110, no. 12, p. 123105, 2011.

[79] J. W. Cleary, G. Medhi, R. E. Peale, and W. R. Buchwald, "Long-wave infrared surface plasmon grating coupler," *Applied optics*, vol. 49, no. 16, pp. 3102–3110, 2010.

[80] R. Grantab, V. B. Shenoy, and R. S. Ruoff, "Anomalous strength characteristics of tilt grain boundaries in graphene," *Science*, vol. 330, no. 6006, pp. 946–948, 2010.